POLITECHNIKA KRAKOWSKA im. T. Kościuszki
Wydział Mechaniczny
Instytut Mechaniki Stosowanej

**Instytut
M-1**

Kierunek studiów: Mechanika i Budowa Maszyn
Specjalność   : Mechanika Komputerowa

STUDIA STACJONARNE

PRACA DYPLOMOWA
MAGISTERSKA

Mariusz Juchno

ELECTROMAGNETIC FEM ANALYSIS OF THE CERN
PROTON SYNCHROTRON MAIN MAGNETIC UNIT

Promotor:
prof. dr hab. inż. **Błażej Skoczeń**

Opiekun CERN:
dr **Simone Gilardoni**

Kraków, rok akad. 2007/2008

KARTA PRACY DYPLOMOWEJ

POLITECHNIKA KRAKOWSKA **WYDZIAŁ MECHANICZNY** **INSTYTUT MECHANIKI STOSOWANEJ**	**Nr pracy:**
Katedra Mechaniki Technicznej	**Autor pracy:** **Mariusz Juchno**
Promotor **prof. dr hab. inż. Błażej Skoczeń**	

Temat:

Electromagnetic FEM analysis of the CERN Proton Synchrotron main magnetic unit

………………….. …………………………………
Podpis promotora   Kierownika specjalności

Uzgodniona ocena pracy: ………………………………………………………………..

……………………… ....
Podpis promotora   Podpis recenzenta   Dyrektora Instytutu
                                                                                        ds. Dydaktyki

Abstract

The knowledge of the magnetic field generated by the main magnets of the CERN Proton Synchrotron (PS) is essential for getting better control over optical parameters of the beam. However, it is not possible in practice to predict the synchrotron working point for every set of linear and nonlinear magnetic field. A finite element analysis of the field was used for this purpose.

The ANSYS software was used to perform 2D and 3D calculations of the magnetic field. The influence of the iron packing factor on results was investigated and the 2D solution for various currents sets was compared with the experimental data. The 3D model was used for analysing the field along the beam trajectory.

Finally, the magnetic field obtained with the 2D analysis was decomposed into multipolar terms and applied in an accelerators design software, MAD, in order to recreate the basic parameters of the accelerator optics. Several limiting factors that could caused discrepancies compared to measured parameters were identified.

Acknowledgements

Contents

Chapter 1

Introduction

1.1 CERN

CERN [9] (the acronym for the French: Conseil Européen pour la Recherche Nucléaire) is the European Organization for Nuclear Research, situated on the Swiss-French border near Geneva. It was founded in 1954 under the convention signed by 12 European countries, as one of the first scientific joint ventures in Europe. Today there are 20 member states and additional 8 countries or international organizations that have a status of member state.
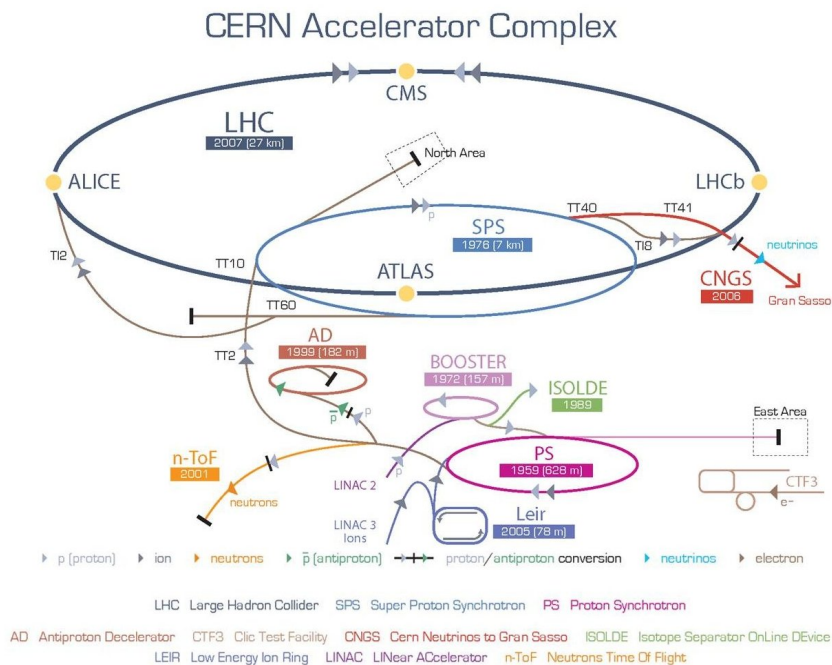
Figure 1.1: CERN accelerator complex [9].

For over 50 years CERN, which is considered to be the world's largest particle physics laboratory, has been providing the scientist with tools needed for exploration of physics fundamentals. Particle accelerators, detectors and other infrastructure are used by physicists to accelerate particles to high energies and through their collisions gain knowledge about the structure of matter. With the Large Hadron Collider (LHC), the newest addition to CERN accelerators chain, acquiring that knowledge may become possible. With the total collision energy of 14 TeV the LHC, in which the proton beams were successfully circulated for the first time on 10 September 2008, will allow to accelerate and collide protons and heavy ions.

1.2   CERN Proton Synchrotron

The Proton Synchrotron (PS) was the first synchrotron at CERN, designed to accelerate particles up to 26 GeV. It has started operation in 1959 and for many years it served as main accelerator in CERN's particle physics programme. However, since the 1970s, when new accelerators had been added to CERN complex, the PS has been supplying other machines with particles. Thanks to its versatility, the PS plays a key role in CERN injection chain shown in Fig. 1.1, being able to accelerate various types of particles and ions. Protons and ions initially accelerated in linear accelerators (LINAC2 and LINAC3) are transferred to the Proton Synchrotron Booster (PSB) and the Low-Energy Ion Ring (LEIR), respectively. The next step is the PS from which particles are injected to the Super Proton Synchrotron (SPS) and further to the LHC.
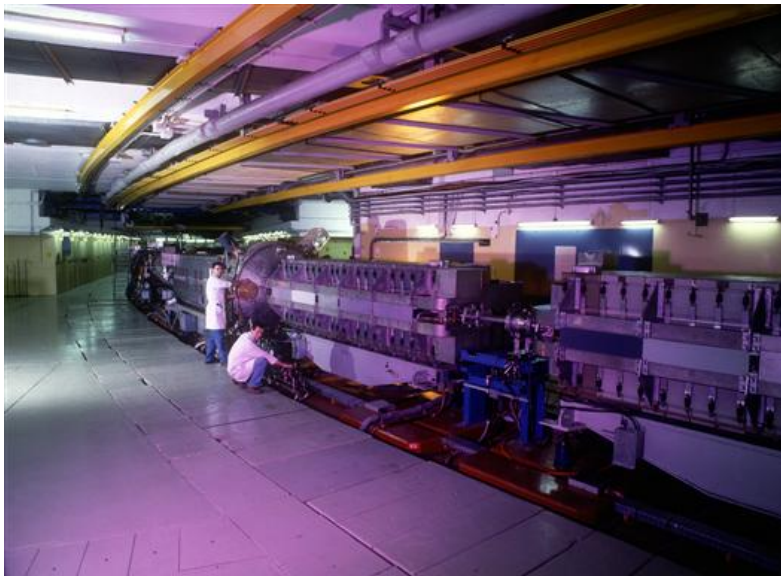
Figure 1.2: The Proton Synchrotron tunnel [9].

1.3   Aim of the thesis

The aim of the present work is to develop and apply the finite element model of the main PS magnets, which are shown in Fig. 1.2. The knowledge of magnetic field is essential for the particle dynamics calculation and future Proton Synchrotron upgrades. However, it is not possible in practice to perform measurements of the field for each set of currents feeding the magnets, so the field analysis is performed with the numerical calculation, which is less time and resource consuming.

The 2D magnetic analysis is performed using ANSYS[1] [1] software, but the model allows only to calculate the reference value of the field and its components in the magnet cross-section. For the calculation of the fringe fields at the ends of the magnet and in the junction between the two magnet halves an attempt of creating a 3D model is undertaken. For that purpose the ANSYS Workbench environment is used.

The obtained magnetic field is decomposed into its multipolar terms to model the machine lattice with the accelerator design software, such as MAD [17]. The goal of this step is to recreate basic parameters of the accelerators optics, such as tune or chromaticity, to verify if the two models, the developed magnet model and the existing optical model of the Proton Synchrotron, can be used together in beam dynamics calculation.

---

[1]developed by ANSYS, Inc.

Chapter 2

Electromagnetism and particle motion basics

2.1 Maxwell's equation in magnetostatic fields

The low frequency domain of magnetism is described by:

- Amper's law

$$\text{rot}\,\mathbf{H} = \mathbf{J}, \tag{2.1}$$

- Faraday's law

$$\text{rot}\,\mathbf{E} = -\frac{\partial \mathbf{B}}{\partial t}, \tag{2.2}$$

- Gauss's law

$$\text{div}\,\mathbf{B} = 0. \tag{2.3}$$

However, in magnetostatics the quantities are independent of time ($\partial/\partial t = 0$) and the Maxwell equations are reduced to

$$\text{rot}\,\mathbf{H} = \mathbf{J},$$
$$\text{div}\,\mathbf{B} = 0,$$

with the constitutive relation that describes the behaviour of magnetic materials

$$\mathbf{B} = \mu\mathbf{H}, \tag{2.4}$$

where $\mathbf{B}$ is the magnetic flux density, $\mathbf{H}$ is the magnetic field intensity, μ is the magnetic permeability of the medium and $\mathbf{J}$ is the electric current density.

To obtain well-posed magnetic boundary value problem the foregoing set of equations has to be completed with appropriate boundary conditions on the enclosing boundary of the analysed domain and material interface boundaries. Fig. 2.1 shows the sketch of the domain Ω of the PS magnet problem. It is divided into two subdomains: Ω_i the iron region and Ω_a the air region

($\Omega = \Omega_i \cup \Omega_a$) connected together with the interface Γ_{ai}. The domain Ω is enclosed by piecewise smooth boundary $\Gamma = \partial\Omega$. Two disjoint smooth boundaries are included in Γ: boundary denoted Γ_B with the normal component of the magnetic flux density prescribed and Γ_H with the tangential component of the magnetic field intensity constrained ($\Gamma = \Gamma_B \cup \Gamma_H$).

With the assumption that no surface electric current density is presented on Γ_{ai}, the boundary conditions are given by

$$(\mathbf{H}_a - \mathbf{H}_i) \times \mathbf{n}_{ai} = [\mathbf{H} \times \mathbf{n}]_{ai} = 0 \qquad \text{on } \Gamma_{ai}, \tag{2.5}$$

$$(\mathbf{B}_a - \mathbf{B}_i) \cdot \mathbf{n}_{ai} = [\mathbf{B} \cdot \mathbf{n}]_{ai} = 0 \qquad \text{on } \Gamma_{ai} \tag{2.6}$$

and the homogeneous boundary conditions imposed on the enclosing boundary are as follows:

$$\mathbf{H} \times \mathbf{n} = 0 \qquad \text{on } \Gamma_H, \tag{2.7}$$

$$\mathbf{B} \cdot \mathbf{n} = 0 \qquad \text{on } \Gamma_B, \tag{2.8}$$

where $\mathbf{n}$ denotes the normal vector on the domain boundary.
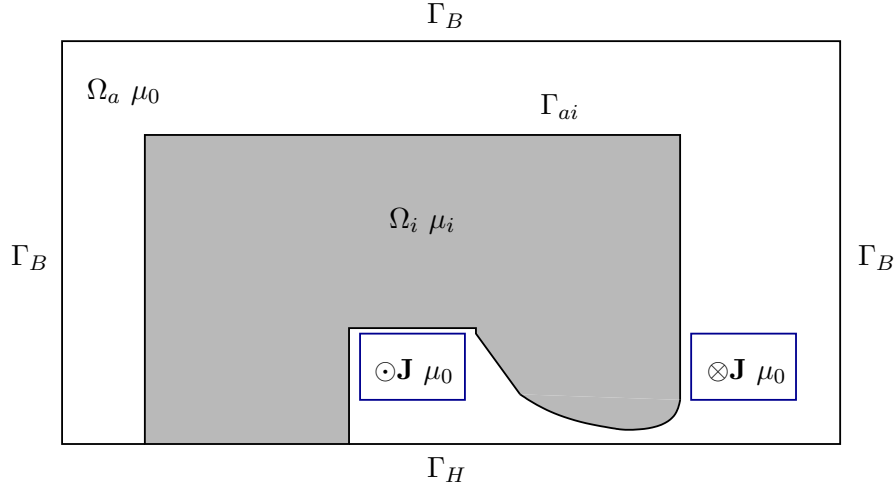
Figure 2.1: Domains and boundaries in PS magnet problem.

2.2 Total vector potential formulation

The most suitable approach for calculation of the magnetostatic fields in a domain with electric current density sources is the total vector potential formulation. By meaning of Helmholtz decomposition of a smooth vector field

$$\mathbf{F} = -\operatorname{div} \mathcal{G}(\operatorname{div} \mathbf{F}) + \operatorname{rot} \mathcal{G}(\operatorname{rot} \mathbf{F}) \tag{2.9}$$

the divergence-free magnetic field $\mathbf{B}$ can be written

$$\mathbf{B} = \operatorname{rot} \mathcal{G}(\operatorname{rot} \mathbf{B}) = \operatorname{rot} \mathbf{A} \qquad \text{in } \Omega, \tag{2.10}$$

where $\mathbf{A}$ is the vector potential and $\mathcal{G}$ represents the Newtonian potential operator. Use of Eq. (2.10) and constitutive equation $\mathbf{B} = \mu \mathbf{H}$ in Amper's law (2.1) yields the following form of partial differential equation

$$\operatorname{rot} \frac{1}{\mu} \operatorname{rot} \mathbf{A} = \mathbf{J} \qquad \text{in } \Omega. \tag{2.11}$$

However, the Maxwell equations are invariant with respect to the gauge transformation, so a gradient of any smooth scalar field ψ added to vector potential

$$\mathbf{A} \to \mathbf{A}' : \mathbf{A}' = \mathbf{A} + \operatorname{grad} \psi \tag{2.12}$$

does not change the magnetic field density $\mathbf{B}$. To guarantee the uniqueness of the boundary value problem solution an additional constraint called the Coulomb gauge has to be employed

$$\operatorname{div} \mathbf{A}' = 0. \tag{2.13}$$

The Coulomb gauge can be included in Eq. (2.11) as a penalty term [20]

$$\operatorname{rot} \frac{1}{\mu} \operatorname{rot} \mathbf{A} - \operatorname{grad} \frac{1}{\mu} \operatorname{div} \mathbf{A} = \mathbf{J} \qquad \text{in } \Omega, \tag{2.14}$$

with the set of appropriate boundary condition [25] on the enclosing boundaries

$$\mathbf{A} \cdot \mathbf{n} = 0 \qquad \text{on } \Gamma_H, \tag{2.15}$$

$$\frac{1}{\mu}(\operatorname{rot} \mathbf{A}) \times \mathbf{n} = 0 \qquad \text{on } \Gamma_H, \tag{2.16}$$

$$\frac{1}{\mu} \operatorname{div} \mathbf{A} = 0 \qquad \text{on } \Gamma_B, \tag{2.17}$$

$$\mathbf{n} \times (\mathbf{A} \times \mathbf{n}) = 0 \qquad \text{on } \Gamma_B, \tag{2.18}$$

and interface boundary

$$\left[\frac{1}{\mu}(\operatorname{rot} \mathbf{A}) \times \mathbf{n} \right]_{ai} = 0 \qquad \text{on } \Gamma_{ai}, \tag{2.19}$$

$$\left[\frac{1}{\mu} \operatorname{div} \mathbf{A} \right]_{ai} = 0 \qquad \text{on } \Gamma_{ai}, \tag{2.20}$$

$$[\mathbf{A}]_{ai} = 0 \qquad \text{on } \Gamma_{ai}. \tag{2.21}$$

2.3 Multipole expansion of a 2D magnetic field

From the solution of defined above total vector potential problem the total magnetic field vector **B** can be derived. However, this form of the field is inappropriate for certain applications, thus it has to be decomposed into its multipole terms. Multipole expansion of the field in the beam vicinity is especially required in beam dynamics, which determines the trajectory of the particle in the magnetic field.

To obtain the solution the problem has to be written by means of Laplace operator, defined over a vector field,

$$\nabla^2 \mathbf{A} = \text{grad div } \mathbf{A} - \text{rot rot } \mathbf{A}. \tag{2.22}$$

Eq. (2.14) in free space has a form

$$\nabla^2 \mathbf{A} = -\mu_0 \mathbf{J} \qquad \text{in } \Omega_a, \tag{2.23}$$

however, in two-dimensional case the vector potential **A** and current density vector **J** have only z-component, thus Eq. (2.23) is reduced to the scalar Poisson equation

$$\nabla^2 A_z = -\mu_0 J_z \qquad \text{in } \Omega_a. \tag{2.24}$$

Multipole expansion will be performed in source-free region, where Eq. (2.24) becomes the Laplace equation

$$\nabla^2 A_z = 0 \qquad \text{in } \Omega_a, \mathbf{J} = 0. \tag{2.25}$$

The Laplace equation in polar coordinates

$$\frac{\partial^2 A_z}{\partial r^2} + \frac{1}{r^2}\frac{\partial^2 A_z}{\partial \varphi^2} + \frac{1}{r}\frac{\partial A_z}{\partial r} = 0 \qquad \text{in } \Omega_a, \mathbf{J} = 0. \tag{2.26}$$

can be solved using the variables separation method. Potential A_z in Eq. (2.26) can be replaced by the product of two function with separate variables

$$A_z(r, \varphi) = w(r)v(\varphi) \tag{2.27}$$

and after differentiating and regrouping, both sides of equation are equal to non-zero separation constant n^2

$$\frac{1}{w(r)}\left(r^2\frac{\partial^2 w(r)}{\partial r^2} + r\frac{\partial w(r)}{\partial r}\right) = n^2 = -\frac{1}{v(\varphi)}\frac{\partial^2 v(\varphi)}{\partial \varphi^2} \tag{2.28}$$

This gives a set of two ordinary differential equations with separate variables

$$r^2\frac{\partial^2 w(r)}{\partial r^2} + r\frac{\partial w(r)}{\partial r} - n^2 w(r) = 0 \tag{2.29}$$

$$\frac{\partial^2 v(\varphi)}{\partial \varphi^2} + n^2 v(\varphi) = 0 \tag{2.30}$$

The solution of Eqs. (2.29) and (2.30) have the following form

$$w(r) = \mathcal{E}r^n + \mathcal{F}r^{-n} \tag{2.31}$$

$$v(\varphi) = \mathcal{G}\sin n\varphi + \mathcal{H}\cos n\varphi \tag{2.32}$$

however, with the boundary condition imposed on the potential, that is finite at $r = 0$ and periodic in angular coordinate φ [13], the general solution is a series expansion of potential A_z

$$A_z(r,\varphi) = \sum_{n=1}^{\infty} r^n (\mathcal{C}_n \sin n\varphi - \mathcal{D}_n \cos n\varphi). \tag{2.33}$$

Components of the field **B** in polar coordinates are obtained as below

$$B_r(r,\varphi) = \frac{1}{r}\frac{\partial A_z}{\partial \varphi} = \sum_{n=1}^{\infty} n r^{n-1}(\mathcal{C}_n \cos n\varphi + \mathcal{D}_n \sin n\varphi), \tag{2.34}$$

$$B_\varphi(r,\varphi) = -\frac{\partial A_z}{\partial r} = \sum_{n=1}^{\infty} n r^{n-1}(\mathcal{C}_n \sin n\varphi - \mathcal{D}_n \cos n\varphi). \tag{2.35}$$

This shows that the magnetic field can be locally expressed with the series of n-fold rotational symmetric fields. Constants $\mathcal{C}_n$ and $\mathcal{D}_n$ are coefficients of the skew and the normal multipole, respectively, where the skew multipole is rotated by $\pi/(2n)$ with respect to the normal multipole component.

The knowledge of the flux distribution generated by magnets is crucial to perform the analysis of the particle motion, since different orders of multipoles have various influence on the beam parameters. Pure dipole, quadrupole and sextupole fields, generated with magnets of appropriate pole shape to respectively bend, focus the beam and adjust its chromaticity, are shown in Fig. 2.2.
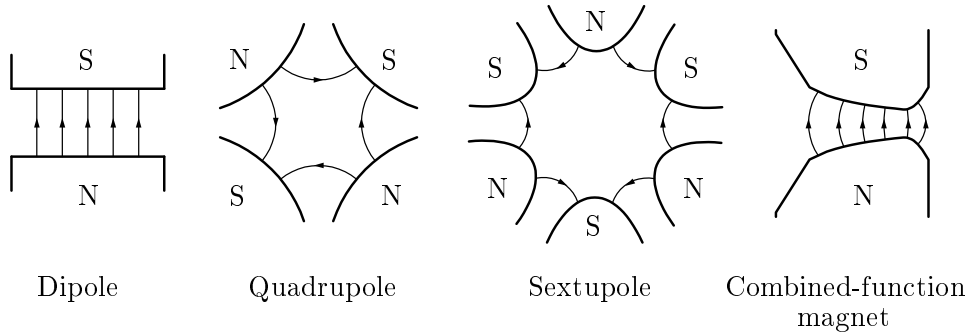

Figure 2.2: Schematic pole shapes of magnets.

Multipole	Skew magnets	Normal magnets
Dipole, n=1	$B_x = \mathcal{C}_1$ $B_y = 0$	$B_x = 0$ $B_y = \mathcal{D}_1$
Quadrupole, n=2	$B_x = 2\mathcal{C}_2 x$ $B_y = -2\mathcal{C}_2 y$	$B_x = 2\mathcal{D}_2 y$ $B_y = 2\mathcal{D}_2 x$
Sextupole, n=3	$B_x = 3\mathcal{C}_3(x^2 - y^2)$ $B_y = -6\mathcal{C}_3 xy$	$B_x = 6\mathcal{D}_3 xy$ $B_y = 3\mathcal{D}_3(x^2 - y^2)$
Octupole, n=4	$B_x = 4\mathcal{C}_4(x^3 - 3xy^2)$ $B_y = -4\mathcal{C}_4(3x^2 y - y^3)$	$B_x = 4\mathcal{D}_4(3x^2 y - y^3)$ $B_y = 4\mathcal{D}_4(x^3 - 3xy^2)$
Decapole, n=5	$B_x = 5\mathcal{C}_5(x^4 - 6x^2 y^2 + y^4)$ $B_y = -20\mathcal{C}_5(x^3 y - xy^3)$	$B_x = 20\mathcal{D}_5(x^3 y - xy^3)$ $B_y = 5\mathcal{D}_5(x^4 - 6x^2 y^2 + y^4)$

Table 2.1: Multipole fields in skew and normal magnets.

Magnetic field components transformed to Cartesian coordinates, more convenient for beam optics, are written in Table 2.1. However, it is usually impossible to generate pure multipole field in a real-world magnets, because not all of unwanted components can be eliminated and they have to be minimized in the design process of the magnet.

There are also magnets designed to generate both the dipole and the quadrupole field components called combined-function magnets. Such design, which was also used in the CERN Proton Synchrotron, allows to make accelerator equipment more compact but makes the machine tuning more difficult compared to separate quadrupole and dipole magnets, which is why it is no longer used in most present-day accelerators.

2.4 Beam optics basics[1]

A particle accelerator lattice is a set of bending and focusing magnets. The design of the lattice is done to keep the particles close to desired reference path. In synchrotrons this path is called the reference orbit and it is defined by bending magnets.

The motion of a charged particle in the electromagnetic field $(\mathbf{E}, \mathbf{B})$ is governed by the Lorentz force

$$\mathbf{F} = \frac{d\mathbf{p}}{dt} = e\mathbf{E} + \frac{e}{c}(\mathbf{v} \times \mathbf{B}), \tag{2.36}$$

---

[1]The accelerator physics goes beyond the aim of this study. Only a very brief introduction is given here.
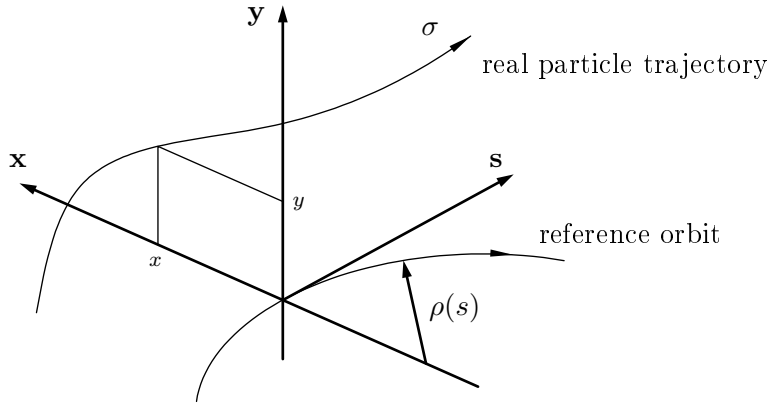
Figure 2.3: Coordinate system.

where $\mathbf{p} = \gamma m \mathbf{v}$ is the relativistic momentum, $\mathbf{v}$ is the velocity, m is the mass, $\gamma = 1/\sqrt{1 - v^2/c^2}$ is the relativistic Lorentz factor with c the speed of light.

2.4.1 Coordinate system

It is convenient to describe the beam dynamics in an orthogonal, right-handed coordinate system $(\mathbf{x}, \mathbf{y}, \mathbf{s})$ shown in Fig. 2.3. In such coordinate system, the vector $\mathbf{s}$ is tangential to the reference path and the system follows the reference particle travelling along it. Particle motion takes place in two planes that can be distinguished in the coordinate system: transversal and longitudinal. In the transversal plane, the particles that are moving along the reference orbit with different transverse momentum make small-amplitude oscillations around the orbit. These transverse oscillations, which are called the betatron oscillations, are governed by the Hill equation described in Section 2.4.3.

2.4.2 Bending and alternating-gradient focusing

The reference particle in a synchrotron is circulating along the closed orbit within the horizontal mid-plane, where $y = 0$. In this plane, when purely vertical magnetic field is taken into account, the curvature and the bending radius for the particle trajectory are

$$\kappa_x = \frac{e}{cp} B_y \tag{2.37}$$

and

$$\frac{1}{\rho_x} = \left| \frac{e}{cp} B_y \right|. \tag{2.38}$$

Particle beams, similar to light rays, have a natural divergence and a tendency to spread out. To prevent particles from deviating, the focusing lenses,

such as quadrupole magnets, can be used. In such magnets, the deflection of the particle trajectory increases linearly with the distance from the reference orbit and can be expressed by means of the focusing strength

$$k = \frac{e}{cp}g = \frac{e}{cp}\frac{\partial B_y}{\partial x}, \tag{2.39}$$

where $g = \partial B_y/\partial x$ is the field gradient. The magnetic field of such a quadrupole has the form

$$\begin{aligned} \frac{e}{cp}B_x &= ky, \\ \frac{e}{cp}B_y &= kx. \end{aligned} \tag{2.40}$$

However, the quadrupole magnets are focusing the beam in one plane while defocusing it in the other one, thus the alternating-gradient focusing has to be used. From the light optics it is known that the combined focal length of two lenses with the focal lengths f_1 and f_2, separated by a distance d can be written as

$$\frac{1}{f} = \frac{1}{f_1} + \frac{1}{f_2} - \frac{d}{f_1 f_2} \tag{2.41}$$

in a specific case when $f_1 = -f_2$ the total focal length is positive and equal $f = f_1^2/d$ which indicates that it is possible to select the focal lengths in such a way to make the set of lenses focusing. The same principle can be referred to a quadrupole doublet. When field gradients g are chosen appropriately the doublet is focusing in both horizontal and vertical planes as shown in Fig. 2.4.

2.4.3 Equation of motion

The general equation for transverse motion of charged particles in electromagnetic field is called the Hill equation. It can be derived from Lorentz force (2.36) and its linear unperturbed form is

$$\begin{aligned} x'' + K_x(s)x &= 0, \\ y'' + K_y(s)y &= 0, \end{aligned} \tag{2.42}$$

where x'' and y'' are second derivatives with respect to s, K_x and K_y are s-dependent functions of field strength coefficients. In the synchrotrons with combined-function magnets, which deflect only in horizontal plane, these functions are periodical and given by

$$\begin{aligned} K_x(s) &= \kappa_x^2(s) + k(s), \\ K_y(s) &= -k(s). \end{aligned} \tag{2.43}$$

The solution of the Hill equation (2.42) satisfies the Floquet theorem [18] and can be expressed as

$$u(s) = \sqrt{\epsilon\beta(s)}\cos\left(\psi(s) + \phi\right), \tag{2.44}$$
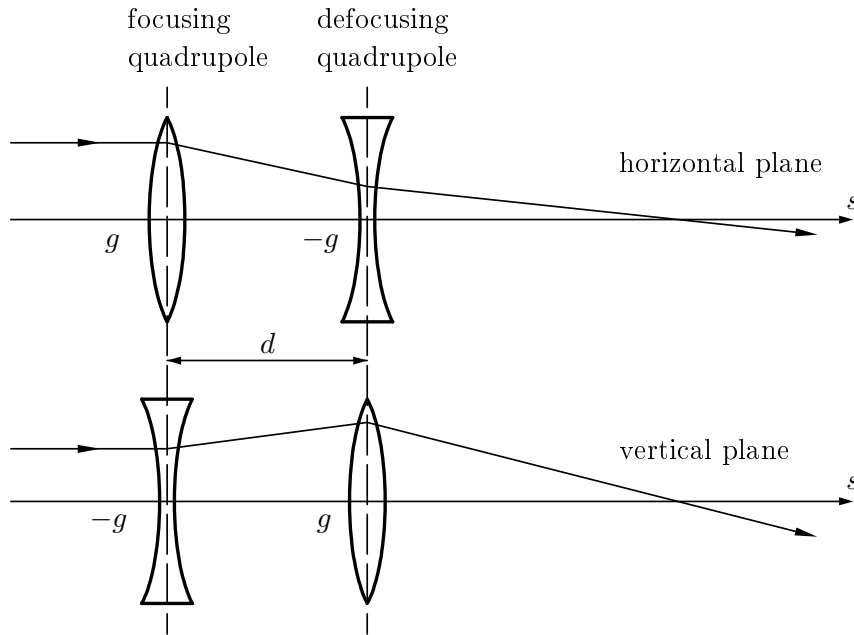
Figure 2.4: Quadrupole doublet.

where u stands for x or y, ϵ is the beam emittance, $\beta(s)$ is called betatron function, which expresses the amplitude modulation due to periodically changing focusing strength, and $\psi(s)$ is the phase advance also dependent on focusing strength and ϕ is a constant dependent on the initial conditions,. This solution, together with $u'(s)$, describes the betatron oscillation of a particle around the reference orbit in the plane uu'.

Eq. (2.42) is derived for a particle with design momentum p_0. However, circulating beams are never perfectly mono-energetic. For particles that have non-zero momentum spread Δp, a momentum deviation $\delta = \Delta p/p_0$ has to be taken into consideration. The perturbed equation of motion has following form

$$u'' + K(s)u = \frac{\delta}{\rho}. \tag{2.45}$$

The solution of Eq. (2.45) can be obtained using Green's function method, detailed description of which can be found in [28].

2.4.4   Beam parameters

The physical parameters which describe the beam behaviour in a synchrotron:

- **Tune** which is a parameter defined as the number of betatron oscillation in one machine revolution. If we suppose that an accelerator has a

circumference C, the betatron tune is

$$Q = \frac{1}{2\pi} \int_s^{s+C} \frac{ds}{\beta(s)} \tag{2.46}$$

and can be written both for the horizontal and the vertical oscillations. This parameter depends on the betatron function $\beta(s)$ so it can be controlled with the focusing strength of the quadrupole magnets.

- **Chromaticity** which is the variation of betatron tune with the momentum and in relative form it is defined as

$$\xi = \frac{\Delta Q/Q}{\Delta p/p_0}. \tag{2.47}$$

The beam chromaticity can be controlled by sextupole magnets.

Chapter 3

The finite element method in 2D magnetostatics

The finite element method is one of the most effective and versatile numerical techniques of approximate solving differential equations that model many problems in the field of physics and engineering.

In this method the geometrical domain of the problem is subdivided into smaller subdomains, called finite elements, in which the unknown variables are approximated using known linear or, if necessary, higher order functions. The governing equations are integrated over each element and then assembled together along with associated boundary conditions into a set of linear equations that can be solved using linear algebra techniques. These equations are formulated using variational methods, which are based on a minimization of a particular functional that describes the phenomena, or residual methods, that are established directly from the physical equations and notion of these methods is to minimize the residual.

3.1   Finite element discretization

The 2D domain of the boundary value problem is discretized with finite element mesh, that should accurately represent the shape of the domain. The mesh is constructed of triangular or quadrilateral elements, that can be used together in the same mash as well.

Depending on the chosen element type the proper interpolation functions must be developed. These functions must satisfy certain key requirements:

- they must guarantee continuity of unknown variables across boundaries between elements,

- they must be differentiable up to the order $n - 1$, where n is the order of the governing differential equation,

- they must be complete polynomials.

Development of the interpolation functions will be performed for bilinear quadrilateral element, which is shown in Fig. 3.1. The element will be considered isoparametric, thus the interpolation functions, which are used to interpolate the primary unknown quantity, are identical to shape functions which are used for mapping the shape and position of the element between local and global coordinating system.
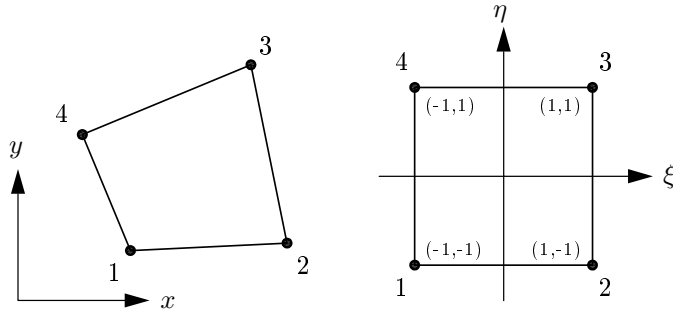
Figure 3.1: Quadrilateral element in xy-plane and $\xi\eta$-plane.

A general shape function in local coordinating system has the form

$$N(\xi,\eta) = c_1 + c_2\xi + c_3\eta + c_4\xi\eta, \tag{3.1}$$

and is equal 1 at a particular node and zero at all others. Therefore, considering the function for node 1, a set of four equations can be written.

$$\begin{aligned}
N_1(-1,-1) &= c_1 - c_2 - c_3 + c_4 = 1 \\
N_1(1,-1) &= c_1 + c_2 - c_3 - c_4 = 0 \\
N_1(1,1) &= c_1 + c_2 + c_3 + c_4 = 0 \\
N_1(-1,1) &= c_1 - c_2 + c_3 - c_4 = 0
\end{aligned} \tag{3.2}$$

The solution gives missing constants

$$c_1 = \frac{1}{4}, \quad c_2 = -\frac{1}{4}, \quad c_3 = -\frac{1}{4}, \quad c_4 = \frac{1}{4}, \tag{3.3}$$

and the interpolation function for node 1 can be written as

$$N_1(\xi,\eta) = \frac{1}{4}(1-\xi)(1-\eta). \tag{3.4}$$

Using the same approach, all four bilinear interpolation functions can be obtained

$$N_1(\xi, \eta) = \frac{1}{4}(1 - \xi)(1 - \eta)$$

$$N_2(\xi, \eta) = \frac{1}{4}(1 + \xi)(1 - \eta)$$

$$N_3(\xi, \eta) = \frac{1}{4}(1 + \xi)(1 + \eta)$$

$$(3.5)$$

$$N_4(\xi, \eta) = \frac{1}{4}(1 - \xi)(1 + \eta)$$

and in terms of these functions the primary unknown quantity interpolation and coordinates transformation can be written as

$$A = \sum_{j=1}^{4} A_j^e N_j \tag{3.6}$$

and

$$x = \sum_{j=1}^{4} x_j^e N_j, \quad y = \sum_{j=1}^{4} y_j^e N_j. \tag{3.7}$$

3.2   The Galerkin method

The Galerkin approach of the weighted residual method is widely used in electromagnetism due to its simplicity and practicality. The finite element equations are derived from physical equation

$$\text{rot} \frac{1}{\mu} \text{rot} \mathbf{A} = \mathbf{J} \qquad \text{in } \Omega, \tag{3.8}$$

which in 2D automatically fulfils the Coulomb gauge ($\frac{\partial}{\partial z} = 0$) and can be written in cartesian coordinates as follows

$$\frac{\partial}{\partial x} \left(\frac{1}{\mu} \frac{\partial A_z}{\partial x} \right) + \frac{\partial}{\partial y} \left(\frac{1}{\mu} \frac{\partial A_z}{\partial y} \right) = -J_z, \tag{3.9}$$

where A_z and J_z are z-components of the magnetic vector potential and the current density vector, respectively. The residual for a single element has the form

$$\mathcal{R}^e = \frac{\partial}{\partial x} \left(\frac{1}{\mu} \frac{\partial A_z}{\partial x} \right) + \frac{\partial}{\partial y} \left(\frac{1}{\mu} \frac{\partial A_z}{\partial y} \right) + J_z, \tag{3.10}$$

which then has to be multiplied by a weight function $w(x, y)$, integrated over the element domain and forced to be zero

$$\iint_{\Omega^e} w \left[\frac{\partial}{\partial x} \left(\frac{1}{\mu} \frac{\partial A_z}{\partial x} \right) + \frac{\partial}{\partial y} \left(\frac{1}{\mu} \frac{\partial A_z}{\partial y} \right) + J_z \right] \mathrm{d}x\mathrm{d}y = 0. \tag{3.11}$$

Transforming Eq. (3.11) and applying the Green theorem yields

$$\iint_{\Omega^e} \frac{1}{\mu} \left(\frac{\partial w}{\partial x} \frac{\partial A_z}{\partial x} + \frac{\partial w}{\partial y} \frac{\partial A_z}{\partial y} \right) \mathrm{d}x\mathrm{d}y$$

$$= \iint_{\Omega^e} wJ_z \mathrm{d}x\mathrm{d}y + \oint_{\Gamma^e} w\frac{1}{\mu} \left(\frac{\partial A_z}{\partial x} n_x + \frac{\partial A_z}{\partial y} n_y \right) \mathrm{d}s, \tag{3.12}$$

which is the weak form of the differential equation. The boundary integral in Eq. (3.12) vanishes due to boundary conditions (2.17) and (2.20). The remaining two boundary conditions that have to be considered in the 2D case are

$$\mathbf{A} \cdot \mathbf{n} = 0 \qquad \text{on } \Gamma_H, \tag{3.13}$$

$$\mathbf{n} \times (\mathbf{A} \times \mathbf{n}) = 0 \qquad \text{on } \Gamma_B. \tag{3.14}$$

The first condition (3.13) is automatically fulfilled since $\mathbf{n} \perp \mathbf{e}_z$, while the condition (3.14) reduces to the form $A_z = 0$.

In the Galerkin method both the weight functions w and the unknown vector potential A_z must be expressed with the same set of shape functions. Therefore,

$$A_z = \sum_{j=1}^{n} A_{zj}^e N_j \tag{3.15}$$

and

$$w = N_i \quad \text{for } i = 1, 2, , n \tag{3.16}$$

where n is the number of the nodes in element type used. Substituting Eqs. (3.15) and (3.16) into Eq. (3.12), the discretized weak form of the governing differential equation for a single element can be conveniently expressed in a matrix form

$$\begin{bmatrix} K_{11}^e & K_{12}^e & \cdots & K_{1n}^e \\ K_{21}^e & K_{22}^e & \cdots & K_{2n}^e \\ \vdots & \vdots & \ddots & \vdots \\ K_{n1}^e & K_{n2}^e & \cdots & K_{nn}^e \end{bmatrix} \begin{Bmatrix} A_{z1}^e \\ A_{z2}^e \\ \vdots \\ A_{zn}^e \end{Bmatrix} = \begin{Bmatrix} F_1^e \\ F_2^e \\ \vdots \\ F_n^e \end{Bmatrix} \tag{3.17}$$

where

$$K_{ij}^e = \iint_{\Omega^e} \frac{1}{\mu} \left(\frac{\partial N_i}{\partial x} \frac{\partial N_j}{\partial x} + \frac{\partial N_i}{\partial y} \frac{\partial N_j}{\partial y} \right) \mathrm{d}x\mathrm{d}y \tag{3.18}$$

is called the element stiffness matrix and

$$F_i^e = \iint_{\Omega^e} N_i J_z \mathrm{d}x\mathrm{d}y \tag{3.19}$$

is the element force vector.

To evaluate the element matrix and the vector for the bilinear quadrilateral element, which was described in Section 3.1, it is convenient to change the integration variables from x and y to ξ and η. For that purpose the Jacobi transformation matrix $\mathbf{J}_t$ has to be introduced

$$\left\{\begin{array}{c} \frac{\partial N_i}{\partial \xi} \\[2mm] \frac{\partial N_i}{\partial \eta} \end{array}\right\} = \begin{bmatrix} \frac{\partial x}{\partial \xi} & \frac{\partial y}{\partial \xi} \\[2mm] \frac{\partial x}{\partial \eta} & \frac{\partial y}{\partial \eta} \end{bmatrix} \left\{\begin{array}{c} \frac{\partial N_i}{\partial x} \\[2mm] \frac{\partial N_i}{\partial y} \end{array}\right\} = \begin{bmatrix} \mathbf{J}_t \end{bmatrix} \left\{\begin{array}{c} \frac{\partial N_i}{\partial x} \\[2mm] \frac{\partial N_i}{\partial y} \end{array}\right\} \tag{3.20}$$

where x and y are space coordinates expanded in terms of the shape functions N_i. Using the Jacobi transformation the element matrix and the vector can be expressed as

$$K_{ij}^e = \int_{-1}^{1} \int_{-1}^{1} \frac{1}{\mu} \left(\frac{\partial N_i}{\partial x}\frac{\partial N_j}{\partial x} + \frac{\partial N_i}{\partial y}\frac{\partial N_j}{\partial y} \right) |\mathbf{J}_t|\mathrm{d}\xi\mathrm{d}\eta \tag{3.21}$$

and

$$F_i^e = \int_{-1}^{1} \int_{-1}^{1} N_i J_z |\mathbf{J}_t|\mathrm{d}\xi\mathrm{d}\eta \tag{3.22}$$

and then numerically evaluated using the Gauss quadrature method.

3.3   Assembling the global matrix

Once the governing equations have been developed for each individual element, the element stiffness matrices and the element force vectors must be merged into a single global stiffness matrix and a global force vector. Assembled global system is usually presented in the following form:

$$[\mathbf{K}]\{\mathbf{A}\} = \{\mathbf{F}\} \tag{3.23}$$

where $\mathbf{K}$ is the global stiffness matrix, which is symmetric and sparse, $\mathbf{A}$ is the global vector of A_z degree of freedom and $\mathbf{F}$ is the global force vector. After imposing the boundary condition $A_z = 0$ on all global nodes that lie on the boundary Γ_B, the equations of the system can be solved using direct or iterative numerical techniques.

Chapter 4

Magnet characterization

The main magnetic part of the Proton Synchrotron is a structure of 100 magnet units placed in a tunnel that forms a ring of 200 m in diameter. Each unit is a combined-function, normal conducting magnet composed of two half-units: focusing (F) and defocusing (D) rigidly joined together. Such design allows to bend and focus particle beam at the same time to keep required radius and size. The magnets are arranged in a lattice FOFDOD with field-free, straight sections (O) between them, where auxiliary equipment is situated.
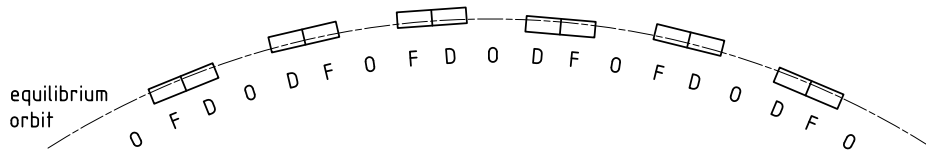
Figure 4.1: The sequence of magnets in the PS accelerator.

4.1 PS unit geometry

Each half-magnet unit consists of 5 adjacent identical magnet structures, called blocks, separated from each other by a wedge-shaped air gap. A block is straight C-shaped structure, 417 mm long, of open or closed type. Such construction gives an arc shape to a magnetic unit, where blocks are so arranged that axes of the magnet gaps are tangent to magnetic circumference of the machine ($r_0 = 70.0789$ m). The magnet half-units do not have the same length. Air gaps between blocks of the same type in focusing half are 7.75 mm long while in defocusing half 9.75 mm. Focusing and defocusing sectors are separated by 20 mm straight air gap called central junction.

19

Figure 4.2: The Proton Synchrotron magnet unit [21].

Open block   Closed block

Figure 4.3: The iron block types.

4.2   Pole profile

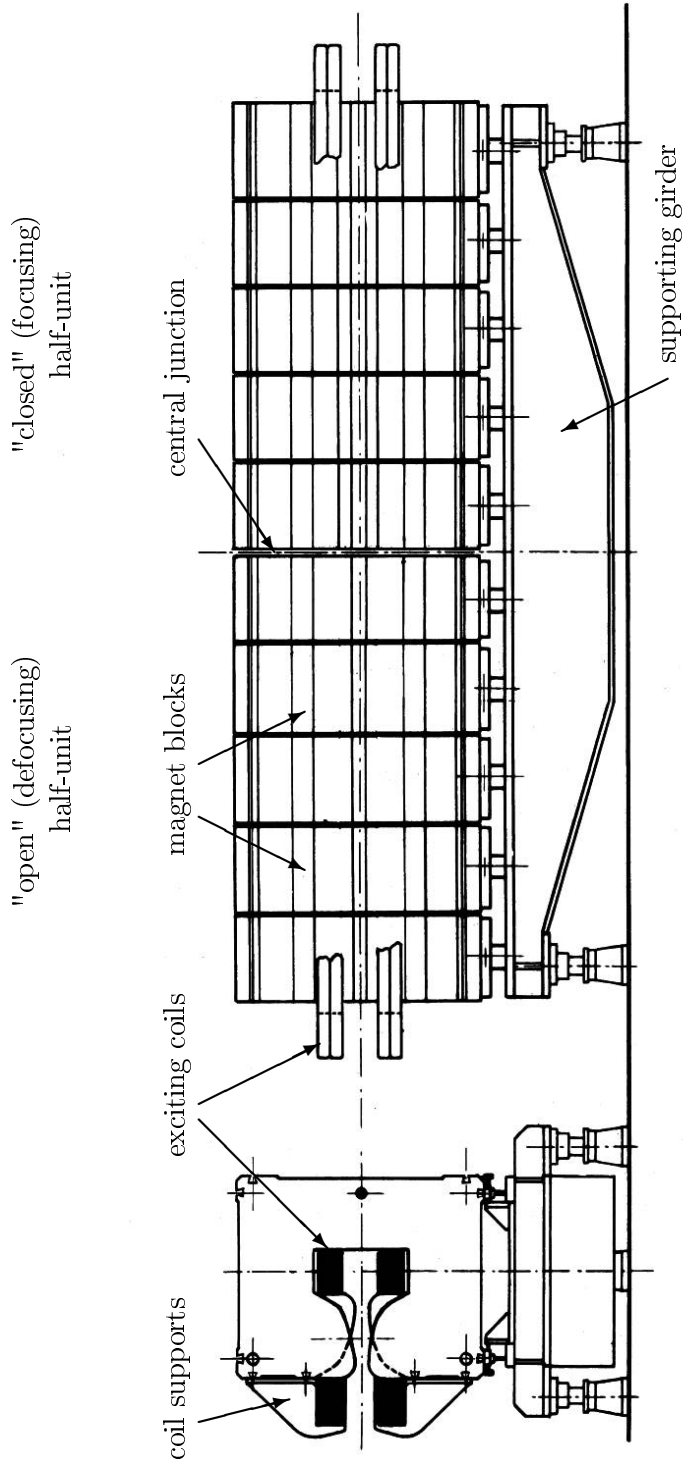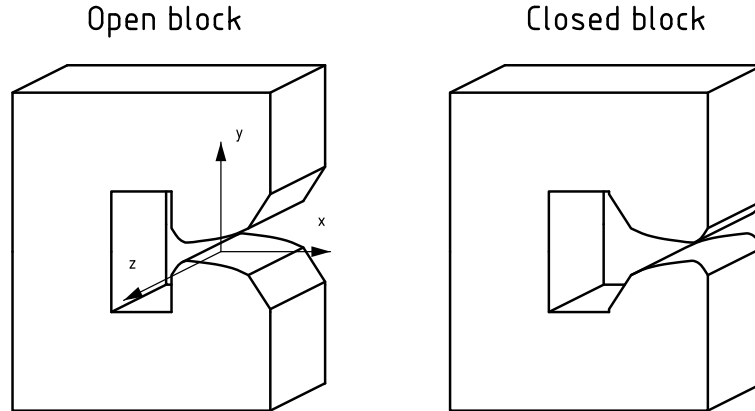The most important factor that determines the field shape is a pole profile. In both block types, open and closed, the geometry of the pole is the same. It has been designed to produce the linear field and keep the focusing strength coefficient k constant over the largest region possible. Obtaining strictly linear field is in this case impossible due to finite permeability of the steel, the coils and the saturation of the core. All of these factors introduce non-linearities. Thus, the final profile contains hyperbolic contour, which provides the quadrupole component of the main field. The central part of the pole is responsible for the field at the equilibrium orbit, while the narrow part reduces the saturation in external pole region and the wide truncated part increases the fall of the radial field on the opposite side, where it was too small.

4.3   Different units

Four different magnet types, denoted by letters: R, S, T and U, can be distinguished depending on the half-units order and the location of the iron core with respect to the beam orbit. There are 35 units of both R and T type and 15 units of both S and U type installed in the tunnel. Magnets with the iron core external to the ring are signed R and S, while those with internal core are called T and U. Units R and U have defocusing sector upstream and focusing downstream while S and T units have their half-units inversely.
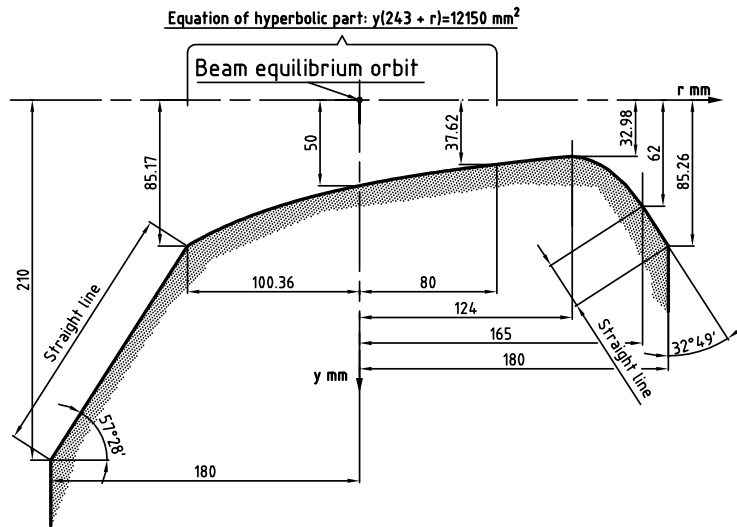
Figure 4.4: Pole profile [7].

4.4   Exciting coils

All 10 blocks of magnetic unit are excited by the same two main coils. One of them is wound around the top pole piece and the other is placed on the bottom pole piece. A single coil consists of two layers called pancakes. They are made up of 5 turns of the conductor, an aluminium rod of 55 x 38 mm cross-section with a hole of 12 mm in diameter used as a cooling line. All main coils are electrically connected in series while the cooling system is connected in parallel. Each turn of conductor as well as the pancake is insulated by several layers of paper-mica-paper and vacuum impregnated with polyester resign. This makes pancakes as rigid as possible and reduces relative movement of individual conductors caused by thermal and magnetic effects.

Apart from the main coil, which is used to generate the dipolar field and the main quadrupolar field, there are two types of auxiliary windings: the figure-of-eight-loop (f8) and pole-face windings (pfw). They are used to adjust and correct the harmonics of the field and to control four optical parameters of the beam, tunes and chromaticities in horizontal and vertical plane.

The figure-of-eight-loop is installed around both top and bottom pole profile. As its name suggests, it has the shape of an 8, thus it goes around the pole faces of focusing and defocusing half-unit and crosses between them. Because of that, currents inside loops around the two poles have different sign so they
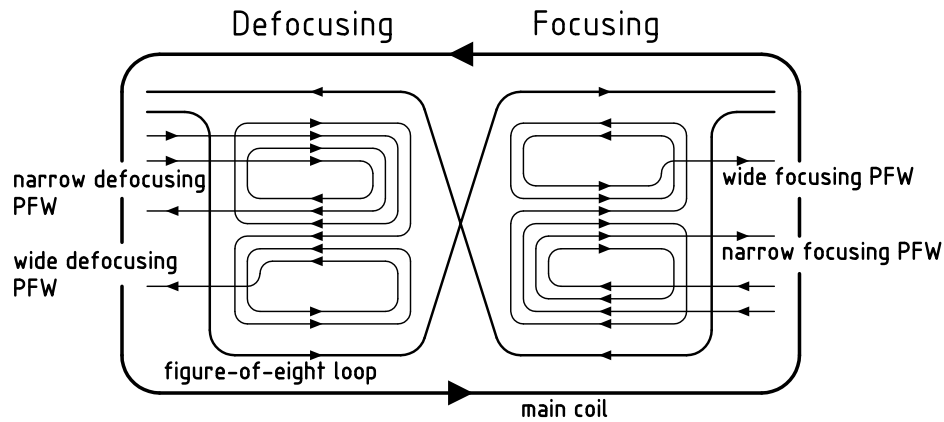
Figure 4.5: Sketch of the magnet windings.

generate opposite fields in each half-unit. The figure-of-eight-loop affects the magnetic field and its quadrupole component therefore it is used to control horizontal and vertical tune.

The second type of auxiliary coils are the pole-face windings. Each magnet has four pole-face windings plates mounted on the pole surface of focusing and defocusing half-unit. Each plate has two separate circuits called narrow and wide. They consist of an arrangement of parallel copper bars, which have cross-section of 9 x 3 mm, embedded in an insulating sheet of polyester resign. Pole-face windings mainly affect quadrupole and sextupole field component, thus they are used in adjustment of all four optical parameters.

Figure 4.6: Cross-section of the pole-face-windings plate [7].

Impurity	Amount
carbon	0.06%
manganese	0.30%
sulphur	0.025%
phosphorus	0.010%

Table 4.1: The amount of the steel impurities [22].

The working point of the machine is controlled using these two auxiliary windings. When narrow and wide circuits of pole-face windings are connected in series, three currents (I_{pfwF}, I_{pfwD} and I_{f8}) are governing four parameters (Q_h,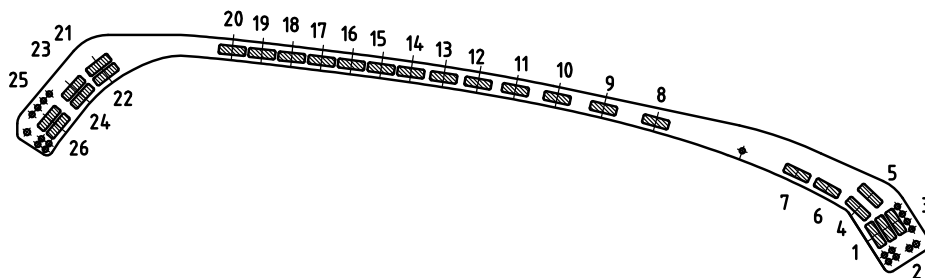 Q_v, ξ_h, ξ_v), which leaves one physical quantity free. Such powering scheme is called the 3-current mode. However, it is possible to power those circuits separately. The application of the 5-current mode (I_{pfwFN}, I_{pfwFW}, I_{pfwDN}, I_{pfwDW} and I_{f8}), which gives more freedom in the working point adjustment, has just started.

4.5 The PS magnet steel

The characteristics of the rimming steel [22] that was used for all of the PS magnets is shown in Table 4.1. It had been cold worked to the critical degree of deformation and subsequently annealed at the temperature of about $750\,°C$ in order to increase the grain size and eliminate the internal stresses, which could contribute to a decrease in permeability for low induction and an increase in the coercive force.

The blocks are made up of laminations insulated by paper and stuck together with hot-setting resin (araldite). They had to be suitably mixed during blocks manufacturing to obtain statistical uniformity of magnetic properties and decrease variations in average performance from one block to another. To reduce induced eddy currents, which are created under dynamic conditions, thickness of a single sheet of steel had been set to 1.5 mm.

Chapter 5

Numerical model

5.1 Finite element magnet model

A 2-dimensional numerical model of the PS magnet was created using ANSYS, a general-purpose finite-element analysis software package. ANSYS has wide application in diverse mechanical as well as electromagnetic problems. The geometry was based on technical documentation [21][22] and drawings [7]. It contains upper half of symmetric iron core and all types of exciting coils as well as a finite air region surrounding the magnet. The fragment of geometry with the close-up of the pole piece and exciting coils is shown in Fig. 5.1.
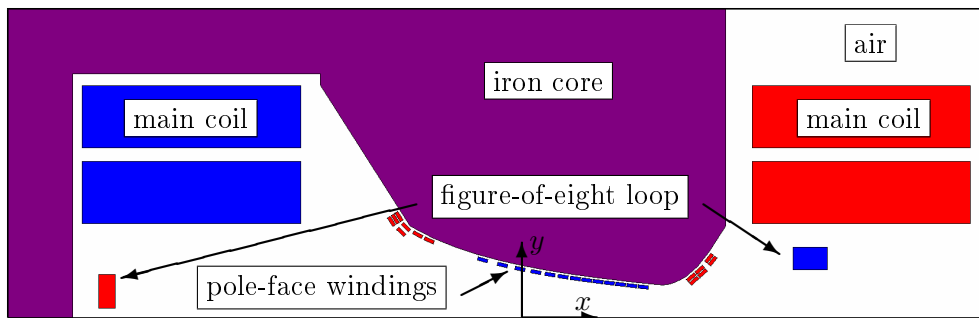
Figure 5.1: The fragment of the focusing half-unit model geometry.

The finite element model was created using 8-node quadrilateral and 6-node triangular PLANE53 elements [1]. This type of element is suitable for the magnetic field calculation with the total vector potential formulation and has up to 4 degrees of freedom at each node, but in static analysis only the vector potential (AZ) is used. The element is capable of modelling materials with nonlinear magnetic properties defined with BH curves.
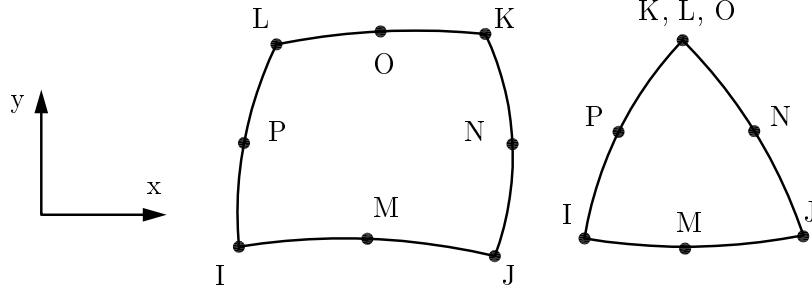
Figure 5.2: The PLANE53 element geometry.

5.2 Magnetic properties of the steel

5.2.1 Packing factor

Laminated iron yoke consists of layers of two different materials, thereby average material properties are strongly dependent on the direction. Between each iron plate of thickness l_{Fe}, which is considered to have isotropic permeability μ_{Fe}, there is a layer of insulating paper of thickness l_0 and permeability μ_0. The influence of laminated structure can be described with a packing factor defined by

$$\lambda = \frac{l_{Fe}}{l_{Fe} + l_0} \tag{5.1}$$

and by means of the packing factor we define the average permeability in the lamination plane

$$\overline{\mu}_x = \overline{\mu}_y = \lambda\mu_{Fe} + (1 - \lambda)\mu_0 \tag{5.2}$$

and in z-direction

$$\overline{\mu}_z = \left(\frac{\lambda}{\mu_{Fe}} + \frac{1 - \lambda}{\mu_0} \right)^{-1} \tag{5.3}$$

The magnetic flux density **B** in anisotropic material is calculated from

$$\mathbf{B} = [\mu]\mathbf{H} \tag{5.4}$$

where $[\mu]$ is the permeability 2nd rank tensor

$$[\mu] = \begin{bmatrix} \overline{\mu}_x & 0 & 0 \\ 0 & \overline{\mu}_y & 0 \\ 0 & 0 & \overline{\mu}_z \end{bmatrix} \tag{5.5}$$

Estimation of the packing factor value is not precise since the number of laminations within blocks is inaccurate. In the technical documentation [21]
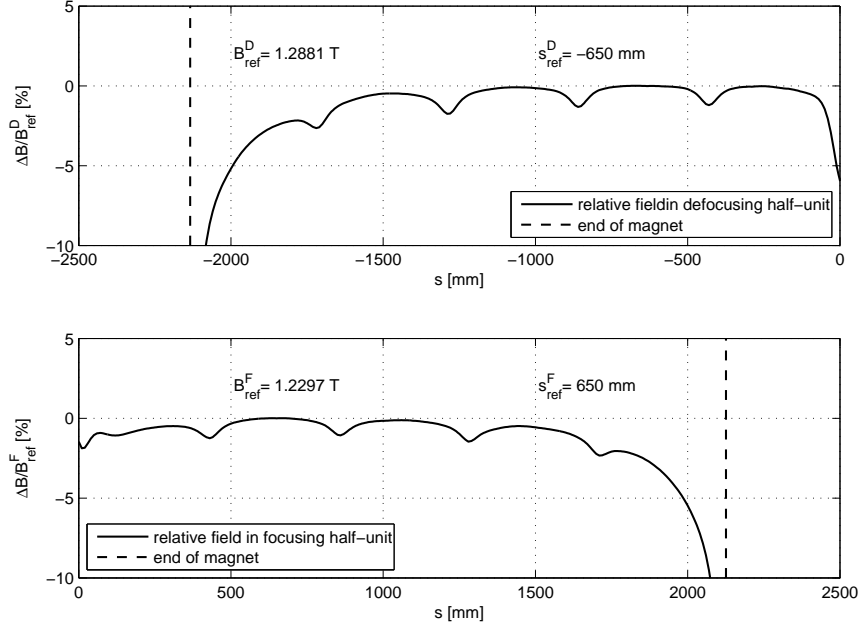
Figure 5.3: Relative field in defocusing and focusing half-unit.

we find information that a single finished block, which is 417 mm long, theoretically contains 264 steel plates of 1.5 mm thickness, but according to other report [22] this number may vary within the range $262 \le n_{lam} \le 272$.

When we take a single block with 264 laminations into consideration, the packing factor is calculated as follows

$$\lambda = \frac{264 \times 1.5mm}{417mm} \approx 0.9496. \tag{5.6}$$

However, this value can be used only in the 3D simulation, where individual blocks are modelled, as well as air gaps between them, while the 2D model represents a cross-section of an infinitely long, continuous magnet. The only way to introduce the influence of air to the calculated magnetic field is through the packing factor. Its average value can be estimated as below

$$\lambda = \frac{264 \times 1.5mm \times 10}{417mm \times 10 + (7.75mm + 9.75mm) \times 4 + 20} \approx 0.9296 \tag{5.7}$$

This value is close to the packing factor $\lambda = 0.925$ that was used in the PS magnet simulation done in the past [10] using POISSON Superfish code[1]. However, both these values, as well as the approach of treating the factor separately

---

[1]developed by the Los Alamos Accelerator Code Group (LAACG)
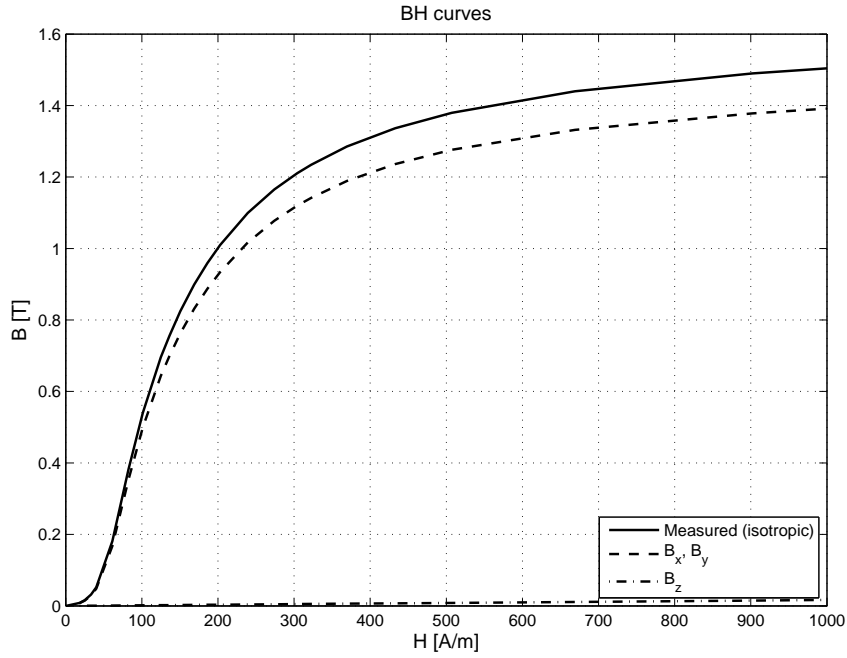
Figure 5.4: Magnetization curves of iron.

for focusing and defocusing half-units, are only an attempt of modelling 3D field effects of a real magnet in the 2D analysis. As shown in Fig. 5.3, the magnetic field is not constant along the beam trajectory in the real magnet. Air gaps, central junction and magnet end in particular have a significant influence on the field drop. It is especially visible in external blocks, where even in the middle of the block length the field can be few percents lower. Therefore estimation and numerical verification of the packing factor will be performed with respect to the reference field value.

Fig. 5.4 shows the measured isotropic magnetization curve [22] of the PS magnet steel and calculated anisotropic properties that were modified with the packing factor $\lambda = 0.9496$. Modified BH-curve in the lamination plane is noticeably lower than the measured one, which pretends the existence of laminations or also air gaps when other factor value is used.

5.2.2   Iron saturation

Magnetic properties of the PS magnet steel have a non-linear character, especially when material is highly magnetized and saturation effect occurs, limiting the magnetic flux growth with the increase of excitation current. The constitutive equation of magnetic material can be written in the form

$$\mathbf{B} = \mu_o(\mathbf{H} + \mathbf{M}), \tag{5.8}$$

where $\mathbf{M}$ is the magnetization factor that describes the movement of magnetic domains, which are regions of aligned electron spins grouped together. When all magnetic domains are aligned in the same direction the material reaches the saturation and further increase of the flux is limited to that provided with the permeability of free-space μ_0. The magnetization shown in Fig. 5.4 proceeds with the movement and rotation of magnetic domains. At first the magnetic field rises slowly in the region of reversible movements and next faster, slightly linear in the region of irreversible movements. After that, when magnetic domains are being reversibly rotated, the iron core becomes saturated and the increase of induced field is much slower.

With the element type that used in simulation and available magnetization curve, the saturation of the iron core can be modelled. If the magnetic flux locally exceeds the range of given BH data further calculations are continued by ANSYS with the permeability of free-space. It happens only in the analysis of a high excitation state of the magnet required for high energy beam guidance.

5.3 Boundary conditions and loads

Both open and closed blocks are symmetrical with respect to the horizontal median plane. Using this feature we can model only the upper half of the magnet, which will decrease number of elements in the model, but simultaneously we have to apply boundary conditions which will force perpendicularity of flux lines to the symmetry plane. On external boundaries of the air domain the flux is forced to flow parallel to the limiting edges.

The model is loaded with current densities applied to conductor areas. Current values have been taken from the control program of a real PS magnet excitation cycle, during which the beam is injected into the machine, accelerated to certain energy and then ejected. The model is used to simulate the magnet when the currents are constant and the magnetic field is stabilized. A simulation was performed under few operational conditions of the coils, that

Cycle	I_{mc}	I_{f8}	I_{pfwF}	I_{pfwD}
E	669.2 A	—	—	—
A	2677.5 A	450.35 A	39.47 A	-45.08 A
B	4732.0 A	—	77 A	88 A
C	5413.15 A	1257.9 A	200.7 A	99.75 A
LHC	5400.56 A	1452.8 A	206.7 A	86.9 A

Table 5.1: Different configurations of currents.

have been measured during past measurement campaigns. The sets of currents that were used:

- E – 3.5 GeV/c cycle,

- A – 14 GeV/c cycle for continues transfer of protons to SPS (Super Proton Synchrotron),

- B – 24 GeV/c cycle for slow ejection to East Experimental Area,

- C – 26 GeV/c cycle for ejection of protons to SPS,

- LHC – 26 GeV/c proposed as test cycle for LHC purpose.

5.4   Post-processing

The result of the electromagnetic analysis is the nodal vector potential A_z from which the nodal magnetic flux density **B** and the field intensity **H** are derived. The ANSYS general postprocessor does not have the capability of decomposing those quantities, the magnetic flux density in particular, into its multipole terms. To perform this post-processing operation the Fourier series field expansion procedure was written in APDL[2] scripting language.
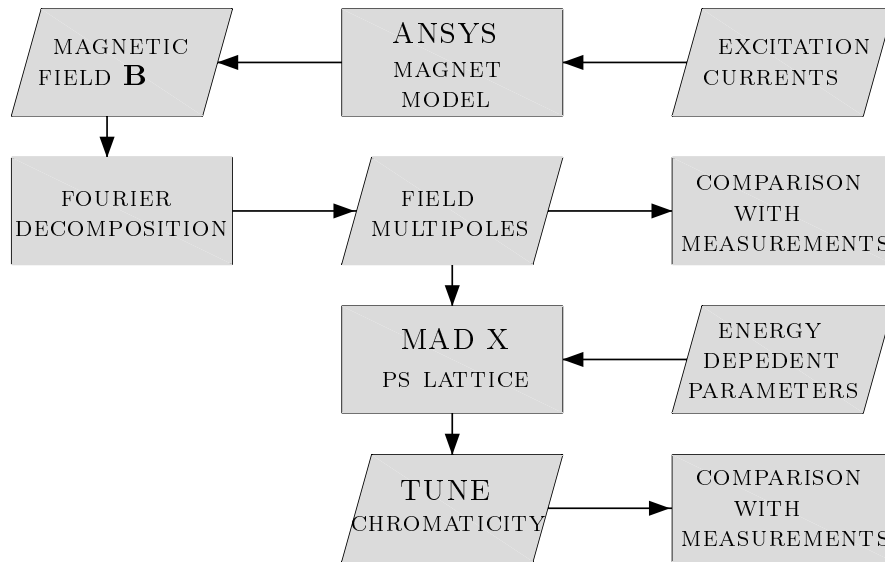

Figure 5.5: Scheme of the calculation algorithm.

---

[2]ANSYS Parametric Design Language

5.4.1 Fourier series expansion of the magnetic field

Fourier series expansion uses 2D field map in the cross-section plane of the magnet. Unlike the field gradients calculated with derivatives of the field measured on the median plane, the Fourier method calculates multipole components using multiple points on the circular path, therefore it is much more accurate.

The numerical solution has to be transformed to the B_r component calculated in N points

$$\varphi_k = \frac{2\pi k}{N}, \qquad k = 0, 1, 2, \ldots, N - 1 \tag{5.9}$$

on the circular path with reference radius of $r = r_0$. We can write the Fourier series expansion of the magnetic flux density

$$B_r(r_0, \varphi_k) = \sum_{n=0}^{\infty} \left(A_n(r_0) \cos n\varphi_k + B_n(r_0) \sin n\varphi_k \right) \tag{5.10}$$

with the Fourier coefficients

$$A_n(r_0) = \frac{2}{N} \sum_{k=0}^{N-1} B_r(r_0, \varphi_k) \cos n\varphi_k \tag{5.11}$$

$$B_n(r_0) = \frac{2}{N} \sum_{k=0}^{N-1} B_r(r_0, \varphi_k) \sin n\varphi_k \tag{5.12}$$

To obtain the multipole coefficients in the same units as measured data, they have to be defined independently of the reference radius

$$\mathcal{A}_n = A_n \frac{(n-1)!}{r_0^{n-1}}, \qquad \mathcal{B}_n = B_n \frac{(n-1)!}{r_0^{n-1}} \tag{5.13}$$

Multipole components calculated this way can be directly compared with the measurement data or used in accelerators and lattice design programs such as MAD-X [17].

5.4.2 Comparative data

The latest measurement data, which can be used for comparison, come from the measurement campaigns that took place in 1992 [11] and 2004 [2]. These campaigns have been carried out using a detector equipped with an array of the Hall probes, which measure only the field component normal to their surface. However, the measurements were performed on the symmetry plane of the magnet, where, as it follows from the Maxwell equations, the magnetic field is perpendicular to this plane.

After obtaining the map of the magnetic field, higher order components of the field, such as quadrupole and sextupole, were approximated with derivative of the dipole component in x-direction, as shown in Eqs. (5.14) and (5.15).

$$\mathbf{G}(x_i, z) = \frac{\mathbf{B}(x_{i+1}, z) - \mathbf{B}(x_{i-1}, z)}{x_{i+1} - x_{i-1}} \qquad (5.14)$$

$$\mathbf{S}(x_i, z) = \frac{\mathbf{G}(x_{i+1}, z) - \mathbf{G}(x_{i-1}, z)}{x_{i+1} - x_{i-1}} \qquad (5.15)$$

The consequence of calculating derivative this way is the measurement error transportation to those components. The total error of the measurement (that takes into account all errors like: Hall probes calibrations, eddy currents effect, probes alignment precision, temperature difference between probes, etc.) has been estimated below 0.05%. The aftermath of that is the relative error of quadrupole on the level of 3%, which still gives a good estimation of the gradient value. However, the sextupole component error reaches even some 70%, which can only give a rough information about its behaviour [2].

Chapter 6

Results of 2D analysis

In this section we will present some of the results obtained with the use of 2-dimensional PS magnet model. At first, we will consider the quality of the calculated magnetic field in terms of discretization and input parameters. Then, three specific solutions, representing real operating states of the magnet, will be compared with the data available thanks to the measurement campaigns.

6.1 Model verification

To begin with, a series of tests had to be performed in order to verify the convergence of the solution. The finite element mesh refinement and the boundary discretization were the factor taken into consideration, as well as the magnetic material properties and the packing factor, both of which have a significant influence on the solution.

In the verification section the current values from the LHC type excitation were used. It generates high level magnetic field which guarantees that the iron saturation phenomenon appears and the whole range of BH curve is used in the simulation.

6.1.1 Boundary distance influence

The simulation is performed in the limited air region with the boundary conditions that pretend the magnetic field behaviour in infinity. In order to select the appropriate boundary distance, that does not deteriorate the solution, the boundary influence was investigated. The test was carried out with the black-leg iron yoke width $d = 360$ mm as a parameter of the air region dimension as shown in Fig. 6.1. The packing factor value $\lambda = 1.0$ was assumed.

Fig. 6.2 presents the dipole, the quadrupole and the sextupole components at the beam trajectory as a function of the boundary dimension. It can be seen that although the changes are not significant, all three components converge to certain values with the increase of n. The sextupole component is characterized
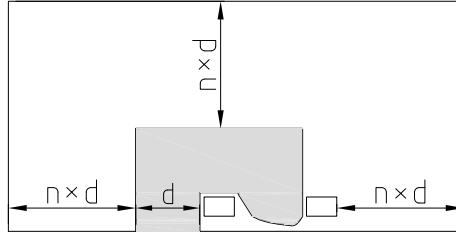
Figure 6.1: Parameterization of the boundary dimension.

by the biggest differences. Its values at $n = 1$ and 16 differ by $\delta_s^{(1-16)} = 0.07\%$, while for the dipole and the quadrupole this difference is less than 0.02%. The rate of change between the last two tested values is much lower. For the sextupolar component $\delta_s^{(8-16)} = 0.004\%$, while for two other components it is less than 0.0015%, which allows us to assume that the value $n = 8$ gives a sufficient accuracy of the solution.
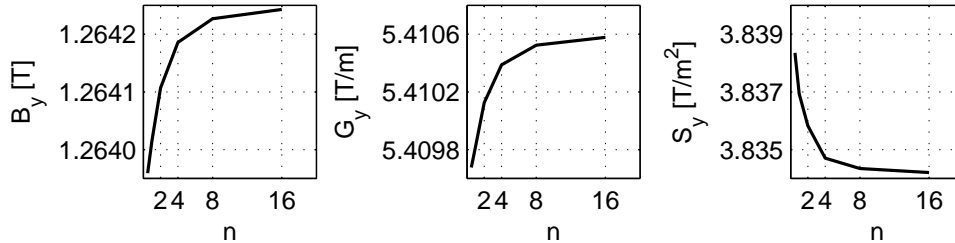
Figure 6.2: Boundary distance influence on field components at $x = 0$.

6.1.2 Solution sensitivity to the material data

In non-linear electromagnetic analysis the crucial factor is the quality of the magnetization curve, which has a strong influence on the solution convergence. Available data had been measured up to 2.03 T, but as it is shown in Figs. 6.3 and 6.4, the calculated magnetic field density and intensity of the LHC cycle both exceed the range of measured properties. When the magnetic field inside the iron yoke exceeds locally the given BH data the material is assumed to be completely saturated and further calculation in this point is proceeded with the permeability of free-space.

In Fig. 6.5 we can see that such extrapolation makes the BH-curve discontinuous in terms of $\frac{\mathrm{d}B}{\mathrm{d}H}$ at the end of original data, which seems to be an unphysical behaviour. Too early assumption that the iron is fully saturated
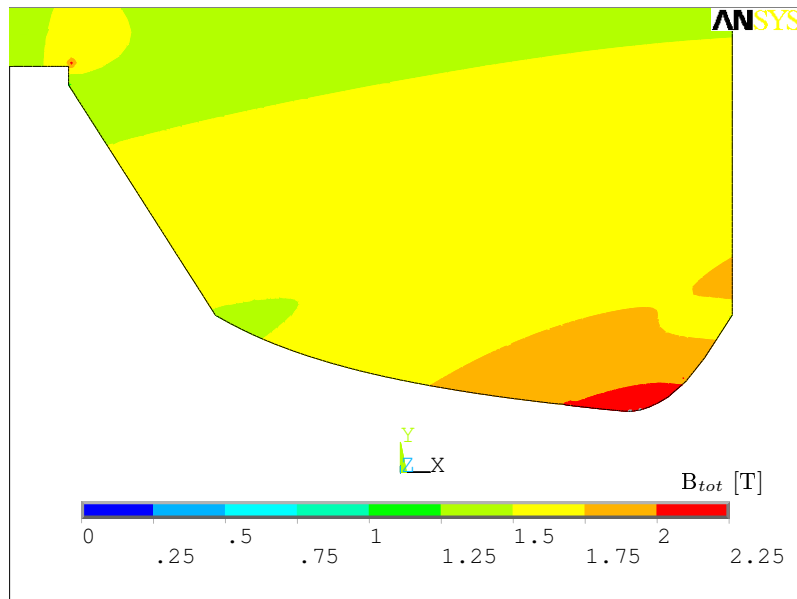
Figure 6.3: Magnetic field density of the magnet pole at 26 GeV/c. The magnet pole-tip is fully saturated.
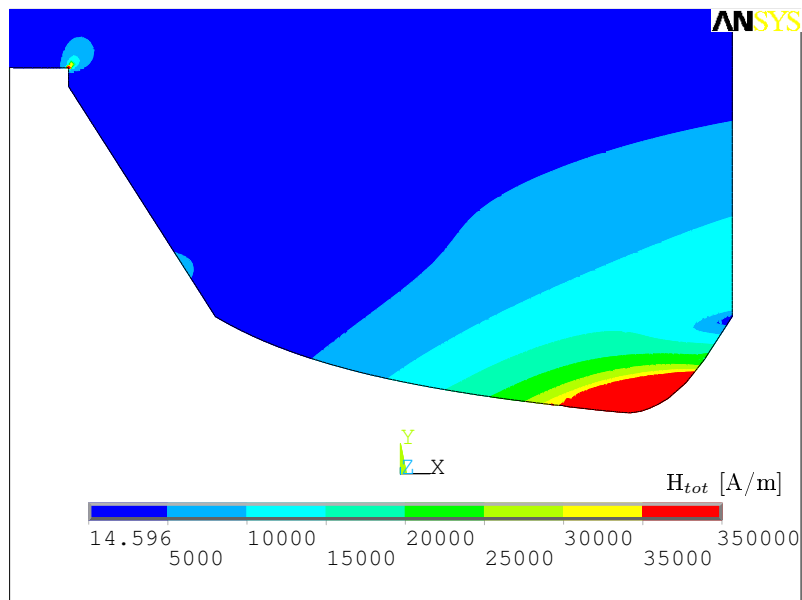

Figure 6.4: Magnetic field intensity of the magnet pole at 26 GeV/c. The magnet pole-tip is fully saturated.
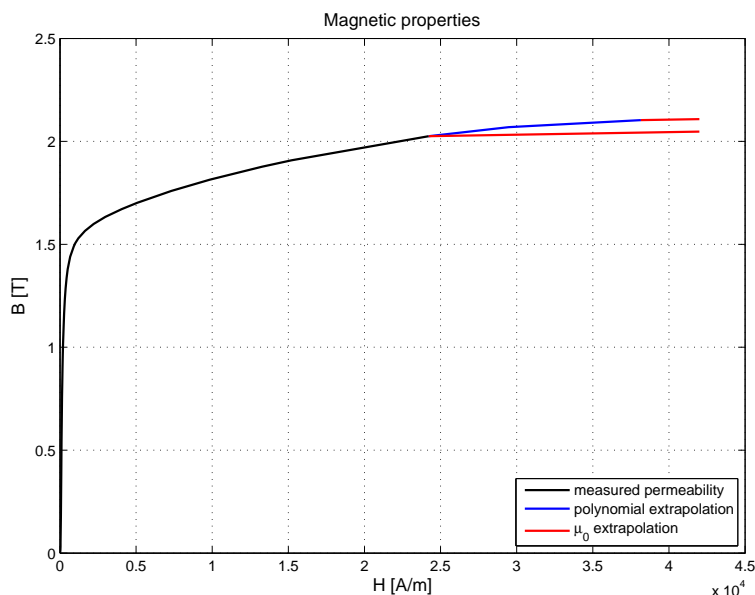
Figure 6.5: Magnetization curve used in the simulation.

might have been the reason of underestimation of the magnetic field in the narrowest part of the pole gap that has reached 1.5% with respect to the measured value for the LHC cycle.

In order to complete the missing data the curve has been extrapolated by means of the 2nd order polynomial in the range where $\Delta B / \Delta H \geq \mu_0$. The obtained points are only an estimation and should be verified by more detailed measurements. However, the aforementioned error in the highly satu-rated region has been reduced to 0.8%, which allows to believe that the applied approximation of missing data is to some extent correct.

The next crucial element of the material data verification is the packing factor. As it was stated in Section 5.2.1, this parameter is extremely important since it introduces laminations and air gaps effect to the 2D model, but its theoretical estimation based on magnet geometry is inaccurate.

To evaluate the sensitivity of the model to this factor and estimate its value for the use in further analysis, a series of calculations were performed. The influence of the factor was tested in the range $0.919 \leq \lambda \leq 0.931$ as shown in Fig. 6.6. It shows that the choice of $\lambda = 0.925$ in the past calculation was quite right since the dipole component error in both half-units is very low and on the same level, while the quadrupole error has almost the same value but opposite sign. The extrapolated zero level of the dipole error lies outside the range of theoretical packing factor values which results from the magnet geometry. The use of this packing factor value brings satisfactory results and will be applied in further analysis.
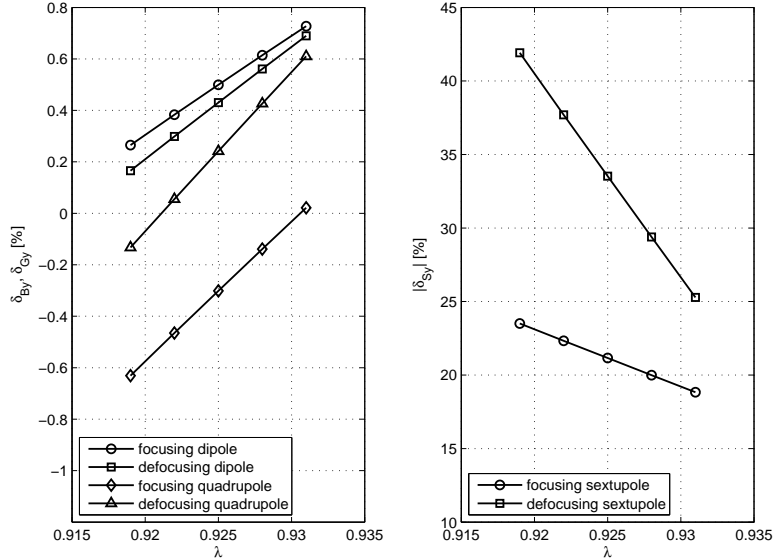
Figure 6.6: Solution sensitivity to the packing factor.

However, the focusing sector is shorter than the defocusing because air gaps between its blocks are 7.75 mm while in the other sector the gaps have length 9.75 mm. Thus, the magnetic/non-magnetic material ratio is smaller in the defocusing sector so the packing factors should satisfy the condition $\lambda_D < \lambda_F$. This is confirmed by the quadrupolar component errors, which are zero for the following factor values

$$
\begin{aligned}
\lambda_F &\approx 0.9306, \\
\lambda_D &\approx 0.9211,
\end{aligned}
\tag{6.1}
$$

but at the same time it makes dipole errors difference more significant. Nevertheless, this approach as well as the previous one with a single packing factor have to be taken under consideration.

6.1.3 Verification by using the ROXIE model

The correctness of results may be verified with the solution obtained by other methods. For this purpose the ROXIE[1] program package was chosen. It has been developed in CERN mainly for the design and optimization of the LHC superconducting magnets [3][25], however, it may be successfully used for calculations of warm magnets as well. It uses a reduced vector potential formula-

---

[1] **R**outine for the **O**ptimization of magnet **X**-sections, **I**nverse field calculation and coil **E**nd design
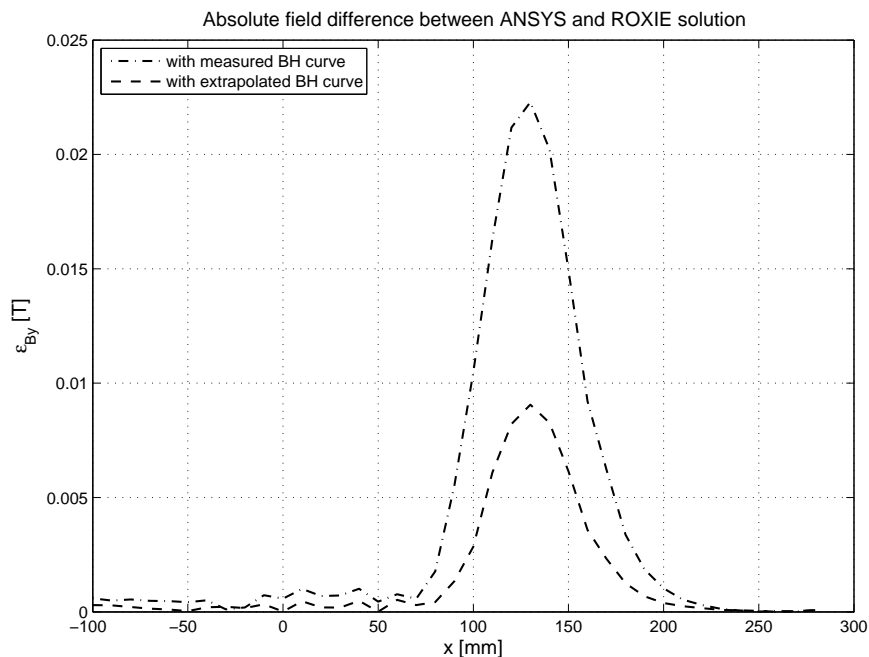
Figure 6.7: Absolute field difference between ANSYS and ROXIE solution of the LHC cycle. Zero corresponds to the beam trajectory.

tion[2] and the BEM-FEM coupling method[3], which does not need the surrounding air region to be discretized as a finite domain with finite elements. Thus there are no artificial boundary conditions on the far field boundaries [25]. This feature is extremely useful in the field calculations of coil ends and optimization of superconducting coils, while in our case it will provide a useful benchmark to the research presented in Section 6.1.2.

Both models were built to have exactly the same geometry of focusing half-unit. Air region boundaries in the ANSYS model were placed at the distance that corresponds to the parameter $n = 16$, with respect to the magnet elements. Two sets of material data were used in the simulation: the original measured BH-curve and the extrapolated one, both with no lamination stacking effect ($\lambda = 1$). ROXIE behaves in the same manner as ANSYS when magnetic field of the iron exceeds the given material data. In this case the calculation is proceeded with the permeability of the free-space.

Fig. 6.7 shows the field differences of both models on the magnet median plane. Discrepancies can be seen in the range of 75 mm $< x <$ 200 mm (see Fig. 4.4 for the pole geometry), where saturated pole-tips are located. When the measured BH-curve was used the maximum relative error corresponds to

---

[2]developed at IGTE Graz, Austria

[3]developed at ITE Stuttgart and Robert Bosch GmbH, Germany

$\delta_{MAX} = 1.29\%$. However, in simulation with the extrapolated material data the error has been reduced to 0.52%, which is satisfactory for the region of high saturation. Outside this region the results coincide, which is show in Table 6.1.

Multipole	ANSYS	ROXIE	relative error δ
dipole [T]	1.26424	1.26426	0.001%
quadrupole [T/m]	5.41058	5.40944	0.021%
sextupole [T/m^2]	3.83421	3.77767	1.475%

Table 6.1: Comparison of field components obtained using ANSYS and ROXIE on the beam trajectory of the focusing half-unit.

6.2   Low energy cycle

The beam momentum during cycle E reaches the level of 3.5 GeV/c, hence the magnetic field, which is needed to keep circulating particles on a constant radius, is also low. In both types of blocks the dipole component obtained in the simulation is equal 0.1665 T on the beam trajectory, and the quadrupolar field reaches 0.6839 T/m for focusing and -0.6852 T for defocusing gradients. At this level of magnetic field the saturation of the steel does not occur and the shape of the multipole components is determined by the pole profile. Therefore, the correction of multipoles introduced by the auxiliary coils is not needed and only the main coil is powered.

Comparison between the numerical solution and the measurements shows very good agreement of multipole values, however, it has to be noted that experimental data of cycles E and A comes from the paper report [11] and a data handling error was taken into account in experimental error bars. The dipole component is the most accurate in the area of the greatest interest, which is the neighbourhood of the beam. On the 10 cm long segment around the beam orbit the difference between the measured and the calculated field is less than 0.25%. Outside the region of hyperbolic pole profile the field behaves strongly nonlinearly and the error reaches the level of 1.6%.

The behaviour of the quadrupole component that is derived from the dipole field shows that the linear field has been achieved with the hyperbolic poles without use of any auxiliary windings. In this region the difference compared to the measurement is oscillating between 0.4% and 1.2%. The error of the quadrupole component increases suddenly in the narrowest point of pole aperture where field gradient changes dramatically. It can be seen that the biggest discrepancies for both dipole and quadrupole components are located in the

Figure 6.8: Comparison between the calculated and the measured cycle E dipole component.

Figure 6.9: Absolute error of cycle E dipole component.

Figure 6.10: Comparison between the calculated and the measured cycle E quadrupolar component.

Figure 6.11: Absolute error of cycle E quadrupolar component.
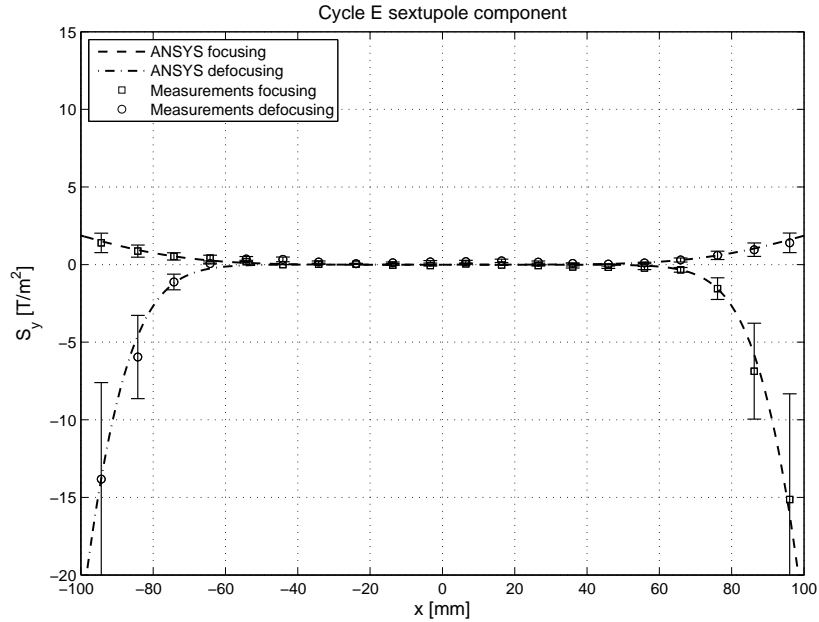
Figure 6.12: Comparison between the calculated and the measured cycle E sextupolar component.

same region outside the hyperbolic part of the pole, where the field is strongly nonlinear and reaches the highest level.

In comparison of sextupolar components the measurement error has to be taken into account. A detailed discussion on quantitative error has been passed over due to the fact that sextupolar components at this level of magnetization is very small and difficult to measure. An error on the measurements up to a factor of 2 can be assumed [11]. However, computed solution has converged with measured data on both the flat and external parts of the component, which is presented in Fig. 6.12.

6.3   Medium energy cycle

Cycle A is an excitation program of which the final ejection momentum of 14 GeV/c is in mid-range of PS capability. The magnetic field at equilibrium orbit reaches 0.6534 T in focusing half-unit and 0.6840 T in defocusing, while the calculated quadrupole field reaches 2.7498 T/m and -2.7406 T/m respectively. The difference of 0.0306 T in the dipole field value is caused by the figure-of-eight loop. Current in focusing half of this winding floats in the opposite direction to the current in the main coil causing a decrease of the field while in defocusing half currents have the same direction and the field is increased. In
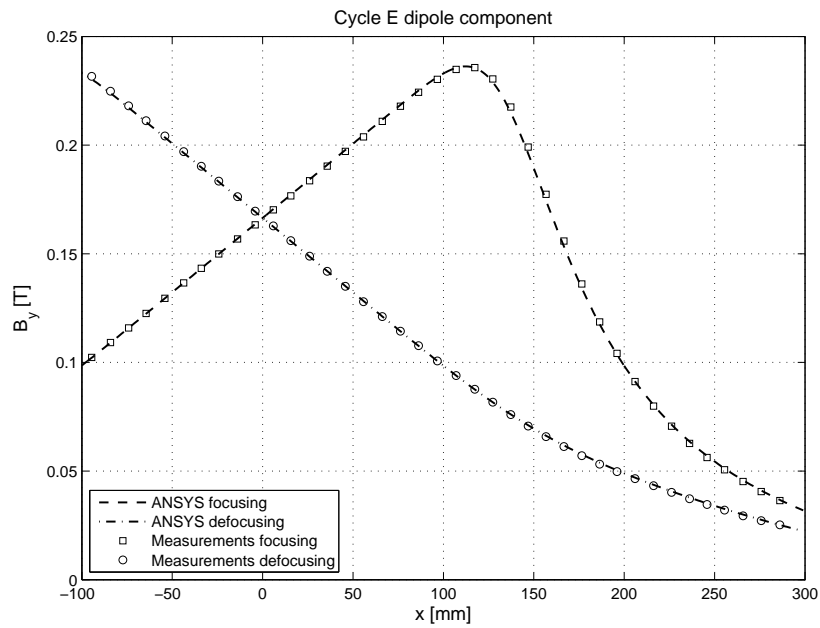
Figure 6.13: Comparison between the calculated and the measured cycle A dipole component.
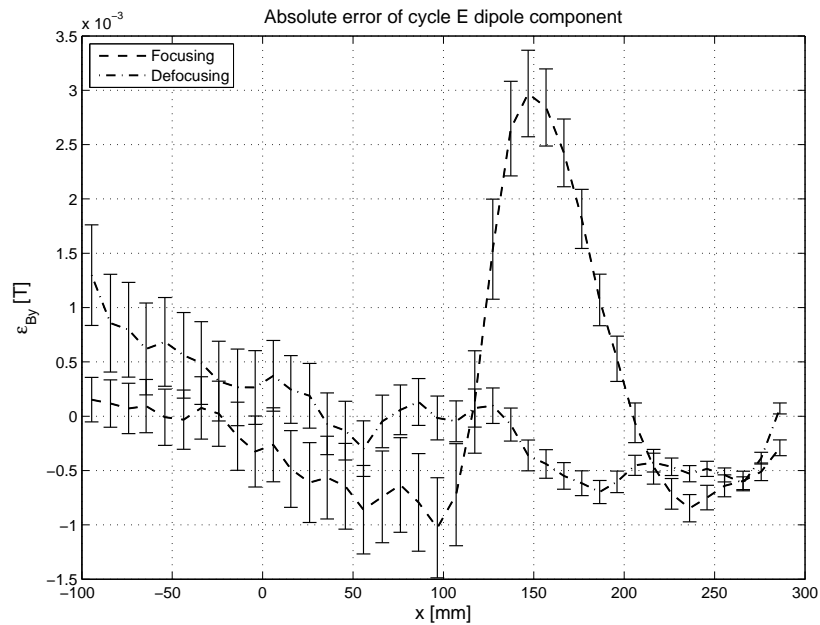

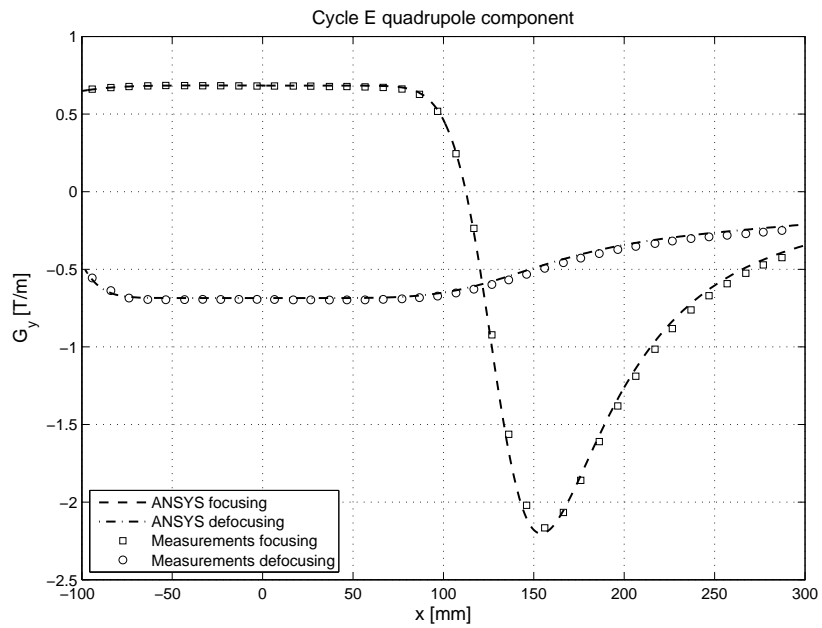Figure 6.14: Absolute error of cycle A dipole component.

Figure 6.15: Comparison between the calculated and the measured cycle A quadrupolar component.
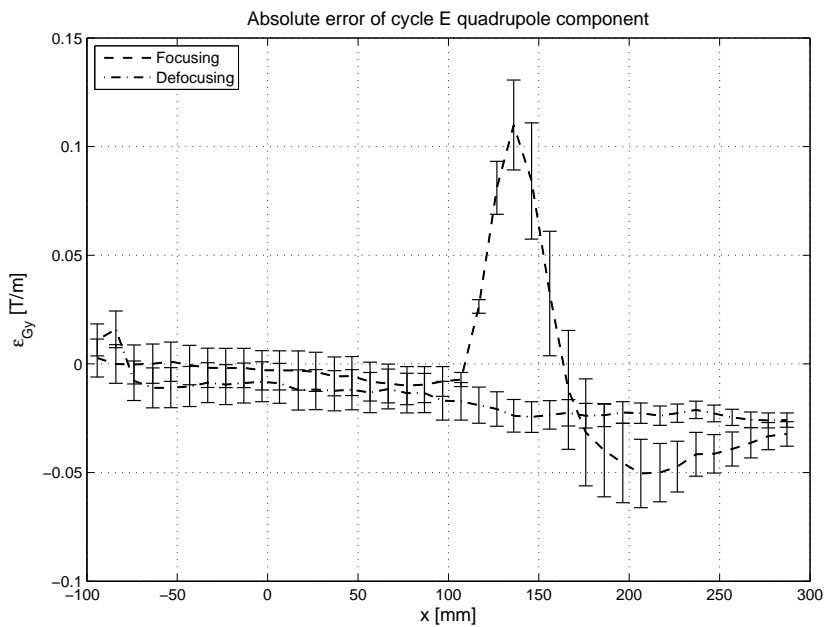

Figure 6.16: Absolute error of cycle A quadrupolar component.

Figure 6.17: Comparison between the calculated and the measured cycle A sextupolar component.

this cycle both figure-of-eight loop and pole-face windings are active to control higher harmonics of the field.

The behaviour of both dipole and quadrupole components of the field is very similar to cycle E. Discrepancies of the dipole component in the beam surrounding were less than 0.5% and less than 1.0% for the quadrupolar component with increasing trend in the narrow part of the pole.

The calculated sextupolar component corresponds to the measurements. As it can be seen in Fig. 6.17, it fits well within the experimental error bars.

6.4   High energy cycle

In the LHC cycle the particle beam is accelerated to the momentum of 26 GeV/c, which is close to the highest possible obtained in the PS. Such a particle momentum implies high magnetic field on the beam orbit at the level of 1.2356 T and 1.2938 T in focusing and defocusing halves respectively. Again, the difference between the focusing and defocusing fields is observed due to the figure-of-eight loop and it amounts to 0.0582 T. Control of the field in this cycle is also made using the pole-face-windings. The quadrupole field on the equilibrium orbit in focusing half-unit is calculated to 5.2281 T/m and -5.2332 T/m in defocusing.

The difference between calculated and measured dipole field [2] is less than 0.5% in the beam region and reaches 0.7% in the narrowing of the pole aperture. Discrepancies of the quadrupolar component on the beam trajectory are less than 0.3%.

The measurement data of the LHC cycle sextupolar component [10] are available in much wider region than for the other two presented cycles. Fig. 6.22 shows that the simulation has well reproduced the behaviour of the sextupolar component. However, in highly nonlinear parts of the field discrepancies are clearly visible, which can be seen closely in Fig. 6.23.

Multipole	Focusing			Defocusing		
	Meas.	Ansys	δ [%]	Meas.	Ansys	δ [%]
B_y [T]	1.2295	1.2356	0.50%	1.2882	1.2938	0.43%
G_y [T/m]	5.2440	5.2281	0.30%	-5.2212	-5.2332	0.23%
S_y [T/m^2]	3.5843	2.8132	21.5%	-1.1155	-1.4257	27.8%

Table 6.2: ANSYS results compared with the measurement of unit type U. Field components were calculated and measured on beam trajectory at 26 GeV/c.

Multipole	Focusing			Defocusing		
	Meas.	Ansys	δ [%]	Meas.	Ansys	δ [%]
B_y [T]	1.2304	1.2365	0.50%	1.2876	1.2948	0.56%
G_y [T/m]	5.2171	5.2348	0.34%	-5.2548	-5.2464	0.16%
S_y [T/m^2]	3.1818	2.7492	13.59%	-1.1655	-1.3991	20.04%

Table 6.3: ANSYS results compared with the measurement of simulated unit type R. Field components were calculated and measured on beam trajectory at 26 GeV/c.
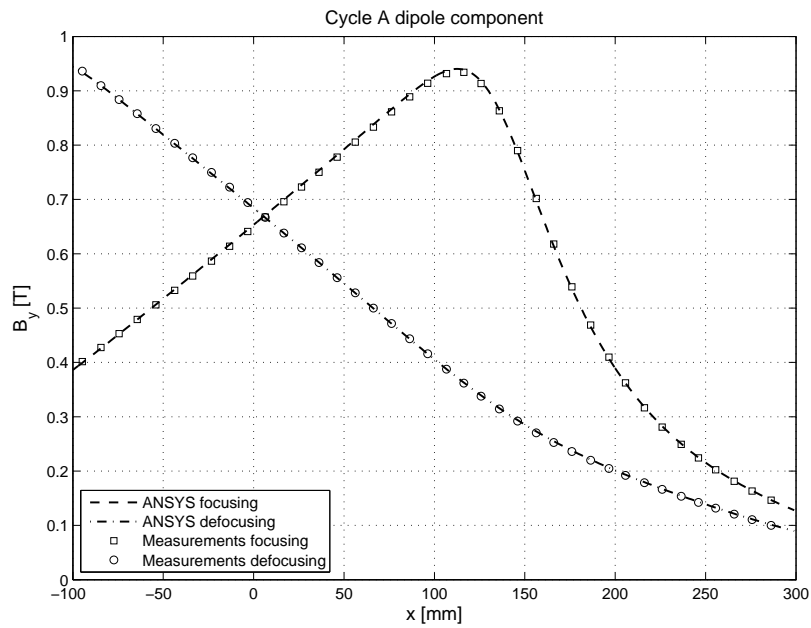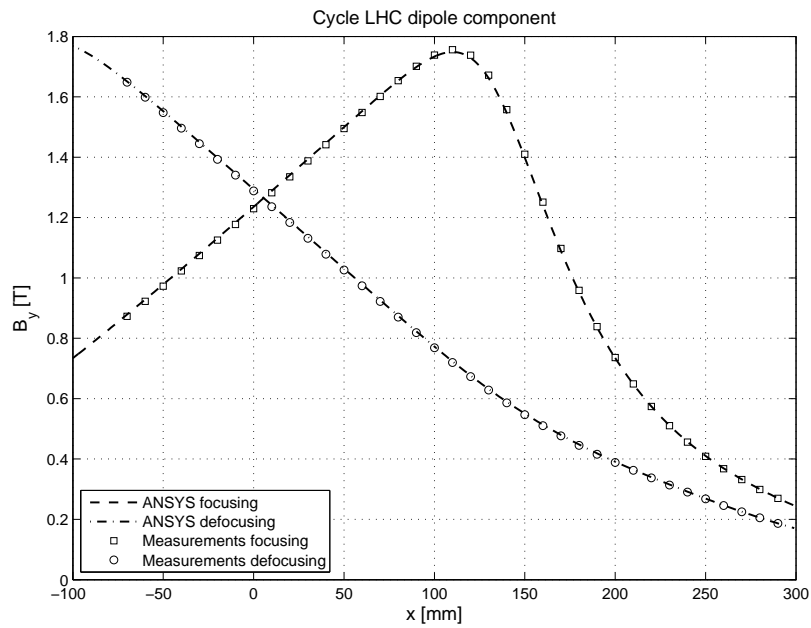
Figure 6.18: Comparison between the calculated and the measured cycle LHC dipole component.
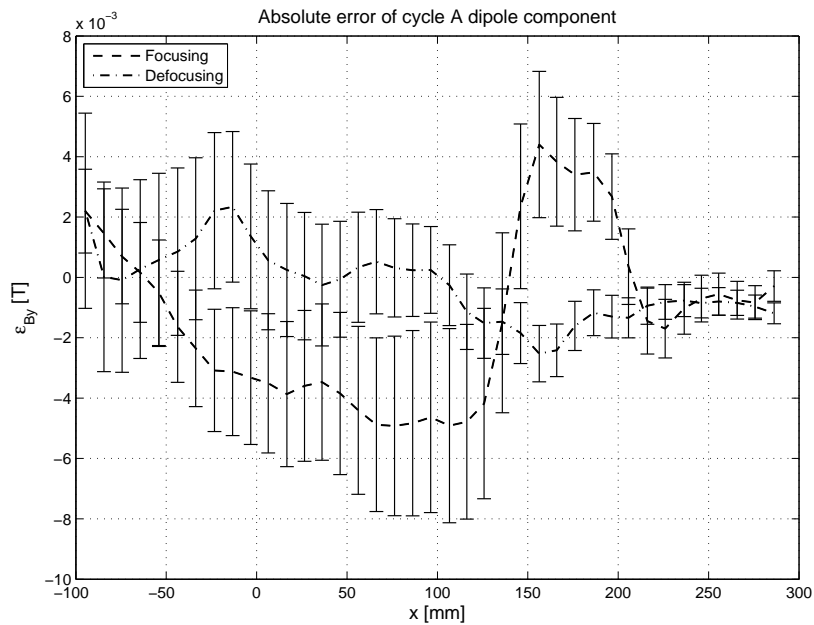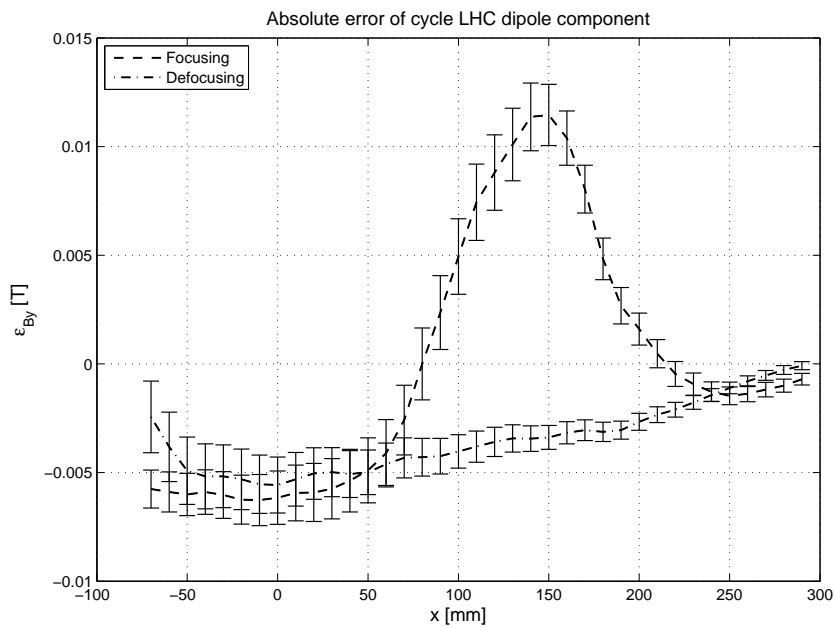

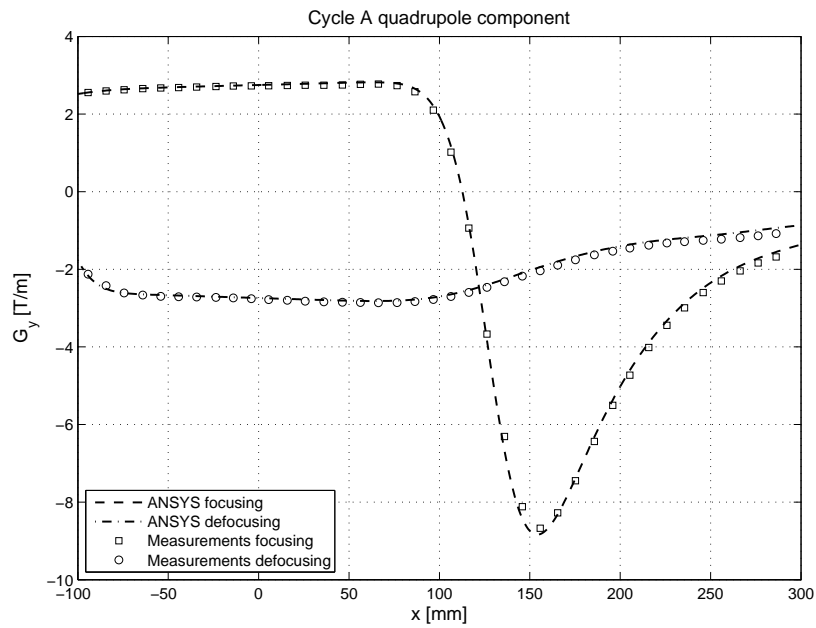Figure 6.19: Absolute error of cycle LHC dipole component.
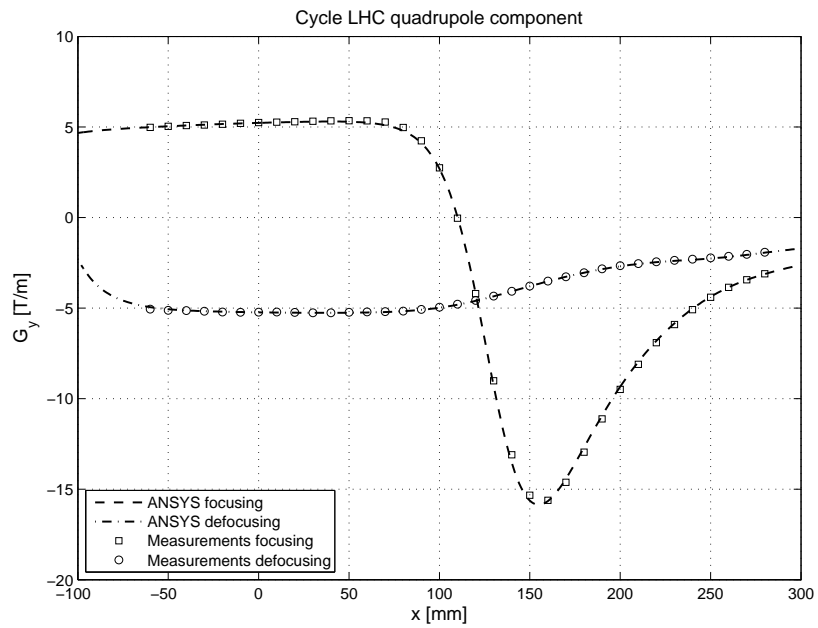
Figure 6.20: Comparison between the calculated and the measured cycle LHC quadrupolar component.
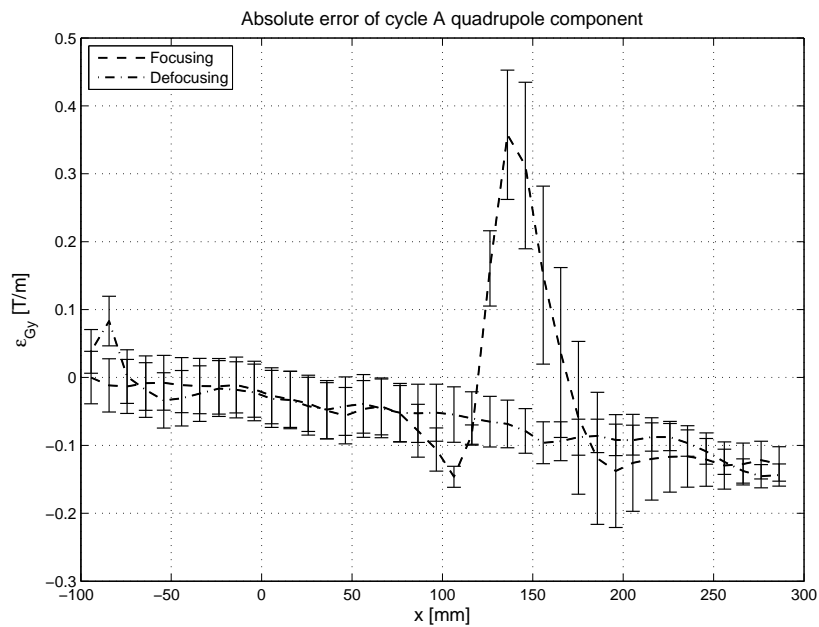

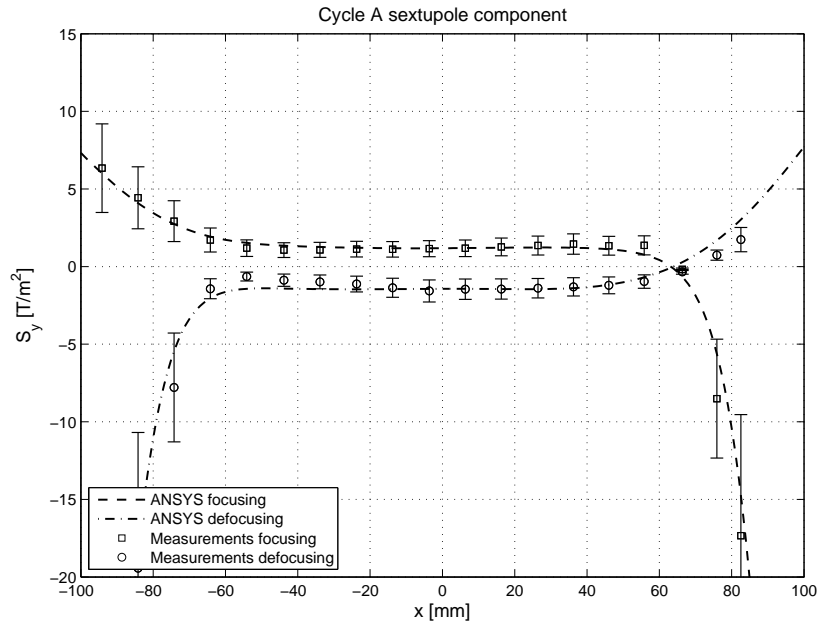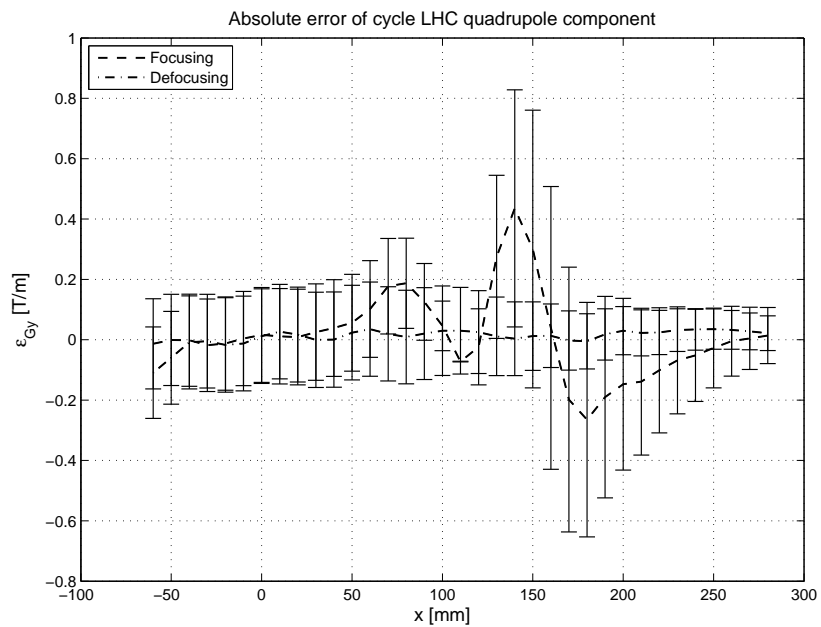Figure 6.21: Absolute error of cycle LHC quadrupolar component.
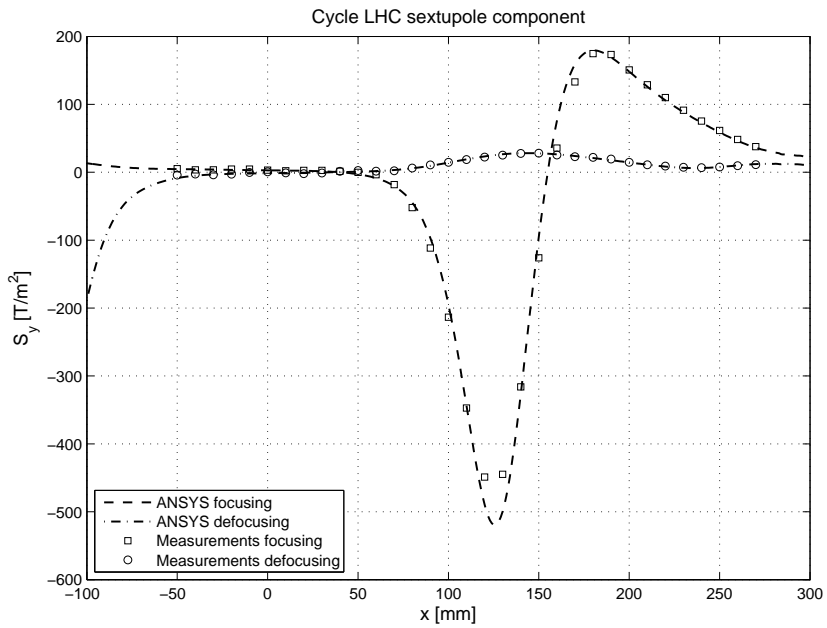
Figure 6.22: Comparison between the calculated and the measured cycle LHC sextupolar component.
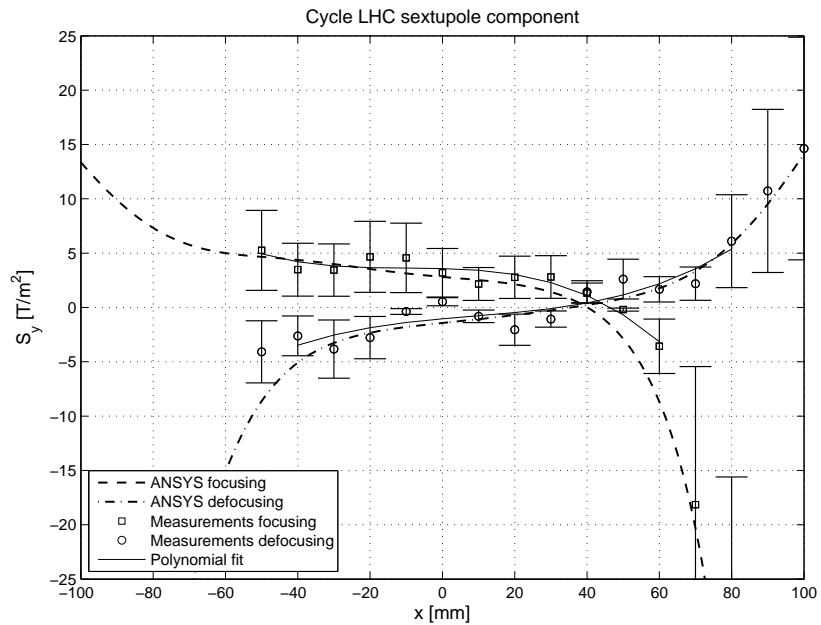
Figure 6.23: Comparison between the calculated and the measured cycle LHC sextupolar component in the pole gap.

Chapter 7

3D magnetic field map calculation

Magnetic field generated by the PS magnet is not uniformly distributed along the magnet half-units. Both ends of the magnet are sectors where the field decreases gradually. Furthermore, air gaps, both the central junction and the gaps between the blocks of the same type, have also the influence on the magnetic field. These effects cannot be modelled in the 2D analysis, thus an attempt was taken to create a 3D model of the magnet.

The solution is verified with the data from the latest measurement campaign, that was undertaken in 2004 [2]. The measurement was performed using a matrix of Hall probes and covered the median plane of the magnet including the ends of the magnet as well as the field in the junction area.
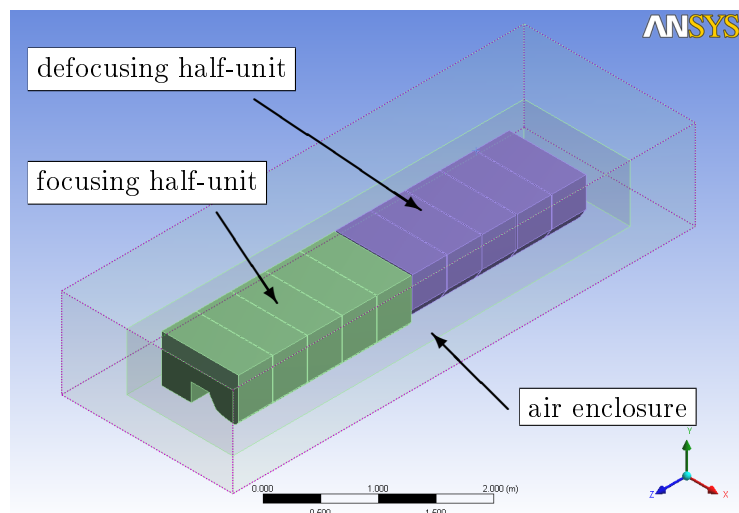
Figure 7.1: 3D model of the PS magnet without coils.

7.1   Full magnet model

The first attempt was to create a 3D model that would contain all 10 blocks and all exciting coils. For the simplicity of the coils modelling, blocks were aligned into a straight line, even though the real magnet is bent with a bending radius of 70.0789 m. The blocks and air enclosure region were meshed with the finite element SOLID117 [1], which is a 3D magnetic element that has a capability of modelling materials with non-linear magnetic properties.

7.2   Coils

ANSYS allows usage of solid conductor bodies only when the termination point of the conductor lies on a symmetry plane, while the full magnet model is symmetrical only with respect to the horizontal median plane. For this reason all coils had to be modelled as line conductor bodies and meshed with the SOURCE36 elements. In this approach, the conductor domain is not physically in the meshed model, but it is used to calculate a source magnetic field intensity $\mathbf{H}_s$ with the Biot-Savart law, which is then prescribed as a load to appropriate elements of the air domain. The advantage of line conductor bodies is the ease of modelling complex coils such as the figure-of-eight loop and the pole-face windings, but the model of these coils were simplified nevertheless. Pole-face windings are wound in the way that copper conductor loops are parallel one to another and are bent at external parts of half-units with the curvature radius of 15 mm. The bent parts were very problematic and due to their small dimensions, they were neglected in the modelling.
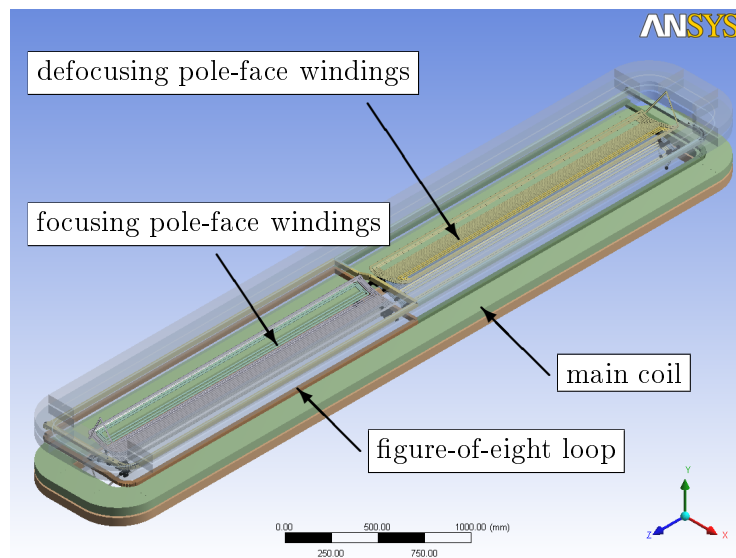
Figure 7.2: 3D model of the PS magnet coils.
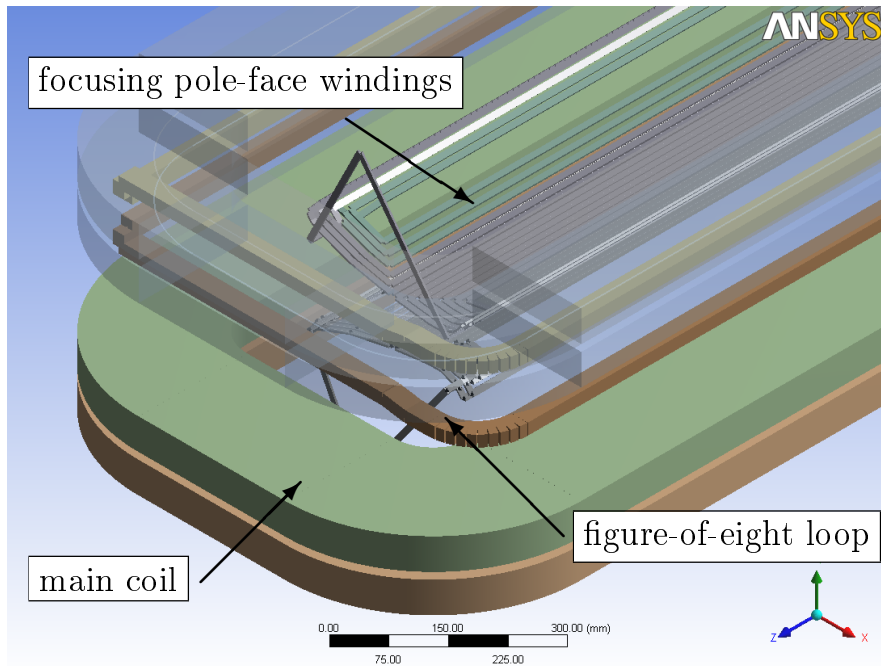
Figure 7.3: The close-up of the focusing side of coils end.

7.3 Analysis conditions

The iron as well as the air domain takes advantage of model symmetry, while the line conductor bodies do not and have to be completely modelled. On the symmetry plane the natural Flux Normal boundary condition automatically occurs. On the rest of external model faces the Flux Parallel boundary condition is applied. Coils are excited with the LHC type currents set, which allows to verify the solution at high magnetic field level, on which the saturation of iron occurs. Blocks are assumed to have non-linear isotropic magnetic material properties. The analysis is performed with two materials defined with different packing factor: $\lambda = 0.925$ that was previously used in the 2D analysis and $\lambda = 0.9496$ that is calculated for a single block with 264 lamination layers.

7.4 Finite element discretization

The final finite element model has dimensions $2.1 \times 1.1 \times 5.67$ m, which are greater than distances between the blocks or coils cross-section dimensions. The existence of such small components requires the usage of adequately small finite elements to obtain accurate solution. However, the refinement of the finite element mesh entails greater need for computer resources, which is, so far, a limiting factor. With the available resources[1], we were able to obtain a solu-

---

[1]Intel® Xeon® 5130 2.0Ghz, 8GB of RAM

tion for the model containing around 1.5×10^6 elements, but it did not allow to go below 1 cm elements on the median plane. Therefore, several additional models were built with the local mesh refinement of the beam trajectory neighbourhood. In these models, a finer mesh was used in specific magnet regions (central junction, half-units mid-blocks or external blocks), while the rest of the model was meshed with coarser elements. This allowed to obtain more detailed solution in these regions.

7.5 The results

The motion of particles takes place along the trajectory that cuts across the horizontal median plane between the magnet poles and goes through the alternating gradient field. Calculated absolute value of the B_y component of the field in this region and the beam path are shown in Fig. 7.4. The dipole and the quadrupole fields along the beam trajectory are presented in Figs. 7.5 and 7.6, respectively.

It can be seen that effects of air gaps and magnet ends are clearly visible. The field drops between each pair of blocks of the same type and lowers towards external blocks. However, the overall accuracy of the solution with respect to the measured data needs to be discussed. A relative field error on the beam trajectory $\Delta B = |B_c - B_s|$ between the calculated magnetic flux B_c and its smoothed value B_s, which was obtained with local regression using weighted linear least squares method (for more details see [19]), defines a nor-
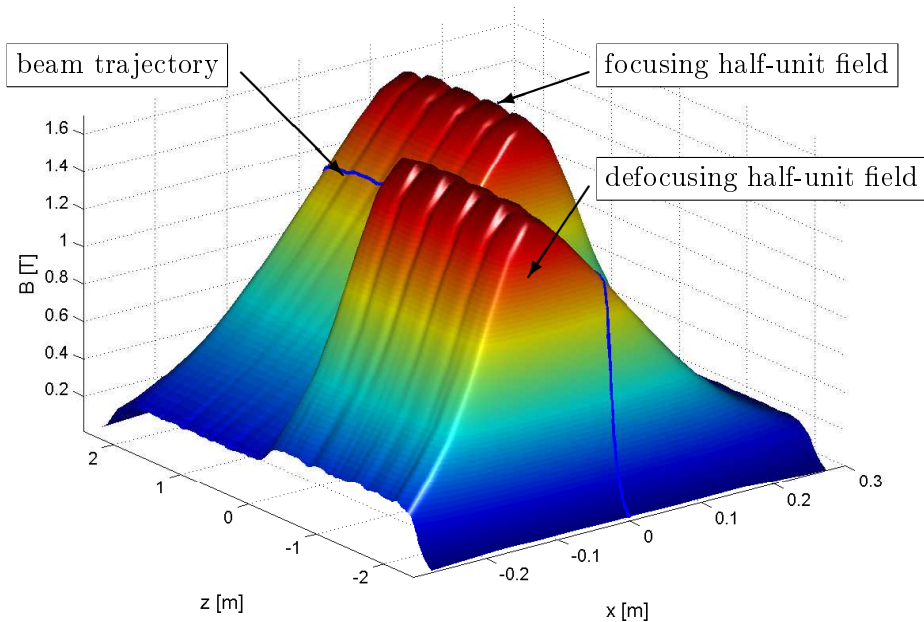
Figure 7.4: Calculated magnetic field on the horizontal median plane.
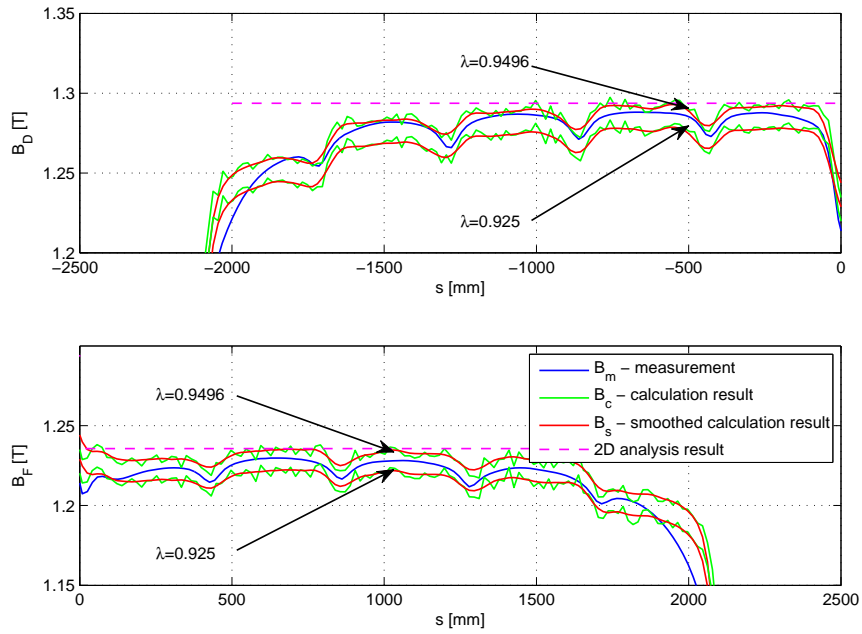
Figure 7.5: Dipole field along the beam trajectory.
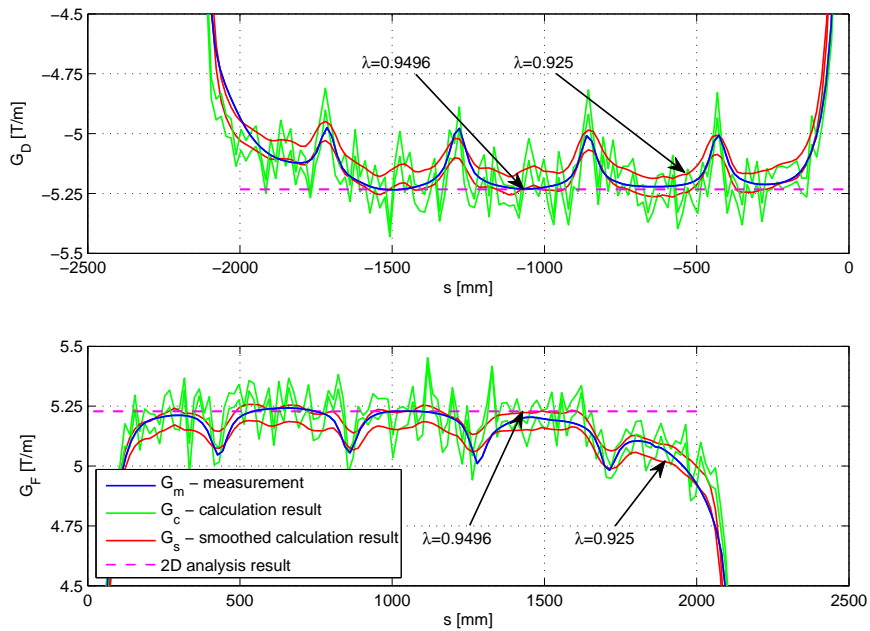
Figure 7.6: Quadrupole field along the beam trajectory.

Field integral	Measurement	$\lambda = 0.925$		$\lambda = 0.9496$	
		Ansys	δ [%]	Ansys	δ [%]
$\int B_F \mathrm{d}s$ [Tm]	2.6455	2.6461	0.02%	2.6754	-1.13%
$\int B_D \mathrm{d}s$ [Tm]	2.7840	2.7671	0.66%	2.7993	-0.55%
$\int G_F \mathrm{d}s$ [T]	10.8749	10.7459	1.19%	10.9002	-0.23%
$\int G_D \mathrm{d}s$ [T]	-10.8711	-10.7623	1.00%	-10.9344	-0.58%

Table 7.1: Field integrals along the beam trajectory and the relative difference δ between the measured and the calculated field integral values.

malized relative error $\delta_B = \Delta B / B_c^{max}$. The maximum normalized error along the steady field region amounts to 0.5%, while at junction and magnet ends 0.9% and 3.5%, respectively. These errors are transported to the quadrupole field that is derived from the dipole field as in Eq. (5.14). Thus, the quadrupole calculation errors are much higher: 4.1% on the steady field region, 13.7% at junction and 9.6% at magnet ends. Calculation errors have influence to much larger extent on sextupole as well as other higher order multipoles.

Figs. 7.5 and 7.6 present results of analysis for two different packing factors. The first factor $\lambda = 0.925$, which was previously used in 2D analysis, alters magnetic properties of the iron, which results in a slight underestimation of the field. The second factor $\lambda = 0.9496$, which is calculated for a single iron block with 264 laminations, gives results closer to the actual field. For both of these materials integrated field values were calculated along the beam path in both half-units. Comparison with the measured values presented in Table 7.1 shows that the second material gives better results, which is much more clear for quadrupolar components. Dipole component values are burdened with small discrepancies in the field of external blocks as well as those close to the junction, which makes the difference comparison less reliable.

The improvement of results quality was obtained by means of locally refined finite element model. Figs. 7.7–7.9 show the dipole, the quadrupole and the sextupole fields calculated with the model refined around the poles of focusing half-unit mid-block. From evaluation of the maximum normalized errors that have decreased to 0.26% for the dipole and 1.73% for the quadrupole component we can see that both of these quantities are more accurate compared to the previous results.

The verification of solution is also performed in the transverse plane of the magnet. It is presented in Figs. 7.10–7.12, in which the median plane field of both focusing and defocusing mid-blocks for $s = \pm 1076$ mm is shown. The model has well reproduced the actual dipole field (Fig. 7.10), especially in the beam surroundings where the difference between the solution and the measurement data is less than 0.4%. However, similarly as in 2D analysis, the calculated magnetic field between the highly saturated magnet poles is slightly
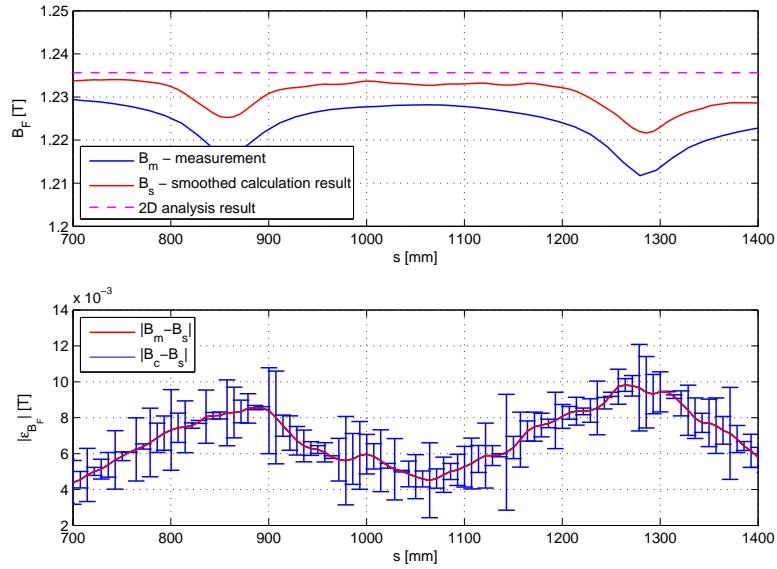
Figure 7.7: Measured and calculated dipole components (top plot) and the total error between them (bottom plot) on the beam trajectory of the focusing half-unit mid-block.
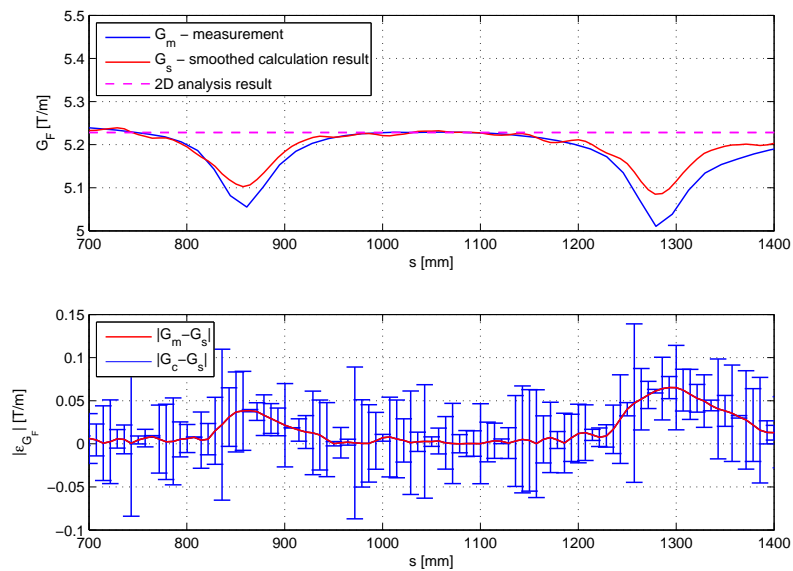
Figure 7.8: Measured and calculated quadrupole components (top plot) and the total error between them (bottom plot) on the beam trajectory of the focusing half-unit mid-block.
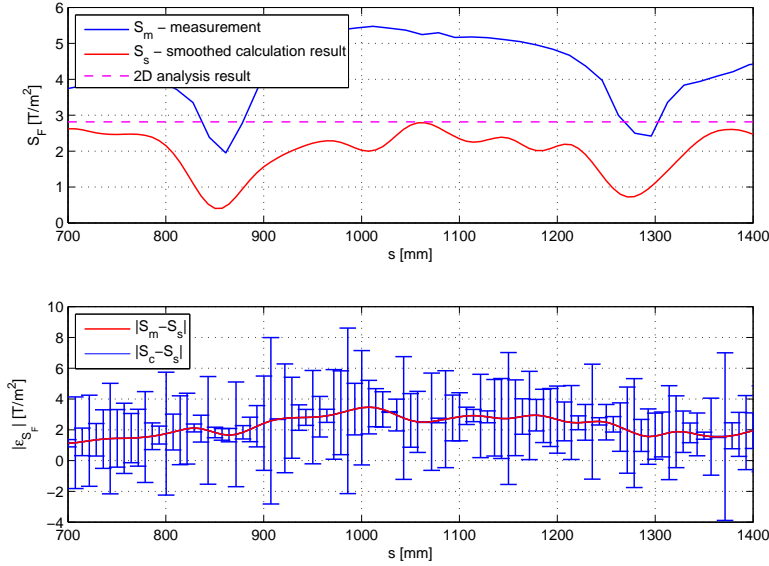
Figure 7.9: Measured and calculated sextupole components (top plot) and the total error between them (bottom plot) on the beam trajectory of the focusing half-unit mid-block.

underestimated by approximately 2% when compared to the measurements. The discrepancy in the same region is also visible in the quadrupole component (Fig. 7.11), but the difference at the beam trajectory in both blocks is much lower and does not exceed the value of 0.2%. The sextupole component (Fig. 7.12), which is derived from the solution obtained with 0.5 mm elements, is still not reliable. The shape of this component and its accuracy is very similar to the measured values, but it is far from the quality of 2D solution. The applied mesh refinement is still sufficient neither to obtain accurate sextupole nor higher order multipoles, but further improvement of quality is only a matter of computer capacity.

Separate models were also create for the junction and magnet ends refinement. The solution of both of them, presented in Figs. 7.14 and 7.15, has improved as in the prior case. It can be seen that the shape of the field obtained with 3D model is very similar to the actual field and even the interaction of alternating gradients field in the magnet centre is visible. However, there are higher discrepancies between the solution and the measured field in the external parts of both half-units. This was expected since these are the regions were conductors have complex shape that was to some extent simplified. These discrepancies are higher than those in the stable field region and amount to 1.5% at the first focusing block (for $s = 60$ mm) and 2.9% at the last focusing block (for $s = 2000$ mm).
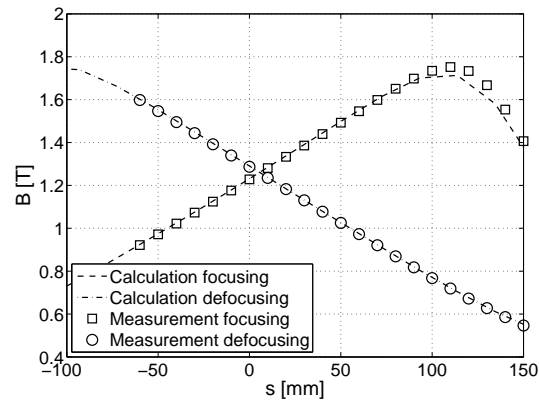
Figure 7.10: Dipole field at $s = \pm 1076$ mm.
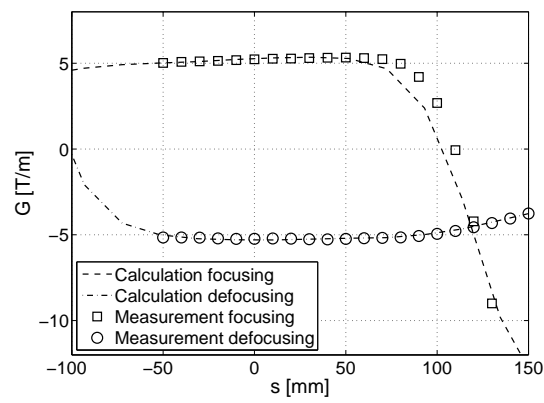
Figure 7.11: Quadrupole field at $s = \pm 1076$ mm.
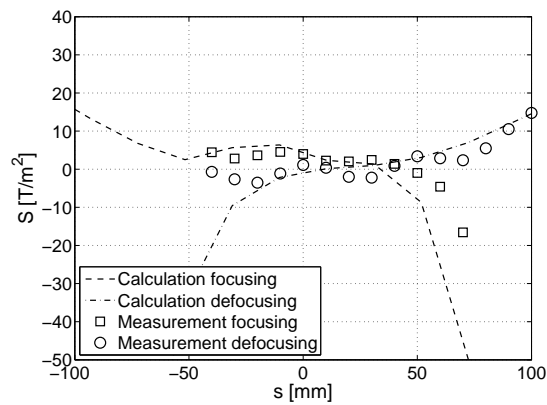
Figure 7.12: Sextupole field at $s = \pm 1076$ mm.
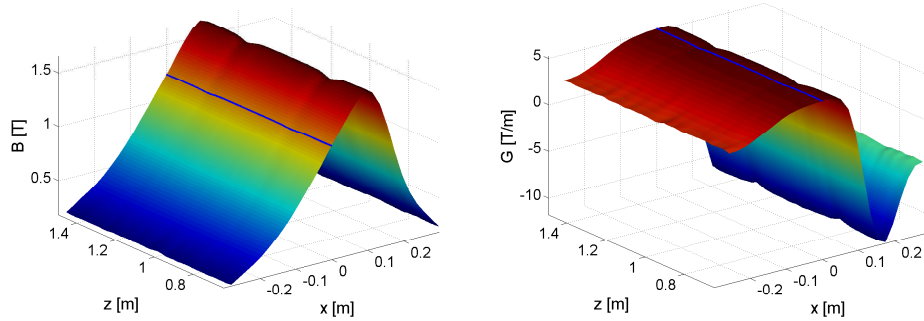
Figure 7.13: Dipole (left) and quadrupole (right) fields on the median plane of the focusing half-unit mid-block.
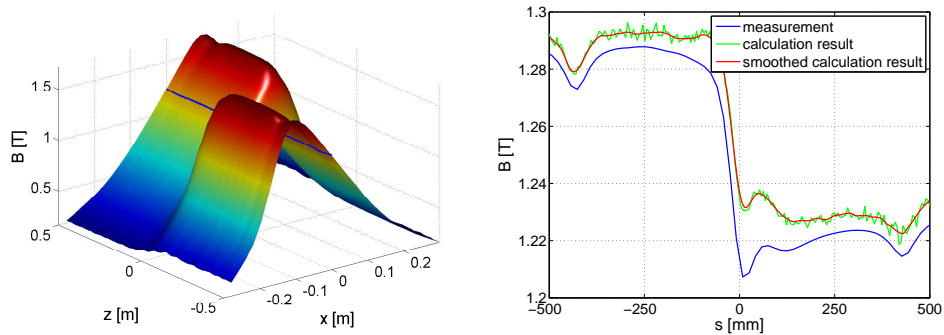
Figure 7.14: Dipole field at the median plane (left) and along the trajectory (right) in the junction region.
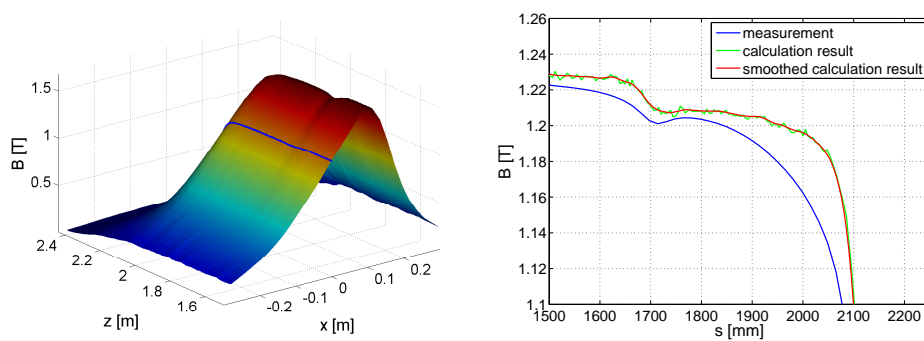
Figure 7.15: Focusing dipole end-field at the median plane (left) and along the trajectory (right).

Chapter 8

Application of the numerical solution in MAD

The magnetic field calculated with ANSYS model and decomposed into multipole terms can be applied in MAD[1] program, which is a tool for charged-particle optics calculations in the accelerators and beam transport systems. It was developed in CERN but since it can handle various accelerators and problems it is used in many other laboratories. We will use MAD-X [17] to check if it is possible to recreate the most basic beam parameters with the FEM solution obtained.

8.1   Proton Synchrotron lattice model

The MAD model of the PS lattice [8] has been divided into 10 sequences of magnetic elements, that correspond to 10 PS ring sections. Each section consist of 10 main magnetic units as well as other accelerator equipment. The magnet itself is modelled as a sequence of MAD elements [12]:

- SBEND – a sector bending magnet described with dipole, quadrupole and sextupole components,

- MULTIPOLE – a thin-lens magnet described with up to 20-pole component,

- DRIFT – a space element with no real attribute of the magnetic field.

Multipoles above the dipole are defined as

$$K_n = \frac{1}{B_y \rho} \frac{\partial^n B_y}{\partial x^n} \qquad n = 1, 2, \ldots \tag{8.1}$$

---

[1]Methodical Accelerator Design

60

defocusing higher   thin-lens for   focusing higher
order components   powering upgrade   order components
(MULTIPOLE)   (MULTIPOLE)   (MULTIPOLE)

drift space   defocusing   junction   focusing   drift space
(DRIFT)   half-unit   (SBEND)   half-unit   (DRIFT)
            (SBEND)   (SBEND)
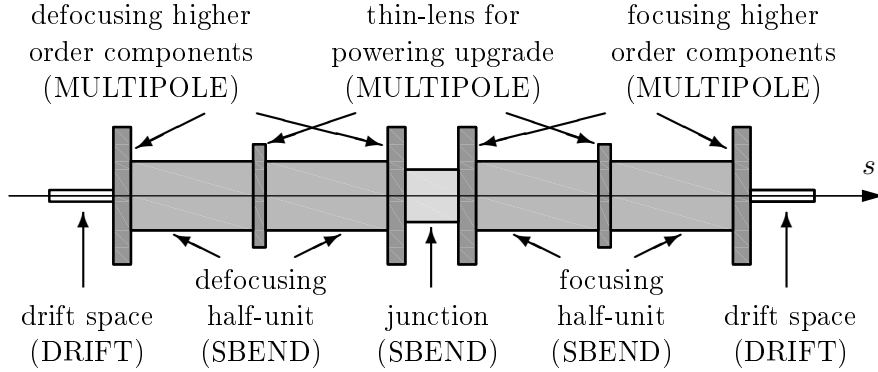
Figure 8.1: Diagram of the PS lattice model in MAD.

where $B_y\rho$ is the beam rigidity. Detailed description of the MAD model created in 1992 can be found in [23], and the diagram of its actual state is presented in Fig. 8.1.

Apart from derived multipole components, which were calculated for a specific working point, there is a number of energy-dependent parameters that cannot be calculated using the 2D ANSYS model:

- central junction parameters: effective length L_J, quadrupole K_{1J} and sextupole K_{2J} components,

- effective magnetic length, which results from the fact that magnetic field does not vanish suddenly at the end of the magnet, but in the optics model the field is assumed to be uniformly distributed along the element. The effective length is introduced to ensure that the field integral through the magnet remains unchanged.

$$B_{max} \times L_{ef} = \int_{-\infty}^{\infty} B(s)\mathrm{d}s$$
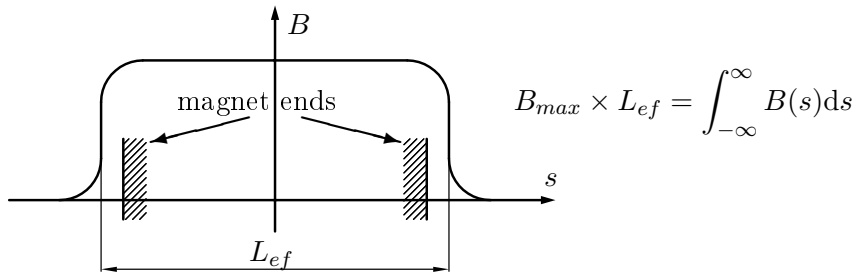
Figure 8.2: Effective magnetic length.

- pole-face angles ε_F and ε_D correcting the difference between the magnet and the stray field geometry at the magnet ends, which is caused by the shape of the pole profile.
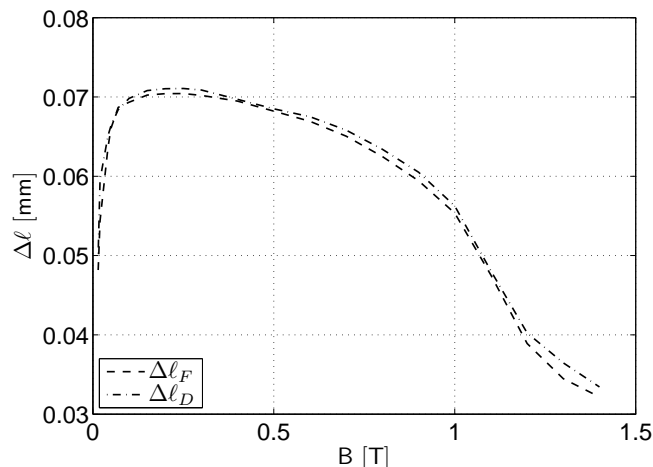
Figure 8.3: Focusing and defocusing correction bending length [27].

The PS lattice model in the latest form is adapted to use the multipole components derived from beam based measurements [6]. Multipole values were fitted with the use of virtual thin-lens elements to reproduce measured beam parameters. However, the parameters of SBEND elements mentioned above were fixed to one value, therefore, for the needs of this study, the model has been modified so that the elements length changes with the energy.

In order to perform the analysis, the measurement data concerning all these parameters is needed for various field levels. The effective bending lengths can be derived from the correction bending lengths $\Delta\ell_F$ and $\Delta\ell_D$, which are given in [27], as below:

$$
\begin{aligned}
L_{efF} &= L_F + \Delta\ell_F, \\
L_{efD} &= L_D + \Delta\ell_D,
\end{aligned}
\tag{8.2}
$$

where $L_F = 2126$ mm and $L_D = 2134$ mm are focusing and defocusing half-unit lengths respectively. Pole-face angles and junction parameters were much more problematic since they were not measured in such a wide range of field levels as correction bending lengths. Available data come from old MAD-8 [16] input files of the PS lattice [24], which are dated 1992, but only for momentum of 3.5, 24 and 26 GeV/c. Thus, the calculations are carried out for these specific working points and their close neighbourhood where parameters can be extrapolated.

8.2 MAD-8 calculations using magnetic field measurements and FEM solution

Optics calculation were at first performed using a MAD-8 model. Since it was intentionally developed for the use with measured magnetic field data, no major modifications were needed to use it with the ANSYS solution. Available

input files contain multipole components and energy-dependent parameters for three different coils powering configurations called B, C and E — which are shown in Table 5.1 — that were applied in ANSYS model. Tables 8.1–8.3 present calculated beam parameters — the tune and the chromaticity, which are mainly governed by quadrupolar and sextupolar components, respectively. However, these parameters are also dependent on the total field since given multipoles are normalized by beam rigidity $B_y\rho$ as in Eq. (8.1).

The cycle E, the solution of which was discussed in Section 6.2, is a low energy cycle with adequately low magnetic field. Beam parameters at this working point show relatively small sensitivity to multipole discrepancies. The difference between the measured and the calculated quadrupole components that has reached 1.2% resulted in the tune error that has not exceeded 0.12%. Very small sextupole components have produced similar values of chromaticity.

	Measurement	ANSYS	δ [%]
Q_h	6.2414	6.2490	-0.12
Q_v	6.2917	6.2996	-0.12
ξ_h	-2.7041	-2.6227	3.01
ξ_v	0.6516	0.5746	11.83

Table 8.1: Parameters of the E cycle beam calculated with MAD-8 model using measurements and ANSYS solution for $\lambda = 0.925$.

The cycle B is a high energy working point that does not have the figure-of-eight powered. Thus, the fields in focusing and defocusing half-units are very similar and it seems that beam parameters are more sensitive to the choice of the packing factor. Discrepancies of dipole and quadrupole components calculated for packing factor $\lambda = 0.925$ were less than 0.5%, while tune discrepancies, which are shown in Table 8.2, are equal to $\delta_{Q_h} = 0.65\%$ and $\delta_{Q_v} = -0.51\%$. The application of separate factors for focusing and defocusing parts of the magnet — $\lambda_F = 0.928$ and $\lambda_D = 0.923$ — has decreased those discrepancies to $\delta_{Q_h} = 0.14\%$ and $\delta_{Q_v} = -0.04\%$. The difference between chromaticities has not improved significantly, nevertheless the values obtained are to some extent similar.

	Measurement	ANSYS	δ [%]
Q_h	6.2090	6.1689	0.65
Q_v	6.3341	6.3664	-0.51
ξ_h	-1.2625	-1.3522	-7.11
ξ_v	-0.8234	-0.7404	10.07

Table 8.2: Parameters of the B cycle beam calculated with MAD-8 model using measurements and ANSYS solution for $\lambda = 0.925$.

The cycle C is the high energy working point, which is similar to LHC cycle presented in Section 6.4. Its currents configuration is set so that all auxiliary coils are powered to correct the effect of iron saturation, hence the field in magnet halves differs significantly. For this reason the separate packing factors are not necessary or even ill-advised in this case. The difference between tunes calculated with ANSYS solution for $\lambda = 0.925$ and those calculated using measured magnetic field are equal to $\delta_{Q_h} = 0.13\%$ and $\delta_{Q_v} = -0.15\%$, while the use of the same separate factors as in the previous cycle has deteriorated these values to $\delta_{Q_h} = -0.66\%$ and $\delta_{Q_v} = 0.62\%$. As it can be seen in Table 8.3, compared chromaticity values are completely divergent. Such difference is caused by sextupole discrepancies, which are relatively small (see Tables A.5 and A.6) compared to the experimental error, but the sextupole itself is much higher, which makes discrepancies more important.

	Measurement	ANSYS	δ [%]
Q_h	6.2343	6.2259	0.13
Q_v	6.2617	6.2710	-0.15
ξ_h	-0.4080	0.0577	114.15
ξ_v	0.3755	-0.0706	118.79

Table 8.3: Parameters of the C cycle beam calculated with MAD-8 model using measurements and ANSYS solution for $\lambda = 0.925$.

The comparison of beam parameters calculated using ANSYS solution and measured magnetic field has given fairly good results, for tune values in particular. However, it has to be noted that these parameters are burdened with uncertainties since the maximum absolute relative error of measured multipoles is $\varepsilon_B \leq \pm 0.2\%$ for dipole and $\varepsilon_G \leq \pm 0.25\%$ for quadrupole, while the error on the sextupole reaches 45% [11]. Furthermore, the estimation of the packing factor for 2D analysis is ambiguous since apart from laminations it also takes into account air gaps between magnet blocks.

8.3 MAD-X solution comparison with measured beam parameters

MAD-X model was chosen in order to perform a comparison of the numerical solution with measured beam parameters. However, its version from 2007, which was up-to-date with the actual machines state, had to be modified to use the calculated multipoles as input. Horizontal and vertical tune data was measured at various energy levels using specifically designed powering programme, which is presented in Fig. 8.4.

The calculated and measured tune values are shown in Fig. 8.5. It can be seen that the numerical solution for $\lambda = 0.925$ does not exactly match the
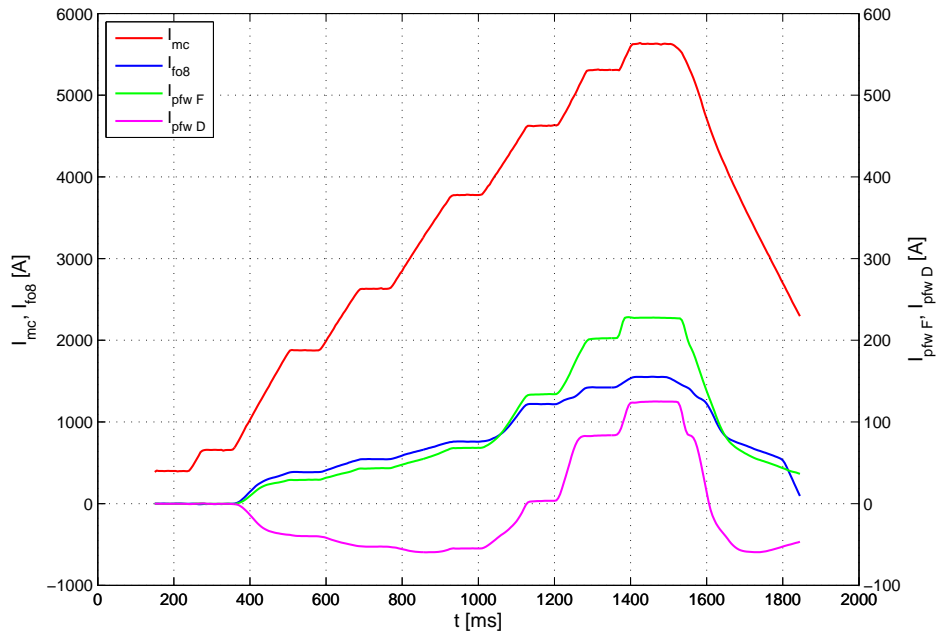
Figure 8.4: Powering programme for beam parameters measurements.
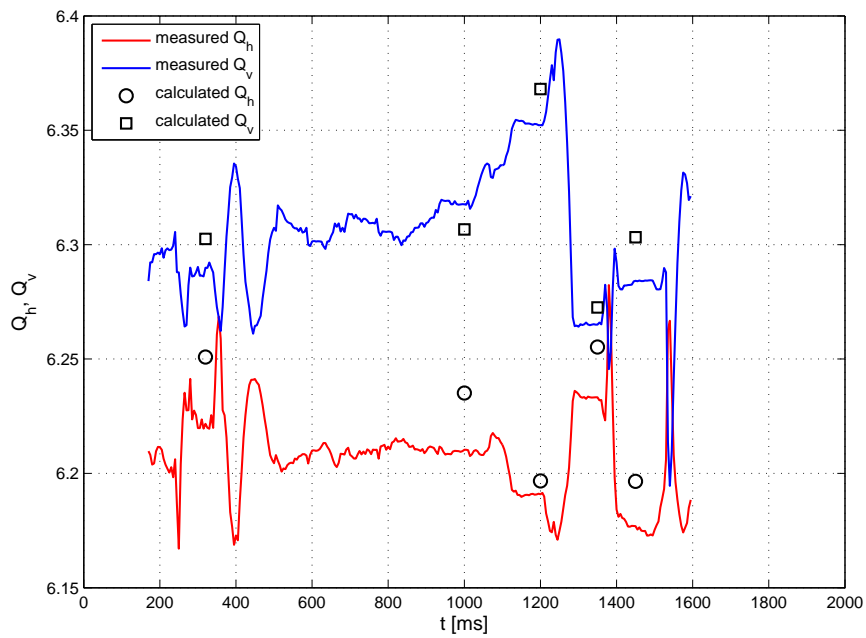
Figure 8.5: Measured and calculated tune values.

measurement, however, it does fit the actual tune values within the error of $\pm 0.47\%$, while the tune measured had a precision of the order of 1×10^{-3}. This gives very good approximation of the tune behaviour, but the accuracy has to be improved. Wrongly chosen betatron tune values lead to transverse resonant conditions that cause betatron amplitude growth and as a consequence of this — particles losses on the accelerator vacuum chamber. Obtaining the convergence of calculated and measured chromaticity has yet turned out to be not correct with existing MAD-X model and FEM solution, however, several limitations of the MAD-X model have been discovered.

8.3.1   Limitations of the Proton Synchrotron MAD-X model

Apart from uncertainties connected with the FEM model (e.g. the packing factor estimation) the accuracy of the PS lattice model is limited by lack of energy-dependent parameters data and optical model simplifications.

Parameters data that can be found in MAD-8 input files (pole-face angles and junction parameters) were measured only at few specific energy levels, while correction bending lengths that come from [27] were measured in 1959 on the prototype magnet unit that was not equipped with any auxiliary coils. Furthermore, the old MAD model was designed in a way that it was possible to calculate the beam circulating in both clockwise and anti-clockwise directions, but because of that half-units were modelled as symmetrical elements. Internal and external pole-face angles of the same type have the same value, while internal angles in real magnets are altered by interacting fields of both half-units. The correction of this simplification is introduced in junction element, but it makes the estimation of junction parameters more complicated.

Another limitation of the model is lack of distinction between odd and even magnets, which have separate powering circuits. The powering scheme for 5 current mode separates narrow power converter circuit for odd and even magnets, which gives 7 power converters in total:

- 1 figure-of eight circuit,

- 2 wide pole-face-windings circuits (focusing and defocusing),

- 4 narrow pole-face-windings circuits (odd and even of focusing and defocusing magnets).

To avoid asymmetry between odd and even circuits a set of resistors was introduced, but it was not readjusted after a renovation campaign in which more even than odd magnets were refurbished. The current difference of about 1 A in pole-face-windings of the same type is enough to noticeably contribute to the precision loss [15], though in lesser extent than previously discussed factors.

Chapter 9

Conclusion

The ability to recreate optical parameters of the Proton Synchrotron using computer programs, such as MAD, is of great importance to perform future development of this accelerator. The main task of this thesis was to develop the finite-element model of the PS magnet that can be used, instead of measurements, to obtain multipole components of the magnetic field in the magnet pole-gap. The secondary task was to determine whether the FE solution can be used as MAD input to recreate beam parameters.

The 2D analysis performed using ANSYS software has given very good results. Although the dipole component was overestimated by about 0.5% compared to measurements, the quadrupole and the sextupole components were well within experimental error bars. The simulation has also shown that the solution is very sensitive to the magnetic material data of the iron and the packing factor in particular. The laminated structure of iron blocks forces the magnetic data reduction with the packing factor. However, since air gaps between blocks also contribute to the field drop an analytical factor estimation becomes uncertain.

The packing factor estimation for the 3D analysis is much more straightforward since it only takes into account the influence of laminations, and the value of $\lambda = 0.9496$ has given very good results. The most important limiting factor in the 3D analysis was the number of finite elements used in the simulation. It was possible to obtain the solution accuracy of $\delta_B \leq \pm 0.26\%$ and $\delta_G \leq \pm 1.73\%$ using locally refined models with up to 1.5×10^6 finite elements. The comparison of the numerical solution with measurements has shown difference of about 0.4% for dipole and 0.2% for quadrupole components, which are comparable with 2D results. However, the solution quality was not high enough so as to obtain the reliable value of the sextupole component. Therefore, it was only possible to compare the individual behaviour of sextupoles and both of them, the calculated and the measured one, had very similar shape and values. The field analysis in the areas of the central junction and magnet ends has shown slightly bigger discrepancies but in these regions the calcu-

lated field is affected by coils simplifications and isotropic iron properties to a greater extent than within central part of the magnet half-units.

The MAD simulation performed with the use of 2D ANSYS solution and measured magnetic field has shown that the influence of the packing factor estimation on the calculated beam parameters increases with the energy. The influence was especially significant in the case of the calculated tune discrepancies in high energy cycles with and without the use of figure-of-eight-loop correction. The comparison of calculated and measured beam parameters is affected by more error sources. Some input parameters, such as junction multipoles and pole-face angles, were available only at limited number of energy levels and could not be precisely extrapolated to other working points. Besides that, there are some MAD model simplifications and magnets powering issues that are not considered in the model. However, despite all these error sources, the tune comparison had shown discrepancies of about $\pm 0.47\%$ compared to the actual tune values, which gives a good knowledge about tune behaviour but the accuracy is not sufficient to use the results in machine developments.

This study has given useful information about the present PS MAD model limitations that should be eliminated. It has also shown that both the 2D and the 3D magnet models that were developed can be useful source of information about the magnetic field and missing energy-dependent parameters data, though some accuracy problems that concern junction and magnet ends regions of the 3D model should be resolved first.

Bibliography

[1] ANSYS, Inc. *ANSYS Release 11.0 Documentation*, 2007.

[2] Asklöv, A. *Magnetic measurement on the CERN proton synchrotron*, Master's Thesis, LITH-IFM-EX-05/1463-SE, Linköpings universitet, Linköping, 2005.

[3] Auchmann, B. *ROXIE User's Documentation*, CERN, Geneva, 2007, `http://at-mei-fp.web.cern.ch/at-mei-fp/`.

[4] Bastos, J.P.A. and Sadowski, N. *Electromagnetic Modelling by Finite Elements Methods; electronic version*, Dekker, Abingdon, 2003.

[5] Bryant, P.J. and Johnsen, K. *The principles of circular accelerators and storage rings*, Cambridge Univ. Press, Cambridge, 1993.

[6] Cappi, R., Giovannozzi, M., Martini, M., Métral, E., Métral, G., Steerenberg, R., Müller, A.S. *Optics Studies for the CERN Proton Synchrotron Machine: Linear and Nonlinear Modelling using Beam Based Measurements*, CERN-AB-2003-017-ABP, CERN, Geneva, May 2003.

[7] *CERN Drawing Directory*, CERN, Geneva, 2007, `https://edms.cern.ch/cdd/plsql/c4w_guided.guided_drawing?cookie=1168642&p_equip_id=MMU__`.

[8] *CERN Optics repository*, CERN, Geneva, 2008, `http://isscvs.cern.ch/cgi-bin/viewcvs-all.cgi/PS/PSRing/?root=camif`.

[9] *CERN Webpage*, CERN, Geneva, 2008, `http://www.cern.ch/`.

[10] Cornuet D. Private communication, CERN, Geneva, 2007.

[11] Cornuet D. and Sharifullin Z. *Magnetic measurements on the PS magnet unit 17 with Hall probes*, Technical Report AT-MA Note 92-93, CERN, Geneva, 1992.

[12] Grote, H. *MAD-X User's guide*, CERN, Geneva, 2002, `http://mad.web.cern.ch/mad/uguide.html`.

[13] Jain, A.K. *Basic theory of magnets* in CAS - CERN Accelerator School: Measurement and Alignment of Accelerator and Detector Magnets, Turner, S. Ed. CERN, Geneva, August 1998.

[14] Juchno, M. *Status of the PS magnet model*, AB-ABP/LII Section meeting, CERN, Geneva, January 2007, `http://ab-dep-abp.web.cern.ch/ab-dep-abp/LIS/Minutes/2007/20070129/mjuchno.pdf`.

[15] Juchno, M. *Final report on ANSYS magnet model study*, AB-ABP/LIS Section meeting, CERN, Geneva, October 2007, `http://ab-dep-abp.web.cern.ch/ab-dep-abp/LIS/Minutes/2007/20071015/juchno.pdf`.

[16] *MAD-8 Home Page*, CERN, Geneva, 2002, `http://mad.web.cern.ch/mad/mad8web/mad8.html`.

[17] *MAD-X Home Page*, CERN, Geneva, 2005, `http://mad.web.cern.ch/mad/`.

[18] Martini, M. *An introduction to transverse beam dynamics in accelerators*, CERN, Geneva, 1996.

[19] MathWorks, Inc. *MATLAB R2007b Documentation*, 2007.

[20] Preis, K., Biro, O., Magele, C.A., Renhart, W., Richer, K.R., Vrisk, G. *Numerical analysis of 3D magnetostatic fields*, IEEE-TMAG, 1991.

[21] Regenstreif, E. *The CERN Proton Synchrotron*, Technical Report 59-29, CERN, Geneva, August 1959.

[22] Reich, K.H. *The CERN Proton Synchrotron magnet*, Technical Report MPS/Int. DL 63-13, CERN, Geneva, 1963.

[23] Risselada T. *Beam Optics Data for the PS Ring and its Transfer Lines*, PS-PA Note 92-04, CERN, Geneva, 1992.

[24] Risselada T. Private communication, CERN, Geneva, 2007.

[25] Russenschuck, S. *Electromagnetic Design and Mathematical Optimization Methods in Magnet Technology*, eBook, ISBN: 92-9083-242-8.

[26] Skoczeń, B. *Compensation Systems for Low Temperature Applications*, Springer-Verlag, Berlin, Heidelberg, 2004.

[27] Umstätter, H.H. *The effective length of the PS magnets at various field levels*, CERN/MPS/SR 72-1, CERN, Geneva, 1972.

[28] Wiedemann, H. *Particle Accelerator Physics: basic principles and linear beam dynamics*, Springer-Verlag, Berlin, 1993.

Appendix A

Multipoles used in MAD-8 calculations

Cycle E multipoles

	Measurement	ANSYS	Relative difference δ [%]
K_{0F}	0.1664	0.1680	-0.97 %
$K_{1F} \times B\rho$	0.6824	0.6901	-1.12 %
$K_{2F} \times B\rho$	-0.0220	-0.0126	42.74 %
$K_{3F} \times B\rho$	0.6851	0.1421	79.26 %
$K_{4F} \times B\rho$	22.3273	4.5000	79.85 %
$K_{5F} \times B\rho$	-2246.3035	-776.3666	65.44 %
K_{0D}	0.1665	0.1680	-0.88 %
$K_{1D} \times B\rho$	-0.6848	-0.6914	-0.97 %
$K_{2D} \times B\rho$	-0.0011	-0.0036	-231.55 %
$K_{3D} \times B\rho$	-0.5722	-0.1490	73.97 %
$K_{4D} \times B\rho$	17.0218	0.4133	97.57 %
$K_{5D} \times B\rho$	1924.4380	680.9651	64.61 %

Table A.1: Focusing and defocusing multipoles of magnets with the iron core internal to the ring.

	Measurement	ANSYS	Relative difference δ [%]
K_{0F}	0.1665	0.1680	-0.88
$K_{1F} \times B\rho$	0.6848	0.6914	-0.97
$K_{2F} \times B\rho$	-0.0011	-0.0036	-231.55
$K_{3F} \times B\rho$	0.5722	0.1490	73.97
$K_{4F} \times B\rho$	17.0218	0.4133	97.57
$K_{5F} \times B\rho$	-1924.4380	-680.9651	64.61
K_{0D}	0.1664	0.1680	-0.97
$K_{1D} \times B\rho$	-0.6824	-0.6901	-1.12
$K_{2D} \times B\rho$	-0.0220	-0.0126	42.74
$K_{3D} \times B\rho$	-0.6851	-0.1421	79.26
$K_{4D} \times B\rho$	22.3273	4.5000	79.85
$K_{5D} \times B\rho$	2246.3035	776.3666	65.44

Table A.2: Focusing and defocusing multipoles of magnets with the iron core external to the ring.

Cycle B multipoles

	Measurement	ANSYS	Relative difference δ [%]
K_{0F}	1.1484	1.1532	-0.42 %
$K_{1F} \times B\rho$	4.7621	4.7755	-0.28 %
$K_{2F} \times B\rho$	0.5063	0.4235	16.35 %
$K_{3F} \times B\rho$	-18.2078	-17.8298	2.08 %
$K_{4F} \times B\rho$	-67.3263	271.0435	502.58 %
$K_{5F} \times B\rho$	-33828.1094	-36188.5530	-6.98 %
K_{0D}	1.1470	1.1523	-0.46 %
$K_{1D} \times B\rho$	-4.7652	-4.7885	-0.49 %
$K_{2D} \times B\rho$	0.7086	0.7176	-1.27 %
$K_{3D} \times B\rho$	18.1574	17.3909	4.22 %
$K_{4D} \times B\rho$	-129.2963	285.9720	321.18 %
$K_{5D} \times B\rho$	35118.5742	41241.6990	-17.44 %

Table A.3: Focusing and defocusing multipoles of magnets with the iron core internal to the ring.

	Measurement	ANSYS	Relative difference δ [%]
K_{0F}	1.1484	1.1534	-0.43
$K_{1F} \times B\rho$	4.7621	4.7756	-0.28
$K_{2F} \times B\rho$	0.5063	0.3912	22.72
$K_{3F} \times B\rho$	-18.2078	-17.2734	5.13
$K_{4F} \times B\rho$	-67.3263	250.8840	472.64
$K_{5F} \times B\rho$	-33828.1094	-37603.1180	-11.16
K_{0D}	1.1470	1.1521	-0.45
$K_{1D} \times B\rho$	-4.7652	-4.7885	-0.49
$K_{2D} \times B\rho$	0.7086	0.7500	-5.84
$K_{3D} \times B\rho$	18.1574	17.9507	1.14
$K_{4D} \times B\rho$	-129.2963	312.5467	341.73
$K_{5D} \times B\rho$	35118.5742	38350.1700	-9.20

Table A.4: Focusing and defocusing multipoles of magnets with the iron core external to the ring.

Cycle C multipoles

	Measurement	ANSYS	Relative difference δ [%]
K_{0F}	1.2337	1.2419	-0.67 %
$K_{1F} \times B\rho$	5.2088	5.2379	-0.56 %
$K_{2F} \times B\rho$	2.4709	2.5295	-2.37 %
$K_{3F} \times B\rho$	-30.0813	-29.8562	0.75 %
$K_{4F} \times B\rho$	577.8979	365.9082	36.68 %
$K_{5F} \times B\rho$	-76500.0000	-95634.0740	-25.01 %
K_{0D}	1.2818	1.2917	-0.77 %
$K_{1D} \times B\rho$	-5.1980	-5.2455	-0.91 %
$K_{2D} \times B\rho$	-1.2830	-1.0420	18.79 %
$K_{3D} \times B\rho$	32.9774	35.0419	-6.26 %
$K_{4D} \times B\rho$	119.8827	-159.6368	233.16 %
$K_{5D} \times B\rho$	88941.8125	90598.2660	-1.86 %

Table A.5: Focusing and defocusing multipoles of magnets with the iron core internal to the ring.

	Measurement	ANSYS	Relative difference δ [%]
K_{0F}	1.2330	1.2428	-0.79
$K_{1F} \times B\rho$	5.1971	5.2407	-0.84
$K_{2F} \times B\rho$	2.2857	2.4738	-8.23
$K_{3F} \times B\rho$	-30.8848	-29.3511	4.97
$K_{4F} \times B\rho$	485.6216	287.1356	40.87
$K_{5F} \times B\rho$	-76252.6250	-106242.4700	-39.33
K_{0D}	1.2829	1.2907	-0.62
$K_{1D} \times B\rho$	-5.2115	-5.2434	-0.61
$K_{2D} \times B\rho$	-1.0767	-0.9772	9.24
$K_{3D} \times B\rho$	32.3055	35.1156	-8.70
$K_{4D} \times B\rho$	210.7191	-172.8100	182.01
$K_{5D} \times B\rho$	86301.5625	94642.3830	-9.66

Table A.6: Focusing and defocusing multipoles of magnets with the iron core external to the ring.

Appendix B

Extensive summary in Polish

Obszerne streszczenie w języku polskim

B.1 Wstęp

Synchrotron Protonowy (PS) jest pierwszym, wybudowanym w 1959 roku, synchrotronem w Europejskiej Organizacji Badań Jądrowych (CERN), uznawanej za największe na świecie laboratorium fizyki cząstek elementarnych. Akcelerator ten przez wiele lat służył jako główne narzędzie w programie badawczym CERN, a od lat 70-tych, gdy zaczęto dołączać nowe akceleratory do kompleksu badawczego, dostarcza cząstki elementarne do innych maszyn.
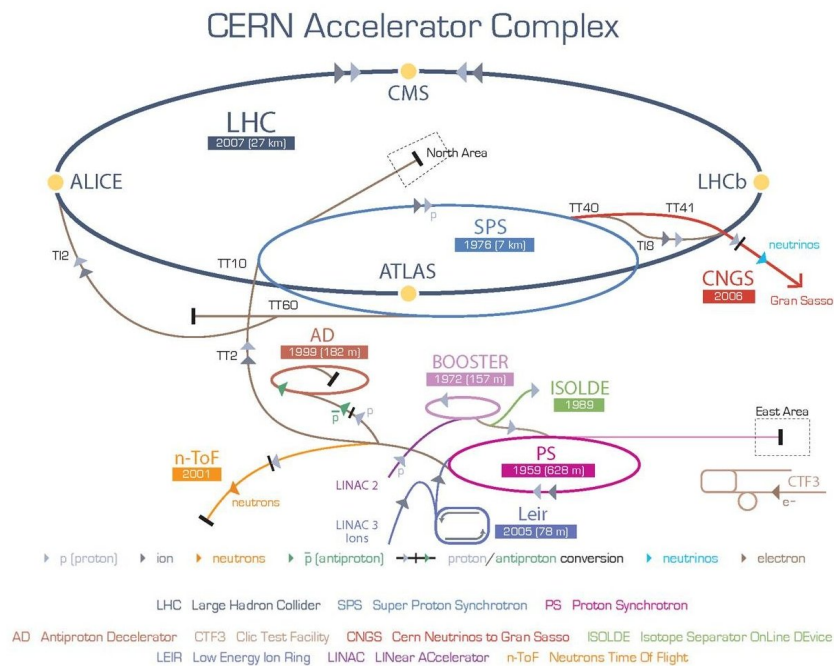
Rysunek B.1: Kompleks akceleratorów w CERN.

Celem niniejszej pracy była analiza numeryczna modelu głównego magnesu Synchrotronu Protonów. Znajomość rozkładu pola magnetycznego jest niezbędna do odtworzenia zachowania krążącej wiązki cząstek elementarnych w akceleratorze oraz jego dostosowania do przyszłych potrzeb. Dzięki analizie numerycznej nie jest potrzebne przeprowadzanie czasochłonnych pomiarów pola magnetycznego, których w praktyce nie da się przeprowadzić dla wszystkich potrzebnych punktów pracy akceleratora.

Do numerycznej analizy 2D i 3D został wykorzystany pakiet elementów skończonych ANSYS. Uzyskany rozkład multipolarny pola magnetycznego został następnie wykorzystany do odtworzenia najbardziej podstawowych parametrów krążącej w akceleratorze wiązki. Do tego celu zostało użyte oprogramowanie do projektowania akceleratorów MAD.

B.2 Elektromagnetyzm i podstawy optyki wiązki

Do opisu problemu magnetostatycznego, którego wielkości są niezależne od czasu ($\partial/\partial t = 0$), wykorzystywane są następujące równania Maxwella
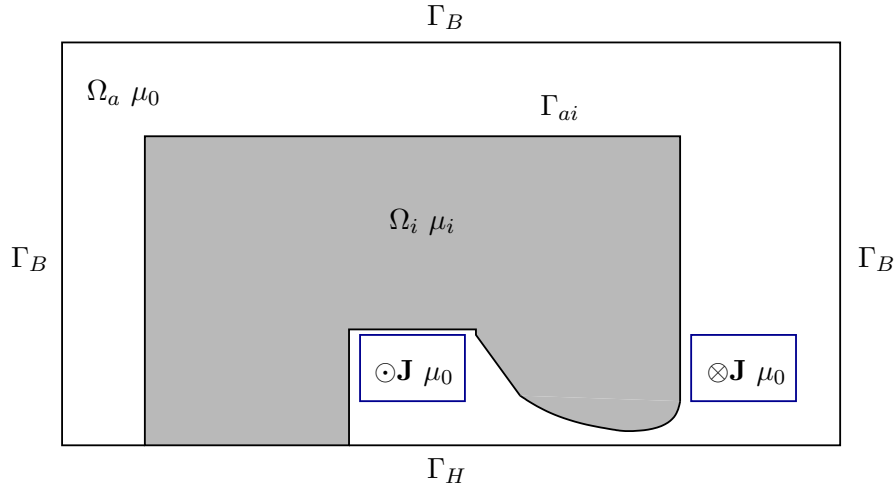
$$\operatorname{rot} \mathbf{H} = \mathbf{J}, \tag{B.1}$$

$$\operatorname{div} \mathbf{B} = 0, \tag{B.2}$$

do których należy dodać równanie konstytutywne materiału magnetycznego

$$\mathbf{B} = \mu \mathbf{H}, \tag{B.3}$$

gdzie $\mathbf{H}$ jest natężeniem pola magnetycznego, $\mathbf{B}$ jest indukcją magnetyczną, $\mathbf{J}$ jest gęstością prądu a μ jest przenikalnością magnetyczną ośrodka.

Rysunek B.2: Obszary oraz ich brzegi w problemie magnesu PS.

Stosując twierdzenie Helmholtza oraz cechowanie Coulomba możemy zapisać problem przy pomocy całkowitego potencjału wektorowego $\mathbf{A}$:

$$\operatorname{rot} \frac{1}{\mu} \operatorname{rot} \mathbf{A} - \operatorname{grad} \frac{1}{\mu} \operatorname{div} \mathbf{A} = \mathbf{J} \qquad \text{in } \Omega, \tag{B.4}$$

przyjmując następujące warunki brzegowe w celu zagwarantowania jednoznaczności rozwiązania

$$\mathbf{A} \cdot \mathbf{n} = 0 \qquad \text{on } \Gamma_H, \tag{B.5}$$

$$\frac{1}{\mu} (\operatorname{rot} \mathbf{A}) \times \mathbf{n} = 0 \qquad \text{on } \Gamma_H, \tag{B.6}$$

$$\frac{1}{\mu} \operatorname{div} \mathbf{A} = 0 \qquad \text{on } \Gamma_B, \tag{B.7}$$

$$\mathbf{n} \times (\mathbf{A} \times \mathbf{n}) = 0 \qquad \text{on } \Gamma_B, \tag{B.8}$$

$$\left[\frac{1}{\mu}(\operatorname{rot}\mathbf{A})\times\mathbf{n}\right]_{ai}=0 \qquad \text{on } \Gamma_{ai}, \tag{B.9}$$

$$\left[\frac{1}{\mu}\operatorname{div}\mathbf{A}\right]_{ai}=0 \qquad \text{on } \Gamma_{ai}, \tag{B.10}$$

$$[\mathbf{A}]_{ai}=0 \qquad \text{on } \Gamma_{ai}. \tag{B.11}$$

Rozkład multipolarny pola magnetycznego w przestrzeni wolnej od źródeł prądu można otrzymać z rozwiązania powyższego problemu w układzie biegunowym

$$A_z(r,\varphi)=\sum_{n=1}^{\infty}r^n(\mathcal{C}_n\sin n\varphi-\mathcal{D}_n\cos n\varphi), \tag{B.12}$$

skąd otrzymujemy składowe indukcji magnetycznej

$$B_r(r,\varphi)=\frac{1}{r}\frac{\partial A_z}{\partial\varphi}=\sum_{n=1}^{\infty}nr^{n-1}(\mathcal{C}_n\cos n\varphi+\mathcal{D}_n\sin n\varphi), \tag{B.13}$$

$$B_\varphi(r,\varphi)=-\frac{\partial A_z}{\partial r}=\sum_{n=1}^{\infty}nr^{n-1}(\mathcal{C}_n\sin n\varphi-\mathcal{D}_n\cos n\varphi), \tag{B.14}$$

gdzie $\mathcal{C}_n$ i $\mathcal{D}_n$ są współczynnikami multipoli pola magnetycznego niezbędnymi w obliczeniach ruchu cząstek elementarnych w akceleratorze.

Multipole	Magnesy skośne	Magnesy normalne
Dipole, n=1	$B_x=\mathcal{C}_1$	$B_x=0$
	$B_y=0$	$B_y=\mathcal{D}_1$
Quadrupole, n=2	$B_x=2\mathcal{C}_2x$	$B_x=2\mathcal{D}_2y$
	$B_y=-2\mathcal{C}_2y$	$B_y=2\mathcal{D}_2x$
Sextupole, n=3	$B_x=3\mathcal{C}_3(x^2-y^2)$	$B_x=6\mathcal{D}_3xy$
	$B_y=-6\mathcal{C}_3xy$	$B_y=3\mathcal{D}_3(x^2-y^2)$
Octupole, n=4	$B_x=4\mathcal{C}_4(x^3-3xy^2)$	$B_x=4\mathcal{D}_4(3x^2y-y^3)$
	$B_y=-4\mathcal{C}_4(3x^2y-y^3)$	$B_y=4\mathcal{D}_4(x^3-3xy^2)$
Decapole, n=5	$B_x=5\mathcal{C}_5(x^4-6x^2y^2+y^4)$	$B_x=20\mathcal{D}_5(x^3y-xy^3)$
	$B_y=-20\mathcal{C}_5(x^3y-xy^3)$	$B_y=5\mathcal{D}_5(x^4-6x^2y^2+y^4)$

Tablica B.1: Pola multipolarne w skośnych i normalnych magnesach.

Ruch cząstki elementarnej w polu elektromagnetycznym odbywa się pod wpływem siły Lorentza

$$\mathbf{F}=\frac{d\mathbf{p}}{dt}=e(\mathbf{E}+\mathbf{v}\times\mathbf{B}), \tag{B.15}$$

gdzie $\mathbf{p}=\gamma m\mathbf{v}$ jest pędem relatywistycznym, $\mathbf{v}$ prędkością, m masą a $\gamma=1/\sqrt{1-v^2/c^2}$ jest czynnikiem Lorentza.

Poprzeczny ruch cząstki elementarnej w krzywoliniowym układzie współrzędnych $(\mathbf{x}, \mathbf{y}, \mathbf{s})$ jest opisany przez równanie Hilla

$$u'' + K(s)u = \frac{\delta}{\rho}. \tag{B.16}$$

gdzie u oznacza zarówno x jak i y, $K(s)$ jest funkcją współczynników multipolarnych pola magnetycznego, $\delta = \Delta p/p_0$ jest dewiacją pędu a ρ promieniem krzywizny wiązki. Rozwiązanie nie zaburzonego równania ruchu cząstki ($\delta = 0$) ma postać

$$u(s) = \sqrt{\epsilon\beta(s)}\cos\left(\psi(s) + \phi\right), \tag{B.17}$$

gdzie ϵ i ϕ są stałymi zależnymi od warunków początkowych, $\beta(s)$ jest funkcją betatronową a $\psi(s)$ jest przesunięciem fazowym.

Wiązka cząstek może być opisana poprzez wiele parametrów. Do jednych z najważniejszych należą

- **tune** – liczba oscylacji betatronowych podczas jednego okrążenia po obwodzie akceleratora o długości C

$$Q = \frac{1}{2\pi}\int_s^{s+C}\frac{ds}{\beta(s)} \tag{B.18}$$

- **chromatyczność** – zmienność liczby oscylacji betatronowych ze zmianą pędu

$$\xi = \frac{\Delta Q/Q}{\Delta p/p_0}. \tag{B.19}$$

B.3 Metoda elementów skończonych w magnetostatyce

Metoda elementów skończonych jest jedną z najbardziej efektywnych i wszechstronnych metod numerycznych służących do przybliżonego rozwiązywania równań różniczkowych opisujących zjawiska mechaniki i fizyki. W analizie elektromagnetycznej najczęściej stosuje się ją w ujęciu residuów ważonych, wykorzystując metodę Galerkina. Metoda ta jest bezpośrednio oparta na równaniu różniczkowym problemu, które w przypadku 2D ma postać:

$$\frac{\partial}{\partial x}\left(\frac{1}{\mu}\frac{\partial A_z}{\partial x}\right) + \frac{\partial}{\partial y}\left(\frac{1}{\mu}\frac{\partial A_z}{\partial y}\right) = -J_z, \qquad (\text{B.20})$$

gdzie A_z jest składową z magnetycznego potencjału wektorowego a J_z jest składową wektora gęstości prądu elektrycznego.

Ogólny algorytm metody elementów skończonych można przedstawić następująco:

- Dyskretyzacja obszaru za pomocą elementów skończonych.

- Wyznaczenie funkcji aproksymacyjnych dla elementu oraz zbudowanie przy ich pomocy układu równań algebraicznych opisujących nieznane wielkości w węzłach elementu.

- Agregacja elementów mająca na celu zbudowanie układu równań algebraicznych dla całego obszaru.

- Uwzględnienie warunków brzegowych w globalnym układzie równań.

- Rozwiązanie globalnego układu równań algebraicznych.

- Obliczenie wartości nieznanej wielkości w dowolnym punkcie obszaru oraz wyznaczenie dodatkowych wielkości.

B.4   Charakterystyka magnesu

Główna cześć magnetyczna Synchrotronu Protonów składa się ze 100 magnesów umieszczonych w kołowym tunelu o średnicy 200 m. Każdy z tych magnesów składa się z dwóch pół-jednostek: skupiającej (F) i rozszczepiającej (D). Magnesy oddzielone są od siebie sekcjami prostymi (O), w których znajduje się pozostałe oprzyrządowanie, tworząc wzór FOFDOD. Każda pół-jednostka składa się z 5 identycznych żelaznych bloków o kształcie litery C z tzw. otwartym lub zamkniętym hiperbolicznym biegunem magnetycznym. Żelazne bloki o długości 417 mm, zbudowane z 1.5 mm grubości płyt stali z niskowęglowej walcowanej na zimno i wyżarzanej w temperaturze około 750 °C, tworzą w pojedynczym magnesie łuk o promieniu $r_o = 70.0789$ m i długości 4260 mm. Dzięki takiej budowie magnesy te spełniają zarówno funkcję zakrzywiającą jak i skupiającą wiązkę.
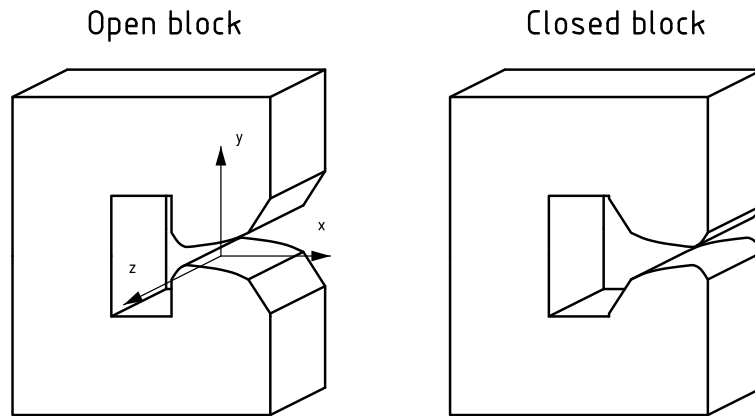

Rysunek B.3: Rodzaje bloków.

Wzbudzanie magnesów odbywa się poprzez trzy typy uzwojenia: uzwojenie główne, odpowiedzialne za podniesienie poziomu pola magnetycznego do odpowiedniej wartości, oraz poprzez dwa rodzaje uzwojenia korekcyjnego. Pierwsze uzwojenie korekcyjne obiega bieguny obu pół-jednostek tworząc pętlę o kształcie cyfry osiem (ang. figure-of-eight loop), natomiast drugie znajduje się na powierzchniach biegunów obu pół-jednostek (ang. pole-face-windings).
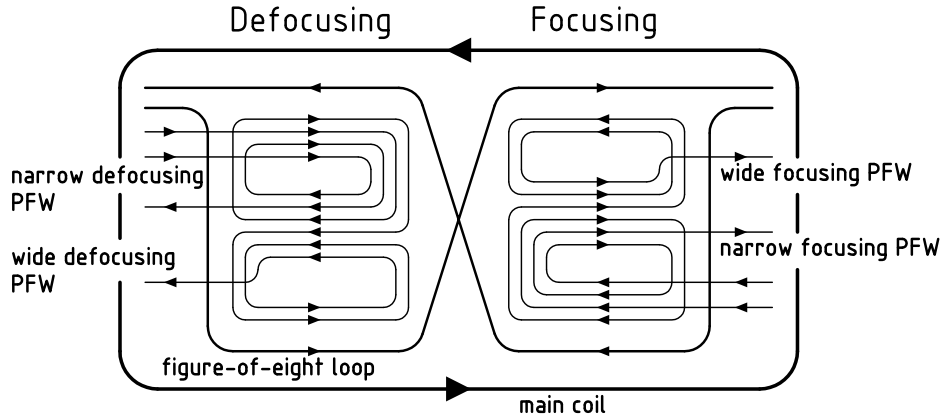
Rysunek B.4: Schemat uzwojenia.

B.5   Model numeryczny

Dwuwymiarowy model numeryczny magnesu został stworzony przy pomocy pakietu ANSYS, na podstawie dokumentacji technicznej [21][22][7]. Zawiera przekrój bloku magnesu, wszystkich trzech typów uzwojenia oraz obszary przestrzeni otaczającej magnes. Model elementów skończonych został zbudowany przy użyciu elementów PLANE53 [1], które są w stanie modelować materiał opisany nieliniowymi własnościami magnetycznymi.
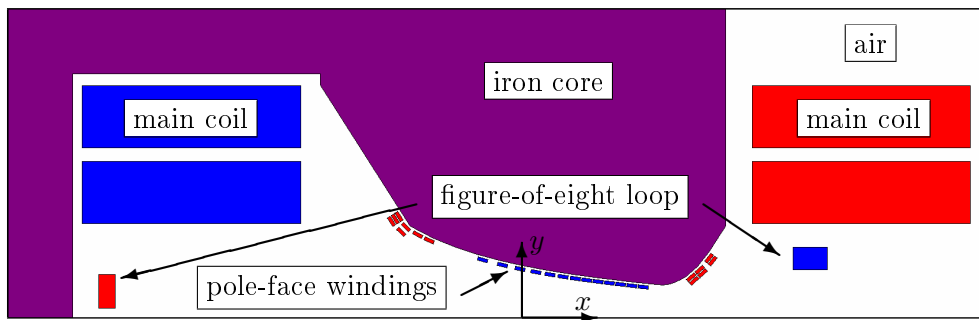
Rysunek B.5: Fragment geometrii modelu pół-jednostki skupiającej.

Nieliniowość materiału jest spowodowana zjawiskiem saturacji magnetycznej stali, która jest osiągnięta gdy zwiększanie natężenia zewnętrznego pola magnetycznego **H** nie powoduje dalszego przyrostu indukcji pola **B**. Ponadto, ze względu na laminacyjną strukturę bloków magnesu własności magnetyczne

stali użyte w obliczeniach muszą zostać zredukowane tzw. parametrem upakowania $\lambda = l_{Fe}/(l_{Fe} + l_0)$, gdzie l_{Fe} jest łączną grubością materiału magnetycznego o przenikalności magnetycznej stali μ_{Fe}, a l_0 łączną grubością izolacji o przenikalności próżni μ_0. Redukcja własności odbywa się zgodnie z wzorami:

$$\overline{\mu}_x = \overline{\mu}_y = \lambda\mu_{Fe} + (1 - \lambda)\mu_0, \qquad \overline{\mu}_z = \left(\frac{\lambda}{\mu_{Fe}} + \frac{1 - \lambda}{\mu_0}\right)^{-1},$$

gdzie $\overline{\mu}_x$, $\overline{\mu}_y$ i $\overline{\mu}_z$ są uśrednionymi kierunkowymi wartościami przenikalności magnetycznej stali. W przypadku analizy dwuwymiarowej jednoznaczne oszacowanie parametru upakowania nie jest możliwe ze względu na wpływ przestrzeni międzyblokowych które nie są uwzględnione płaskim modelu. Do obliczeń 2D przyjęto wartość $\lambda = 0.925$, natomiast w przypadku analizy 3D parametr upakowania wynosi $\lambda = 0.9496$.

W modelu zadane są dwa rodzaje warunków brzegowych:

- warunek prostopadłości strumienia magnetycznego do brzegu – zadany na osi geometrycznej symetrii modelu,

- warunek równoległości strumienia magnetycznego do brzegu – zadany za zewnętrznych brzegach dyskretyzowanego obszaru.

Obciążenie zostało zadane poprzez gęstość prądu przyłożonego w przekroju odpowiedniego przewodnika. Wartości zostały pobrane z programu sterującego cyklem wzbudzenia magnesu, dla stabilnego poziomu pola magnetycznego przy których przeprowadzana zostaje ekstrakcja wiązki.

| Cykl	I_{mc}	I_{f8}	I_{pfwF}	I_{pfwD}
E	669.2 A	—	—	—
A	2677.5 A	450.35 A	39.47 A	-45.08 A
B	4732.0 A	—	77 A	88 A
C	5413.15 A	1257.9 A	200.7 A	99.75 A
LHC	5400.56 A	1452.8 A	206.7 A	86.9 A

Tablica B.2: Konfiguracje obciążenia.

Post-processing został przeprowadzony za pomocą specjalnie do tego celu napisanym procedurą w języku APDL[1]. Procedury te dokonują dekompozycji obliczonego pola magnetycznego na jego składowe multipolarne wykorzystując do tego celu szeregi Fouriera. Następnie rozwiązanie w takiej postaci może być porównane z danymi dostępnymi dzięki przeprowadzonym w przeszłości kampanią pomiarowym [11][2] lub wykorzystane do obliczeń w programie MAD.

---

[1]ANSYS Parametric Design Language

B.6 Wyniki analizy 2D

Dla dwuwymiarowego modelu został przeprowadzony szereg testów sprawdzających zbieżność rozwiązania dla różnych parametrów symulacji. Przetestowano wpływ rozmiarów dyskretyzowanego obszaru na rozwiązanie oraz jego wrażliwość na dane materiałowe i zmianę parametru upakowania.
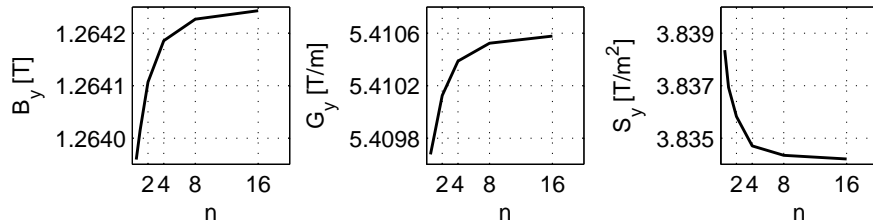
Rysunek B.6: Wpływ odległości brzegów $d = n \times 360$ mm dla $x = 0$.
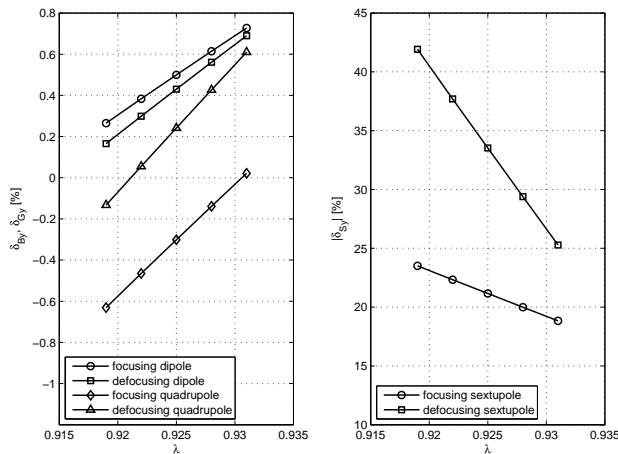
Rysunek B.7: Wrażliwość rozwiązania na parametr upakowania.

Zostało również przeprowadzone porównanie wyników symulacji uzyskanych za pomocą dwóch różnych programów: ANSYS wykorzystującym metodę elementów skończonych oraz ROXIE[2] wykorzystującym hybrydowe połączenie metody elementów skończonych i metody elementów brzegowych.

Następnie przedstawiono porównanie wyników obliczeń z danymi pomiarowymi dla trzech różnych cykli wzbudzenia: nisko-energetycznego typu E (wiązka o energii 3.5 GeV), średnio-energetycznego typu A (14 GeV) oraz wysoko-energetycznego typu LHC (26 GeV). Porównanie komponentów dipolowego oraz kwadrupolowego wypadło bardzo pomyślenie dla wszystkich trzech

---

[2]**R**outine for the **O**ptimization of magnet **X**-sections, **I**nverse field calculation and coil **E**nd design

Multipole	ANSYS	ROXIE	Błąd względny δ
dipole [T]	1.26424	1.26426	0.001%
quadrupole [T/m]	5.41058	5.40944	0.021%
sextupole [T/m^2]	3.83421	3.77767	1.475%

Tablica B.3: Porównanie wartości multipoli na trajektorii wiązki uzyskanych przy pomocy programów ANSYS i ROXIE.

cykli w obszarze pola generowanego przez hiperboliczną cześć bieguna. Nieco większe rozbieżności zostały zaobserwowane w obszarze przewężenia przestrzeni międzybiegunowej, gdzie pole magnetyczne osiąga największą wartość i ma silnie nieliniowy charakter. Ze względu na wysoki błąd pomiarowy komponentu sekstupolowego, a przez to oscylacyjny charakter dostępnych danych pomiarowych, porównanie tego komponentu mogło mieć jedynie charakter jakościowy. Dla cyklów nisko- i średnio-energetycznego zarówno kształt jak i wartości zostały bardzo dobrze odtworzone. W cyklu wysoko-energetycznym rozbieżności były większe ale kształt komponentu sekstupolowego został odwzorowany bardzo dobrze. Poniższa tablica i wykresy przedstawiają porównanie wyników obliczeń z pomiarami dla cyklu wysoko-energetycznego.

| Komponent	Pole skupiające (F)			Pole rozszczepiające (D)		
	Pomiary	Obliczenia	Błąd	Pomiary	Obliczenia	Błąd
B$_y$ [T]	1.2295	1.2356	0.50%	1.2882	1.2938	0.43%
G$_y$ [T/m]	5.2440	5.2281	0.30%	-5.2212	-5.2332	0.23%
S$_y$ [T/m^2]	3.5843	2.8132	21.5%	-1.1155	-1.4257	27.8%

Tablica B.4: Porównanie obliczonych i zmierzonych komponentów pola na trajektorii wiązki dla cyklu LHC.
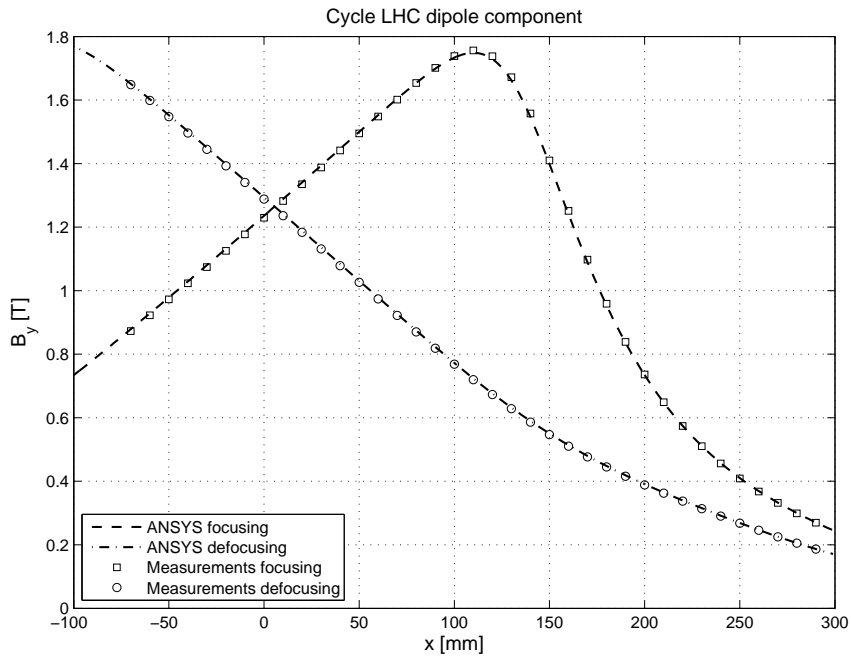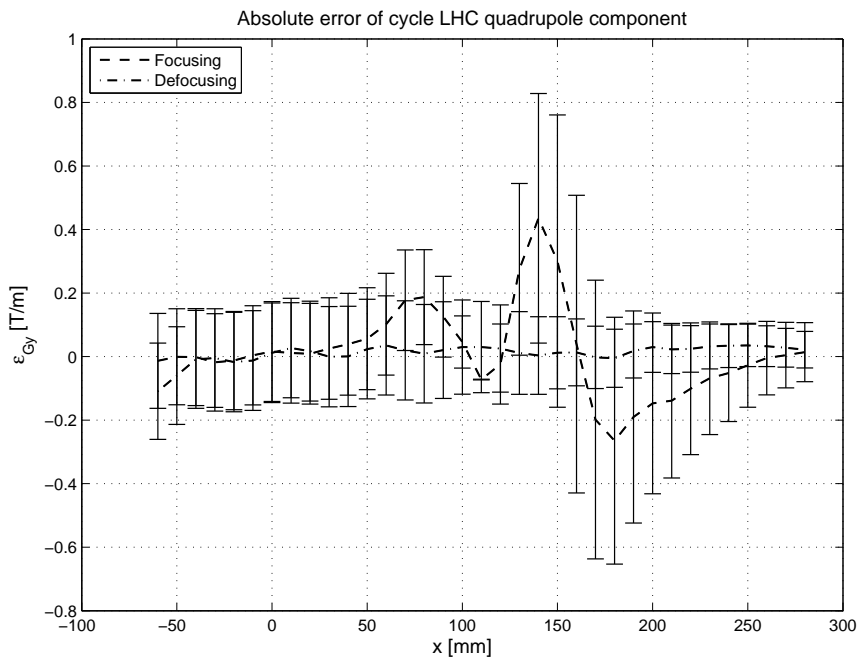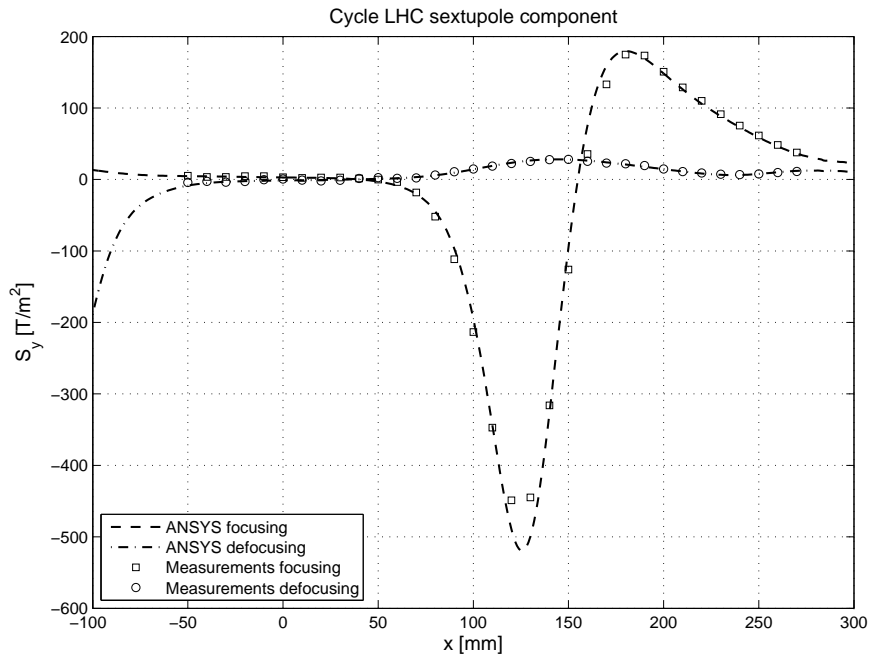
Rysunek B.8: Cykl LHC - komponent dipolowy.
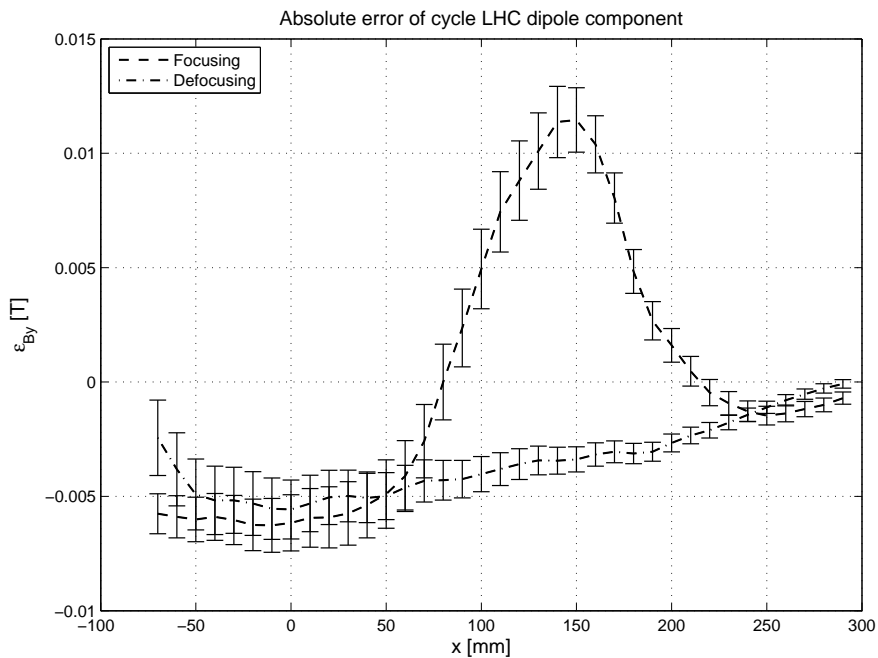
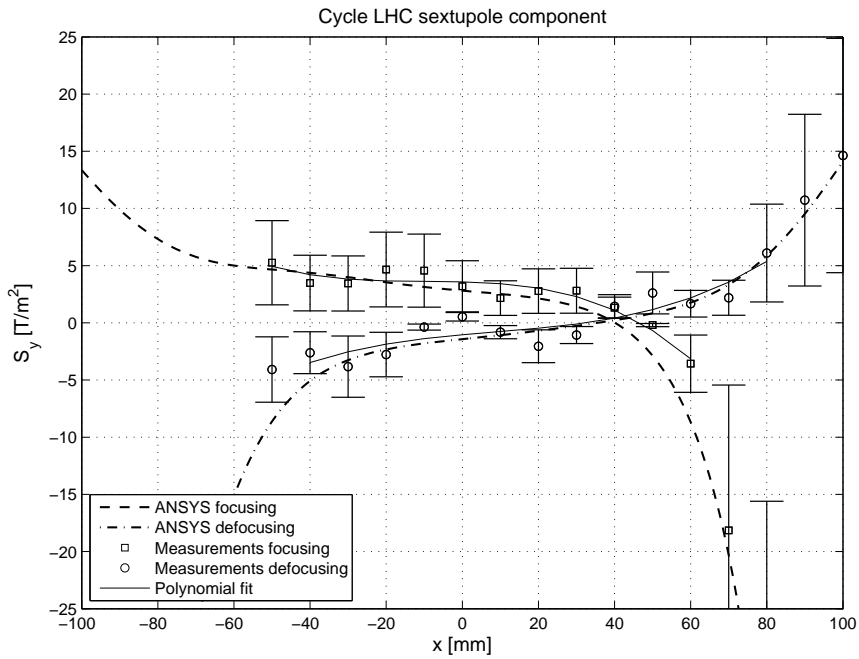Rysunek B.9: Cykl LHC – błąd bezwzględny komponentu dipolowego.
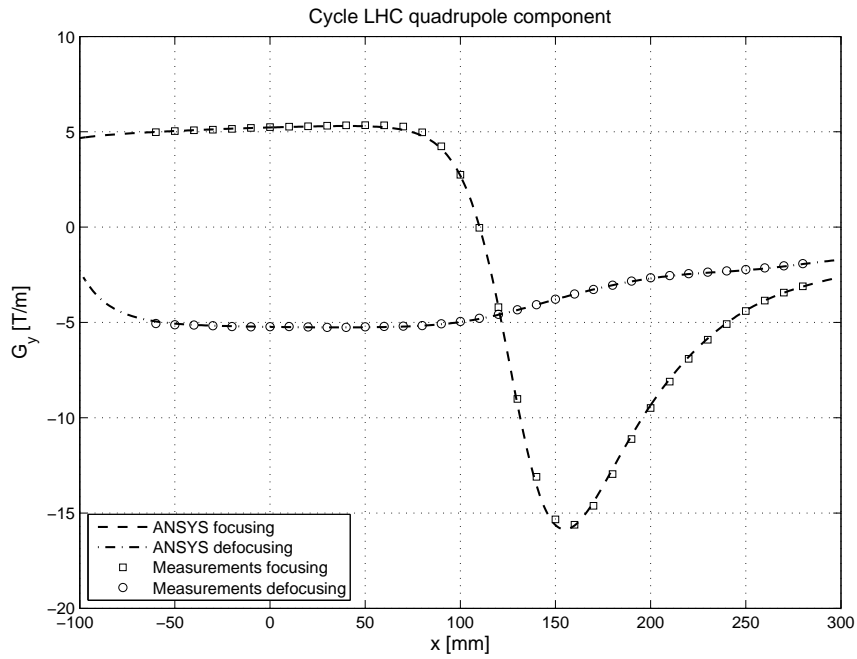
Rysunek B.10: Cykl LHC - komponent kwadrupolowy.

Rysunek B.11: Cykl LHC – błąd bezwzględny komponentu kwadrupolowego.

Rysunek B.12: Cykl LHC - komponent sekstupolowy.

Rysunek B.13: Cykl LHC - komponent sekstupolowy.

B.7   Obliczenia map pola magnetycznego w przestrzeni 3D

Trójwymiarowy model magnesu został stworzony w programie ANSYS Work-bench przy użyciu elementów SOLID117 [1]. Zawiera on 10 bloków, które dla uproszczenia ułożone są w linii prostej i mają izotropowe własności magne-tyczne o czynniku upakowania $\lambda = 0.9496$, oraz obszar przestrzeni która je otacza. Uzwojenie magnesu zostało zamodelowane elementami SOURCE36. Bardzo skomplikowana geometria przewodników wymusiła zastosowanie pew-nych uproszczeń uzwojenia korekcyjnego. Model wykorzystuje symetrię pozio-mą magnesu w celu zmniejszenia ilości elementów skończonych. Mimo to ich liczba sięga niemal 1.5×10^6 dlatego konieczne było stworzenie kilku oddziel-nych modeli o lokalnie zagęszczonej siatce elementów skończonych.
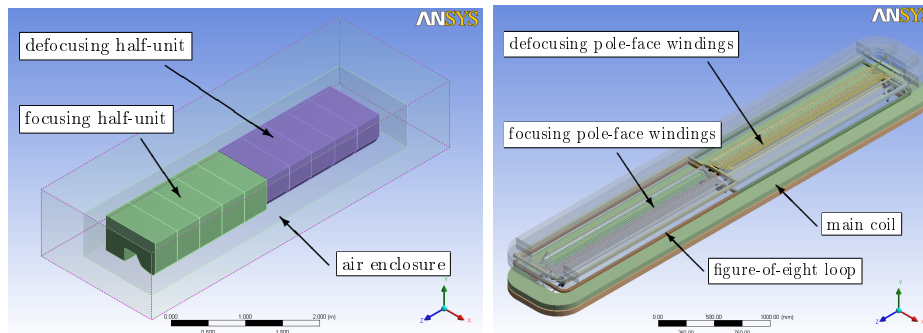

Rysunek B.14: Trójwymiarowy model magnesu oraz uzwojenia.
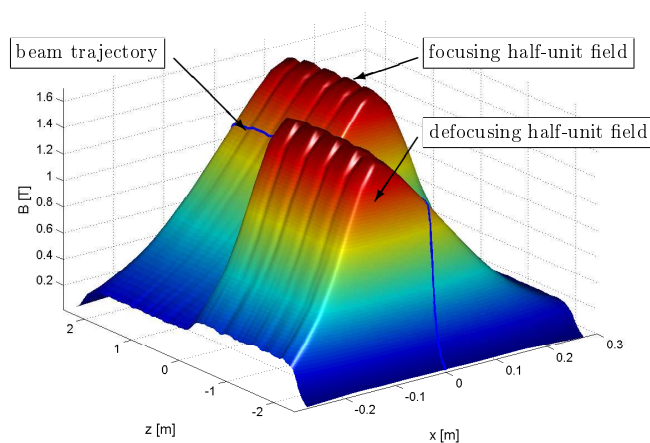
Rysunek B.15: Obliczona mapa pola magnetycznego na płaszczyźnie środkowej magnesu.

Najbardziej interesującym pod względem wyników obszarem jest płaszczyzna symetrii magnesu, a w szczególności trajektoria wiązki cząstek elementarnych która ją przecina. Przy pomocy względnego błędu symulacji wyrażonego przez $\Delta B = |B_c - B_s|$, gdzie B_c jest obliczoną węzłową wartością pola a B_s wartością wygładzonej mapy pola magnetycznego, został oszacowany znormalizowany względny błąd obliczeń $\delta_B = \Delta/B_c^{max}$. Maksymalna wartość błędu na trajektorii wiązki wyniosła 0.26% dla komponentu dipolowego i 1.73% dla kwadrupolowego w obszarze stabilnego pola obu połówek magnesu.
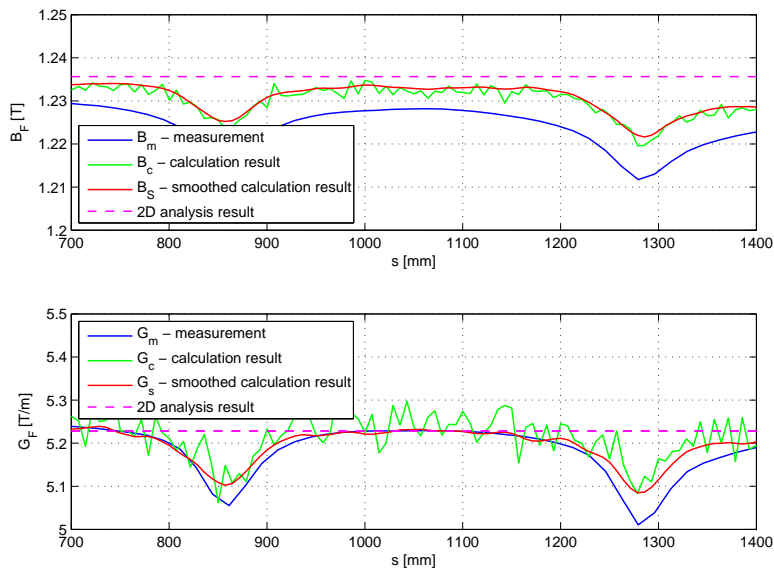
Rysunek B.16: Komponent dipolowy (na górze) i kwadrupolowy (na dole) na trajektorii wiązki w środkowe części pół-jednostki skupiającej.
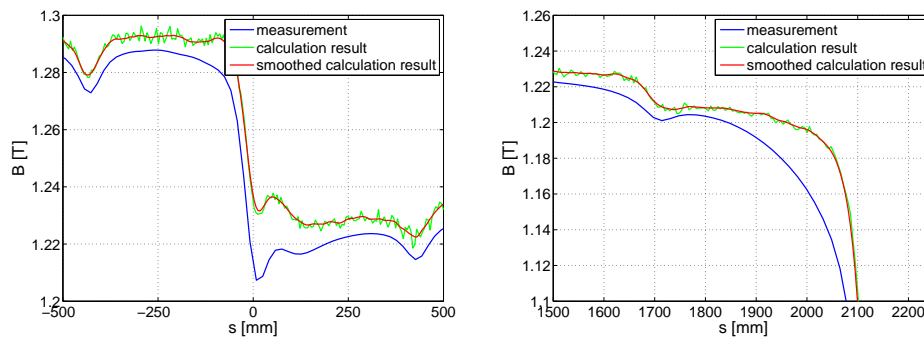
Rysunek B.17: Komponent dipolowy w środkowej części magnesu (po lewej) i na jego końcu (po prawej).

Porównanie wyników obliczeń 3D ze zmierzonym polem magnetycznym dało wyniki bardzo zbliżone do tych z analizy 2D. Różnice dla środkowych bloków obu pół-jednostek magnesu ($s = \pm 1076$ mm) w porównaniu do pomiarów sięgnęły na trajektorii wiązki 0.4% dla komponentu dipolowego i 0.2% dla kwadrupolowego.

W obszarze rozdzielającym połówki magnesu oraz na ich końcach odwzorowanie kształtu pola magnetycznego było bardzo dobre ale rozbieżności były znacznie większe i wyniosły dla komponentu dipolowego 1.5% dla $s = 60$ mm i 2.9% dla $s = 2000$ mm. Należy jednak pamiętać, że właśnie w tych obszarach wpływ uproszczeń modelu jest najbardziej widoczny.

B.8 Zastosowanie rozwiązania MES w programie MAD

Obliczone za pomocą modelu elementów skończonych wartości komponentów pola magnetycznego mogą zostać wykorzystane w programie MAD[3], służącym do projektowania akceleratorów. Stworzony przy jego pomocy model magnesu Synchrotronu Protonowego opisany jest za pomocą multipoli zdefiniowanych następująco:

$$K_n = \frac{1}{B_y\rho}\frac{\partial^n B_y}{\partial x^n} \qquad n = 1, 2, \dots \tag{B.21}$$

gdzie $B_y\rho$ jest sztywnością wiązki, a także poprzez zależne od energii wiązki parametry związane z długością efektywną magnesu, przestrzenią oddzielająca połówki magnesu oraz z geometrią pola magnetycznego na jego krańcach.
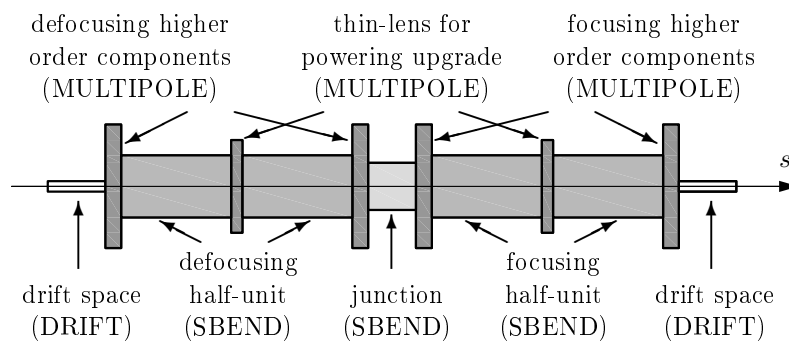
Rysunek B.18: Schemat modelu magnesu w programie MAD.

---

[3]Methodical Accelerator Design

Przy pomocy modelu wykonanego w programie MAD-8 porównano parametry wiązki uzyskane przy wykorzystaniu zarówno obliczonych w analizie 2D jak i zmierzonych wartości pola magnetycznego.

	Pomiary	ANSYS	δ [%]
Q_h	6.2414	6.2490	-0.12
Q_v	6.2917	6.2996	-0.12
ξ_h	-2.7041	-2.6227	3.01
ξ_v	0.6516	0.5746	11.83

Tablica B.5: Parametry wiązki cyklu E policzone w programie MAD-8 przy użyciu pomiarów i obliczeń.

	Pomiary	ANSYS	δ [%]
Q_h	6.2090	6.1689	0.65
Q_v	6.3341	6.3664	-0.51
ξ_h	-1.2625	-1.3522	-7.11
ξ_v	-0.8234	-0.7404	10.07

Tablica B.6: Parametry wiązki cyklu B policzone w programie MAD-8 przy użyciu pomiarów i obliczeń.

	Pomiary	ANSYS	δ [%]
Q_h	6.2343	6.2259	0.13
Q_v	6.2617	6.2710	-0.15
ξ_h	-0.4080	0.0577	114.15
ξ_v	0.3755	-0.0706	118.79

Tablica B.7: Parametry wiązki cyklu C policzone w programie MAD-8 przy użyciu pomiarów i obliczeń.

Natomiast wykorzystując specjalnie zmodyfikowany do tego celu model wykonany w programie MAD-X obliczono parametry wiązki wykorzystując wyniki analizy MES a następnie porównano je z parametrami wiązki zmierzonymi podczas pracy akceleratora.
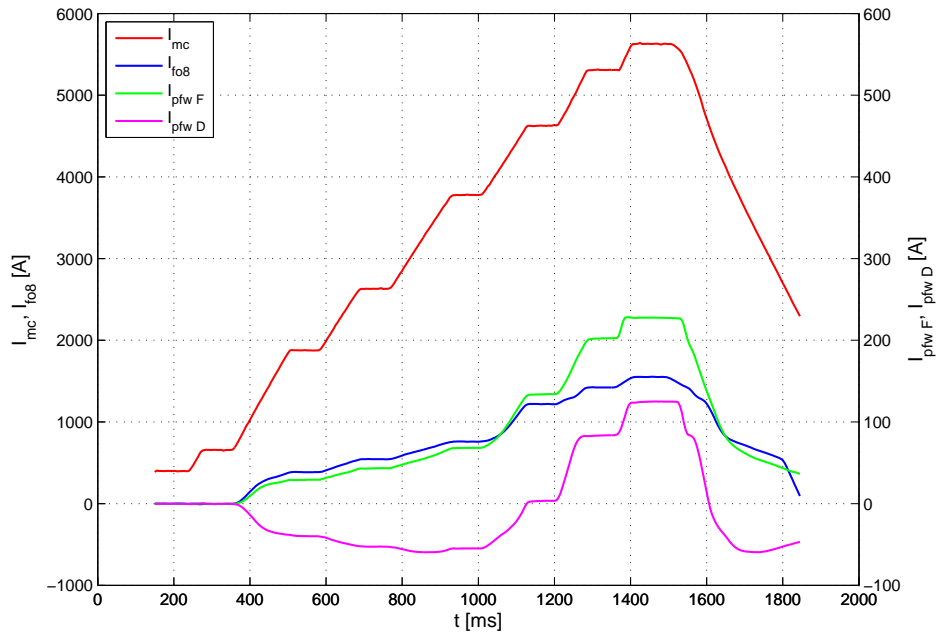
Rysunek B.19: Program natężeń prądu wykorzystany podczas pomiarów.
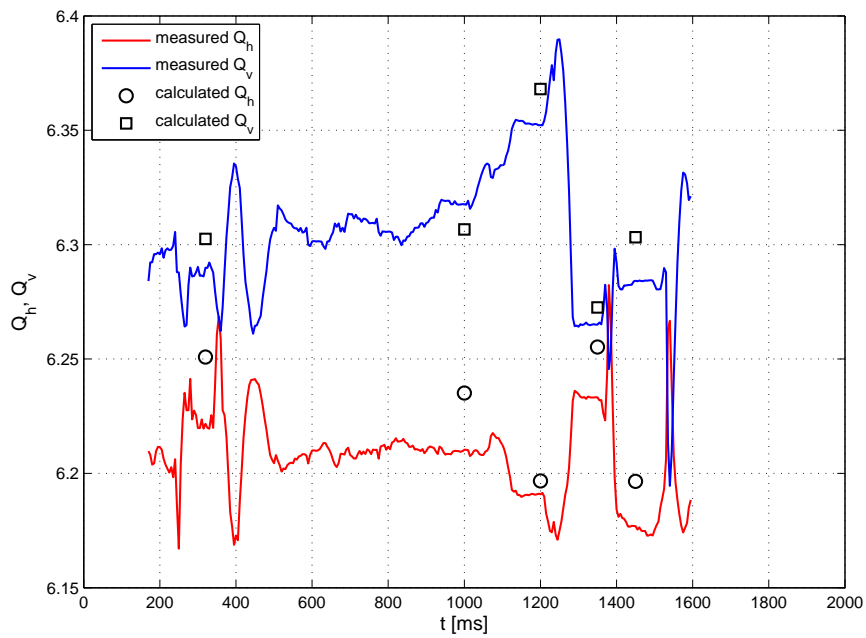
Rysunek B.20: Zmierzone i obliczone wartości parametru tune.

B.9 Wnioski

Zdolność do odtworzenia parametrów optycznych Synchrotronu Protonowego, przy pomocy programów takich jak MAD, jest niezwykle ważna w dostosowaniu tego akceleratora do przyszłych potrzeb. Celem tej pracy było stworzenie modelu numerycznego magnesów tego akceleratora, oraz próba wykorzystania jego wyników zamiast danych pomiarowych w obliczeniach parametrów wiązki.

Dwuwymiarowa analiza pola magnetycznego na trajektorii wiązki wykazała różnicę rzędu 0.5% dla komponentu dipolowego w porównaniu do wyników pomiarów. Komponent kwadrupolowy i sekstupolowy mieściły się w granicach błędu pomiarowego. Wykazana została również duża zależność wyników od parametru upakowania, którego oszacowanie w przypadku 2D nie jest jednoznaczne z powodu złożonej geometrii magnesów.

Głównym czynnikiem ograniczającym obliczenia 3D była liczba elementów skończonych wykorzystanych w modelu, która sięgała nawet 1.5×10^6. Analiza trójwymiarowa dała różnice rzędu 0.4% dla komponentu dipolowego oraz 0.2% dla komponentu kwadrupolowego w stosunku do danych pomiarowych. Ze względu na błędy symulacji, jakość obliczonego komponentu seksupolowego nie była wysoka, jednak jego zachowanie i wartości były bardzo podobne do danych pomiarowych. Wyniki analizy pola magnetycznego pomiędzy połówkami magnesu oraz na jego brzegach dały nieco gorsze rezultaty, czego przyczyną mogły być uproszczenia modelu uzwojenia oraz zastosowanie izotropowych własności żelaza.

W obliczeniach przy pomocy programu MAD część wymaganych parametrów wejściowych, takich jak wartość gradientu pola magnetycznego pomiędzy połówkami magnesu czy korekcja gradientu na końcach magnesu, była dostępna jedynie dla kilku konfiguracji wzbudzenia, natomiast sam model synchrotronu w programie MAD jest pod pewnymi względami uproszczony. Mimo tych ograniczeń obliczona liczba oscylacji betatronowych podczas jednego cyklu (tune) różniła się do $\pm 0.47\%$ w porównaniu ze zmierzonymi wartościami. Dla obliczeń chromatyczności nie udało się uzyskać wiarygodnych rezultatów.

Praca ta dostarczyła cennych informacji na temat ograniczeń istniejącego modelu Synchrotronu Protonowego w programie MAD które powinny być wyeliminowane. Pokazała również, że numeryczny model magnesu może być cennym źródłem informacji na temat pola magnetycznego i parametrów wejściowych modelu MAD, jednak kilka kwestii wymaga dalszej pracy badawczej.